UNIVERSITA’ DEGLI STUDI DI PARMA

DOTTORATO DI RICERCA IN
SCIENZA E TECNOLOGIA DEI MATERIALI

CICLO XXX

Functionalization of carbon fibers with piezoelectric ZnO nanostructures for the realization of a deformation sensor embedded within carbon fiber composite

Coordinatore:
Chiar.mo Prof. Enrico Dalcanale

Tutore:
Chiar.mo Prof. Andrea Zappettini

Dottorando: Maurizio Culiolo

Anni 2014/2017

A tutta
la mia famiglia

INDEX

INTRODUCTION

List of acronyms

- **AAO**: anodic aluminum oxide
- **ABS**: acrylonitrile-butadiene-styrene
- **AC**: alternating current
- **AFM**: atomic force microscope/y
- **ALD**: atomic layer deposition
- **AMSE**: School of Advanced Materials Science & Engineering
- **AOT**: Na(DEHSS)
- **CBD**: chemical bath deposition
- **CF**: carbon fiber
- **CFC**: carbon fiber composite
- **CFT**: carbon fiber tow
- **CM**: capacitance measurement
- **CTAB**: cetyltrimethylammonium bromide
- **CVD**: chemical vapor deposition
- **DC**: direct current
- **DEA**: diethanolamine
- **DEHSS**: bis(2-ethylhexyl) sulfosuccinate
- **DHM**: dynamic hysteresis measurement
- ***e.g.***: *exempli gratia* (for example)
- **EDA**: ethylenediamine
- **ER**: epoxy resin
- **ETD**: Everhart-Thornley Detector
- **FBG**: Fiber Bragg Grating
- **HMTA**: hexamethylenetetramine
- ***i.e.***: *id est* (that is, which means, namely)
- **ILSS**: InterLaminar Shear Strength

- **IMEM-CNR**: Istituto dei Materiali per l'Elettronica ed il Magnetismo - Consiglio Nazionale delle Ricerche
- **LM**: leakage current Measurement
- **LPFM**: lateral PFM
- **LSW**: Lifshitz-Slyozov-Wagner
- **MBE**: molecular beam epitaxy
- **MCF**: macro fiber composite
- **MEMS**: microelectromechanical systems
- **MOCVD**: metalorganic chemical vapor deposition
- **NB**: nota bene (note well)
- **NESEL**: Nano Electronic Science and Engineering Laboratory
- **NR**: nanorod
- **PDMS**: polydimethylsiloxane
- **PED**: pulsed electron deposition
- **PEDOT:PSS**: poly(3,4-ethylenedioxythiophene)-poly(styrenesulfonate)
- **PFM**: piezoresponse force microscope/y
- **PLD**: pulsed laser deposition
- **PUND**: pulsed measurement
- **PVD**: physical vapor deposition
- **PW**: plain weave
- **PZT**: lead zirconate titanate
- **SDS**: sodium dodecyl sulfate
- **SEM**: scanning electron microscope/y
- **SHM**: static hysteresis measurement
- **SILAR**: successive ionic layer adsorption and reaction
- **SKKU**: Sungkyunkwan University
- **SL**: seed layer
- **SNR**: signal-to-noise ratio
- **TEA**: triethanolamine

- **TEM**: transmission electron microscope/y
- **TFA**: Thin-Film Analyzer 2000E
- **TMAH**: tetramethylammonium hydroxide
- **TMEDA**: N,N,N'N'-tetramethylenediamine
- **UV**: ultraviolet
- **VdW**: Van der Waals
- **VdWL**: Van der Waals-London
- **VLS**: vapor-liquid-solid
- **VP**: vapor phase
- **VPE**: vapor phase epitaxy
- **VPFM**: vertical PFM
- **XRD**: X-ray diffraction
- **ZEH**: zinc 2-ethylhexanoate
- **ZfCF**: carbon fiber functionalized with zinc oxide nanostructures
- **ZnO**: zinc oxide

INTRODUCTION

Carbon fiber composites

A composite material is a mix between two or more constituents, artificially combined in order to form a new material possessing better features with respect to the uncombined components.
Carbon fibers (CFs) and the relative composites have represented a fundamental discovery for applications where both low weight and high mechanical features are requested.

Advantages and applications

Composites with CFs embedded within epoxy resin (ER) matrix show the following important characteristics:

- Low density (40% lower than aluminum);
- High mechanical resistance (comparable with high resistance steels);
- High rigidity (comparable with titanium alloys, but with much lower density);
- Good fatigue resistance;
- Good creep resistance;
- Low friction coefficient;
- Good aging resistance;
- High tenacity;
- Corrosion resistance;
- Dimensional stability;
- Excellent vibration damping;
- Low electrical resistance;
- High thermal conductivity (higher than aluminum, lower than copper);
- High electromagnetic interference (screening effect).

These properties mean that carbon fiber composites (CFCs) can be used in many applications, such as the ones listed in tab. 1 [1] [2] [3].

BRANCH	APPLICATIONS
Building	Underground pipelines, supports, containments
Aerospace	Wing parts, tails, fuselages, internal panels, helicopter blades
Automotive	Car body parts, spoilers, truck cabs, instrument panels, motorcycle frames, helmets
Navigation	Hulls, sails, decks, structural parts, masts, cordage
Wind energy	Blades
Biomedical	Prosthesis
Sport	Fishing poles, golf clubs, bicycles, skis, canoes, tennis rackets
Accessories	Jewelries, furniture, art, musical instruments, technology

Tab. 1: Different fields of technology where CFCs are widely used.

Drawbacks

One of the limitations in the use of CFCs is the relatively high cost, especially by comparing with common materials such as aluminum and steel, but predictions show that this difference will decrease in few decades (fig. 1) [4].

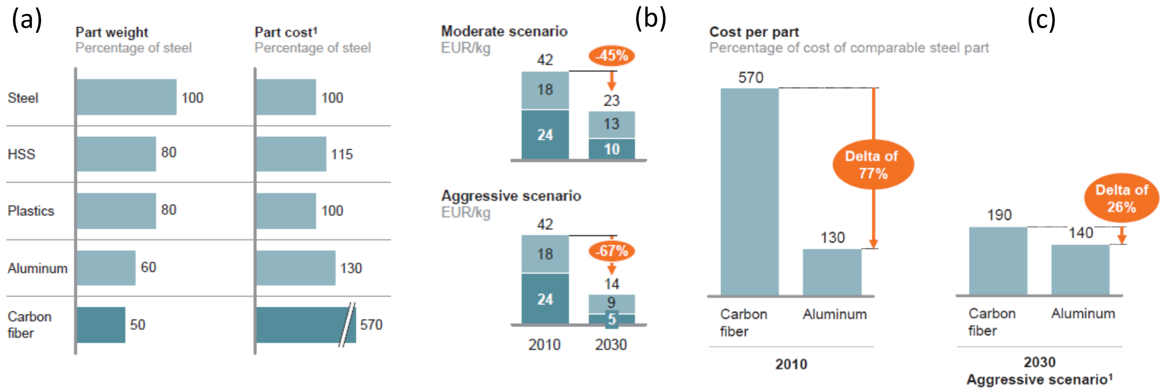

Fig. 1: (a) Cost of different lightweight materials (¹60.000 pieces-per-year assumption). (b) CF cost trend prediction. (c) CF vs. aluminum cost prediction (¹assuming increase in energy cost for both).

However, the most serious issue concerning the use of CFCs is the lack of universal and reliable predictive models for mechanical failures [5]. These materials are, in fact, made of different layers of CF fabric and ER; the assembly process is specific for each object, and the different arrangements lead to variable mechanical behaviors. This aspect is obviously limiting CFCs from spreading in applications where safety is essential such as, for example, aviation. Among all commercial aircrafts, the highest quantity of these materials can be found in Airbus A350 XWB with 53% at most (fig. 2/a).

It is very important, therefore, to analyze vibrations and the other types of deformations in real time.

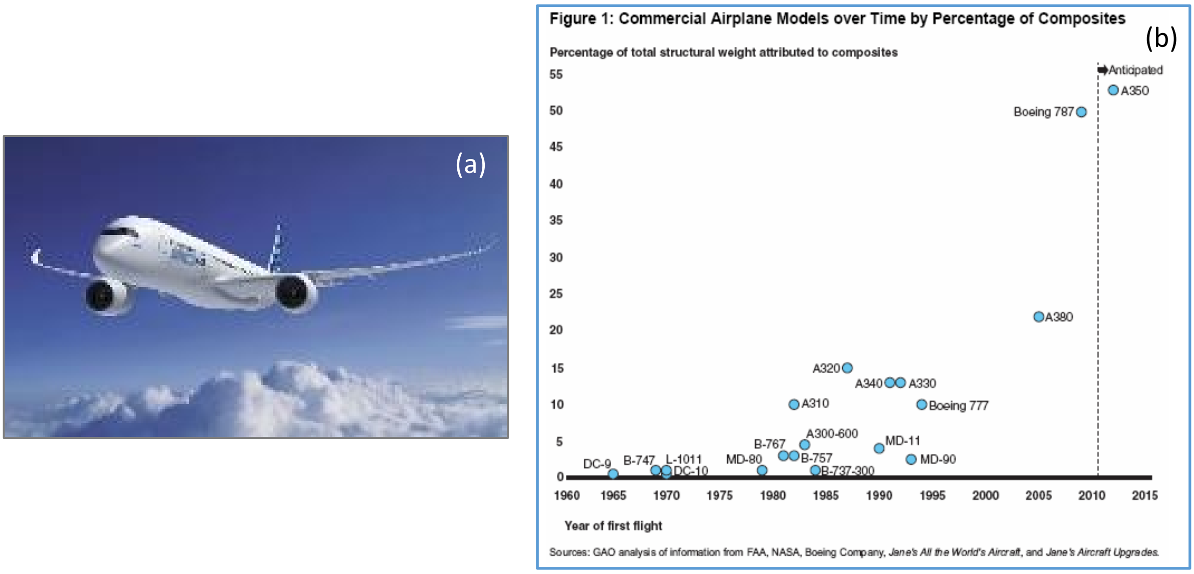

Fig. 2: (a) Airbus A350 XWB. (b) Use of CFCs is the history of commercial aviation.

Deformation sensors for carbon fiber composites

Many nondestructive evaluation techniques are used in order to monitor the mechanical behavior of CFCs, but their employment in operational structures is often inconvenient or impossible due to size and weight [6].

Nowadays deformations in CFCs are meanly measured by means of two compact technologies: piezoelectric fibers and Fiber Bragg Grating (FBG). In both cases the devices are applied either onto the surface of the studied object or, sometimes, embedded into it.

Despite certain advantages, they still present limitations that industry requires to overcome.

- **Piezoelectric fibers**

  The piezoelectric effect is commonly exploited for deformation sensors since it relates deformation with electrical signals.

  One of the most efficient piezoelectric materials is $Pb[Zr_xTi_{1-x}]O_3$ (where $0 \le x \le 1$), called PZT, thanks to its perovskite crystalline structure.

  The first PZT sensors consisted of monolithic ceramic on which electrodes were electrodeposited (fig. 3/a). Successively interdigitated electrodes (fig. 3/b) allowed for better exploitation of the in-plane alignment of electric field, so the piezoelectric effect along the direction perpendicular to the plane. This kind of electrode present an important drawback though: their morphology causes strong polarizations around the electrode branches, generating high stresses within the material that are strong enough to cause breakages.

PZT fibers embedded within resin matrix (fig. 3/c) were introduced hence; this configuration is more adaptable to different geometries and exhibits higher mechanical resistance thanks to the composite structure. It is affected, nevertheless, by the reduction of electric field intensity due to the different dielectric characteristics between PZT and resin; in order to maintain a sufficient electric field, it is necessary to raise it, which can provoke damages as in the case of interdigitated electrodes.

All these problems were solved by means of rectangle-section fiber composites called Macro Fiber Composites (MCFs), also consisting in piezoelectric fibers embedded within ER (fig. 3/d). This arrangement allows higher contact between fibers and electrodes [7] [8] [9].

Piezoelectric effect will be described in detail in chapter 4.

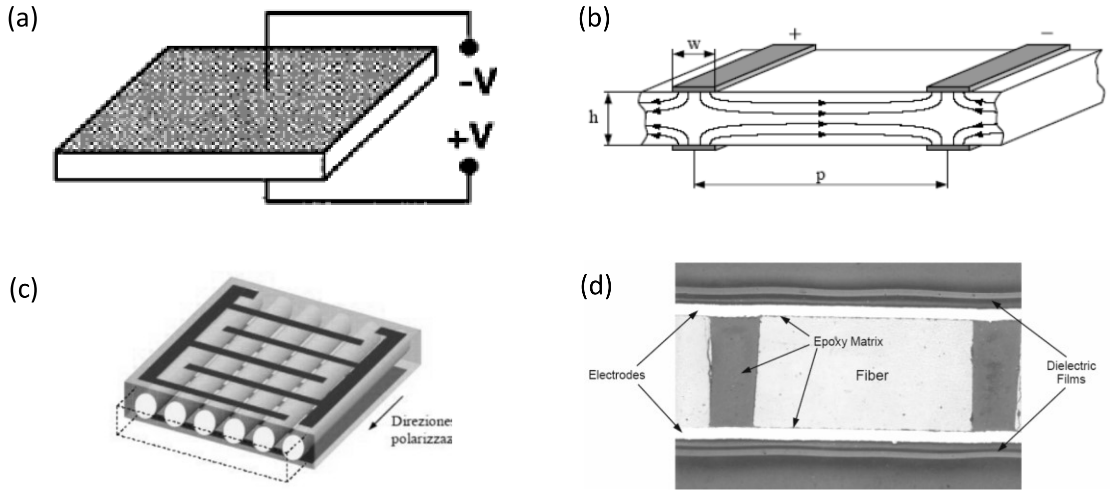

Fig. 3: (a) Representation of monolithic PZT. (b) Representation of interdigitated electrodes on PZT ceramic. (c) Representation of round-section PZT fibers embedded within resin. (d) Macro Fiber Composite (MCF) cross-section view.

- **Fiber Bragg Grating (FBG)**

  The Fiber Bragg Grating technology [10] [11] [12] is based on optical fibers. These are classified as dielectric waveguide, meaning that they can carry high frequency electric fields (approximately around the infrared wavelength) with extremely low leakage. They are used, for this reason, for ultrahigh-speed/long-distance communication and broadband connections, inasmuch they are also manufactured in the form of flexible cables, which are unencumbered by electrical interference and extreme weather conditions.

  The simplest optical fiber structure consists of two concentric and highly transparent active parts: the central cylindrical core and the cladding layer around it. The latter has a slightly lower refraction index with respect to the former. They are surrounded by a buffer layer and a jacket sheath in order to be protected from external physical and chemical solicitations (fig. 4/a).

The structure acts as a tubular mirror, where the total reflection phenomenon occurs: if the entering angle of light is lower than the limit angle (depending on the material), none of the light components will be refracted, so information loss are minimized.

Core and cladding can be made in either silica or polymers (polycarbonates, polycyanides, polysiloxanes). The polymeric ones exhibit better mechanical features (such as higher flexibility and lower fragility) but lower thermal conductivity with respect to glass.

Particularly interesting for deformation sensing is the Fiber Bragg Grating technology (FBG). The sensor is realized by photo-impressing the core material with a periodic grid having a different refraction index with respect to the core material. This is made by means of a mask-assisted UV laser acting perpendicularly to the fiber axis.

The grating is able to reflect only one wavelength (called Bragg wavelength, λ_B) thanks to the constructive/destructive interference effect.

The reflected wavelength is related to the grating characteristics:

$$\lambda_B = 2n_{eff}D$$

Where n_{eff} is the effective refraction index of the grating and D the mesh distance.

A common value of reflected wavelength is around 1550 nm.

As already mentioned, the FBG sensor is usually either applied onto the surface of the analyzed object or embedded within it, so once the object is deformed, the sensor will follow the distortion (fig. 4/b). The reflected wavelength arising from the FBG changes consequently as follows:

$$d\lambda_B = 2(dn_{eff}D + n_{eff}dD)$$

where dn_{eff} is the change of refraction index of the grating and dD the mesh distance variation.

λ_B changes because of both mechanical and thermal stress:

$$\frac{\Delta\lambda}{\lambda_0} = (1-p)\epsilon + n_T\Delta T = (1-p)\epsilon_m + (1-p)\alpha_S\Delta T + n_T\Delta T$$

Here λ_0 is the initial wavelength, p the photoelastic coefficient, α_S the thermal expansion coefficient of the sample, while

$$\epsilon = \epsilon_m + \epsilon_T$$

is the deformation due to the sum of the mechanical component ϵ_m and the thermal one

$$\epsilon_T = \alpha_S \Delta T$$

Moreover, n_T is expressed by the relation

$$n_T = \frac{\left(\frac{\delta n}{n}\right)}{\delta T}$$

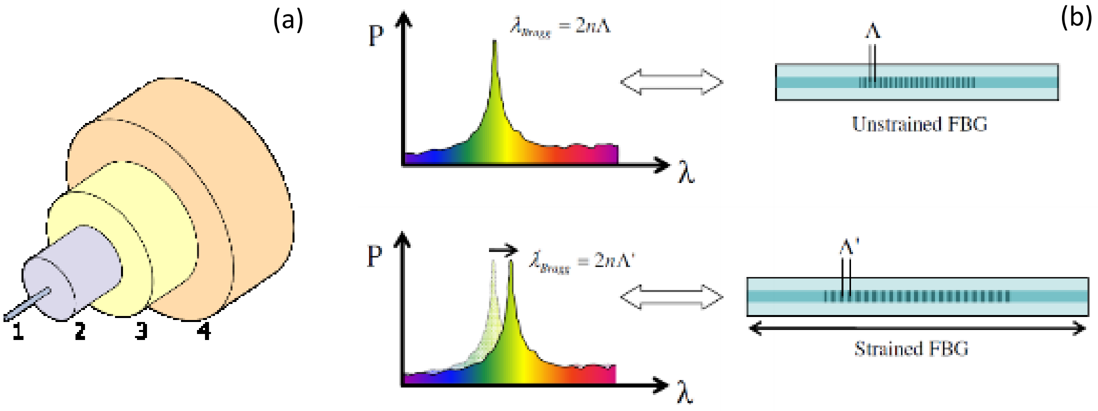

Fig. 4: (a) Optical fiber basic structure. (b) Working principle of a Fiber Bragg Grating.

Drawbacks of current sensing technologies

An important specific issue with FBG is the lack of cohesion between sensor and matrix, which can reduce the sensitivity.

For both PZT and FBG sensors, the main drawbacks are represented by weight addition and the use of extrinsic (and sometimes expensive) materials (fig. 5/c); the most restrictive one, though, is the large size, compared to the typical dimensions of the studied composite structure (*e.g.* carbon fiber diameter and layers thickness), that could worsen the mechanical properties (fig. 5/a-b, fig. 3/d) [12] [13].

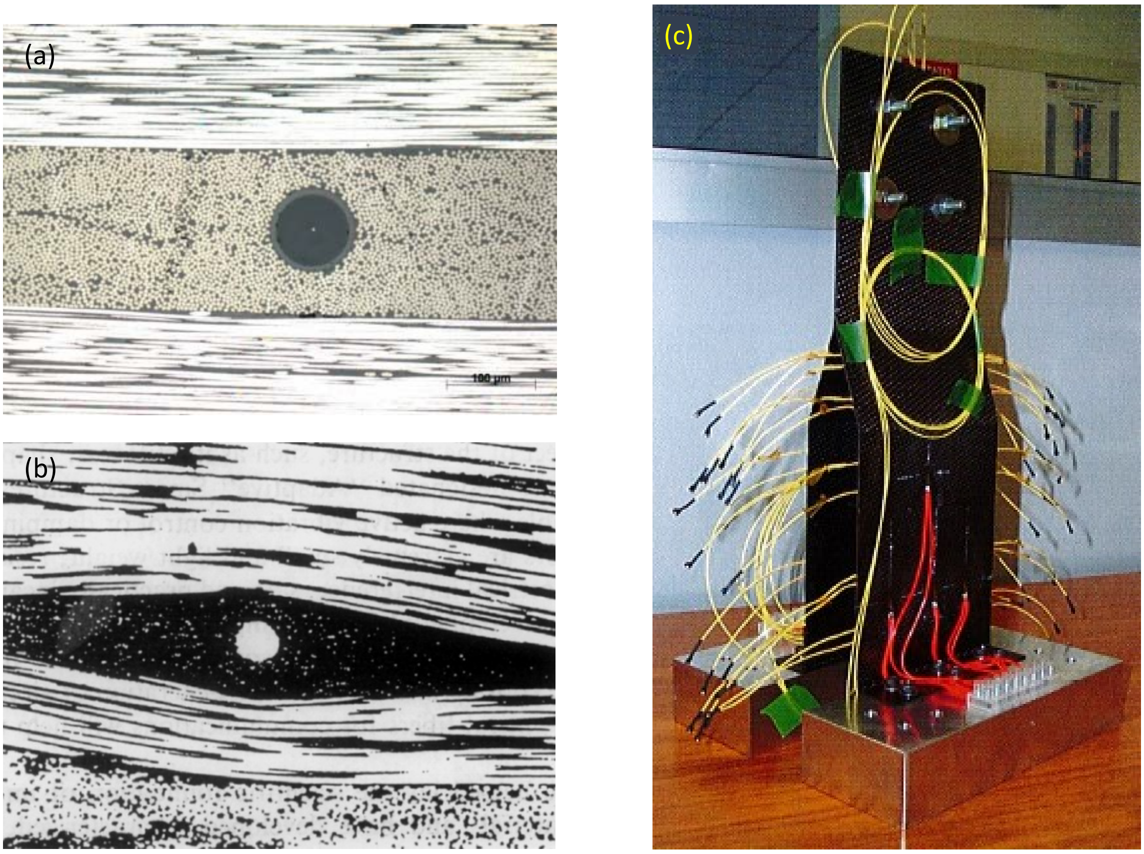

Fig. 5: (a) FBG size compared with carbon fibers and composite layers. (b) "Resin eye" effect due to the size of FBG. (c) Numerous FBG sensors on a CFC object [14].

Proposed solution

On account of these issues, together with the limited knowledge and experience about mechanical failures of CFC materials, it is crucial to realize a low cost deformation sensor that can be totally embedded within the composite matrix without worsening the mechanical properties.

Thanks to the electrical conductivity of carbon fibers, they can be used as electrodes without the need of external materials. It is possible, therefore, to give its composite deformation-sensing properties by functionalizing carbon fibers with a piezoelectric material that can be synthesized at low temperature, in order to avoid oxidative degradation of the carbon fibers. Zinc oxide (ZnO) possess these requested features, hence the work is focused on the functionalization of carbon fibers with ZnO nanostructures with the aim to transform CFC itself into a deformation sensor.

Thesis outline

In this work, ZnO is one of the two main materials, so its electronic properties, crystalline structures, the nanostructures that is possible to grow, synthesis methods and applications are presented as first in **chapter 1**.

A summary expound of the crystal growth mechanisms is included in **chapter 2**, with the classical theory of nucleation and growth, as well as more recent studies about nucleation.

ZnO is grown here in the form of nanorods (NRs) by means of a chemical solution, hence in **chapter 3** the 1D anisotropic growth of wurtzitic ZnO crystals by alkaline aqueous synthesis is illustrated, with particular attention to the role of hexamethylenetetramine (HMTA).

ZnO responds to the needs of low temperature synthesis, low cost and piezoelectricity. Piezoelectric effect is elucidated for both the direct and inverse phenomenon in **chapter 4**, also through the mathematical treatise. Equations for the wurtzitic case are finally displayed.

The theoretical part sees the end in **chapter 5** with an outline of the experimental setup used for the whole work.

The experimental section begins in **chapter 6** with the study of the ZnO NRs synthesis on carbon fibers, divided into the steps of seed layer (SL) deposition and NRs growth. Special interest is posed in the dependence of NRs aspect ratio by precursors concentration.

Two types of device are created: the first is based on crossing two single carbon fibers (**chapter 7**), while the second presents the same crossed structure but entire carbon fiber tows (CFTs) are employed (**chapter 8**). For both, piezoelectric characterization is carried out.

Chapter 9 concerns the final aim of this work, namely embedding the piezoelectric sensor based on ZnO-functionalized carbon fibers (ZfCFs) within a CFC. This turns out to be the most awkward step and criticalities are debated.

THEORY

1 Zinc oxide

ZnO is not a new entry in the science of materials: studies about lattice parameter [15], electronic [16] and optical properties [17] [18] [19] were carried out since the dawn of semiconductor science throughout the twentieth century.
It exhibits intriguing physical and chemical properties, which make it suitable for numerous applications in the different fields of electronics, mechanics and biotechnology.
ZnO is synthesized by means of many physical and chemical methods and plenty of nanostructures can be obtained, enlarging the possibility to find new properties and employments.

1.1 Electronic properties

Wurtzitic ZnO is a II-VI semiconductor material with wide direct bandgap of $3.37\ eV$ at 25 °C and high exciton binding energy of $60\ meV$ [20].
Due to the presence of defects, ZnO exhibits strong luminescence in the green portion of the spectrum with peak at $\sim 495\ nm$ and broad half-width of $0.4\ eV$, as well as the narrow peak at $\sim 370\ nm$ arising from the band-to-band recombination [21].
It presents n-type doping with carrier concentration of $10^{15} \div 10^{20}\ cm^{-3}$ [22] [23] [24] and it is supposed to be mainly caused by hydrogen, whose presence is inevitable in all the synthesis techniques [25]. The role of this element in n-doping is not universally accepted: it can either bond strongly with oxygen of the ZnO crystal [26] or substitute it [27]. The latter option is more likely, due to the higher mobility of interstitial hydrogen (it can easily diffuse out of the sample) [25], or rather, higher stability of substitutional hydrogen. Anyway, it corresponds, in both cases, to shallow donor in the band structure (fig. 6/c), with ionization energy comparable with $k_B T$ [25].

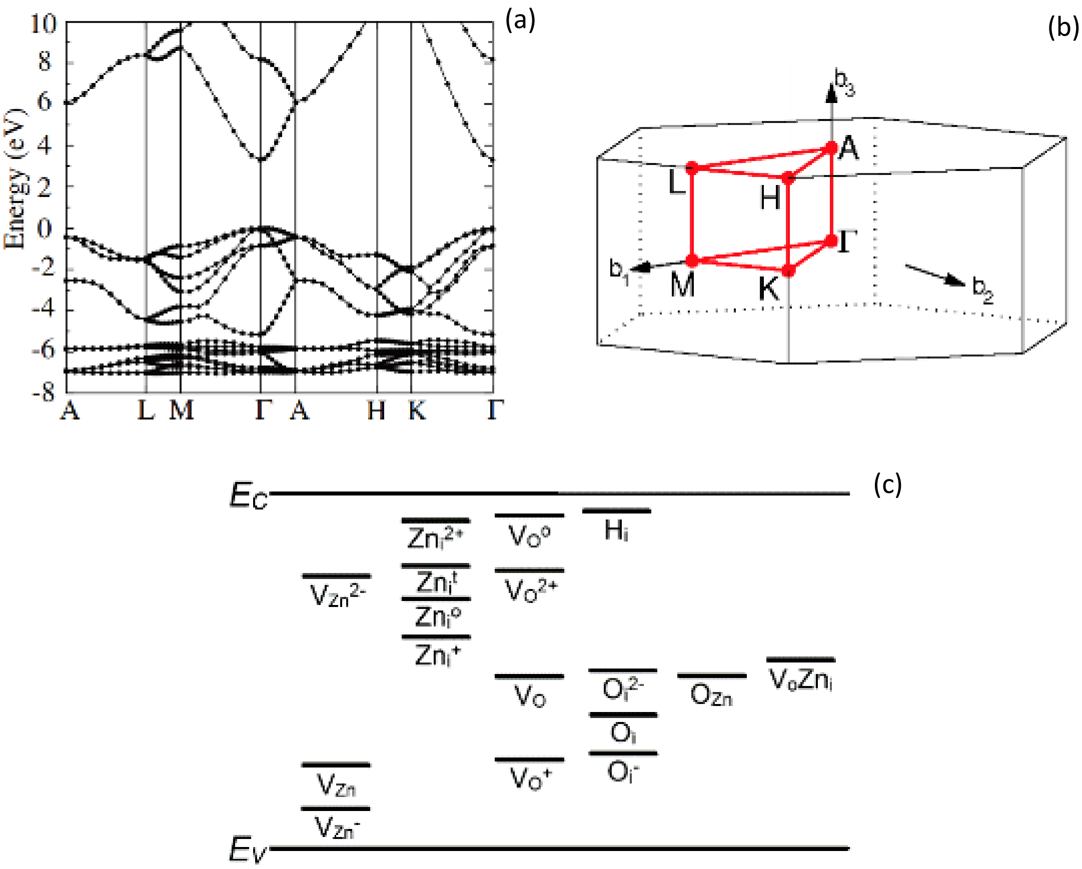

Fig. 6: (a) Band structure of wurtzitic ZnO, calculated by means of HSE hybrid functional [24]. (b) High symmetry points of hexagonal lattice [28]. (c) Energy levels of different defects in ZnO [29].

One of the most relevant challenges in ZnO research is the difficulty to obtain stable p-doping. This is due to the stable n-doping, compensating role of defects [30] [31] [27] [32] and scarce number of shallow acceptors, whose role is controversial anyway [33] [34]. Despite works claiming accomplished p-doping of ZnO, there is no solid evidence of long-term stability [24].

1.2 Crystalline structure

Many II-VI semiconductors crystallize in zinc blend (cubic) and wurtzite (hexagonal) structures, with the ions arranged in tetrahedral coordination; this is, in fact, peculiar of covalent materials with sp^3 hybridization.
ZnO presents an intermediate condition between covalent and ionic and it exhibits three types of structures:

1) Rock salt – cubic
2) Zinc blend – cubic
3) Wurtzite – hexagonal

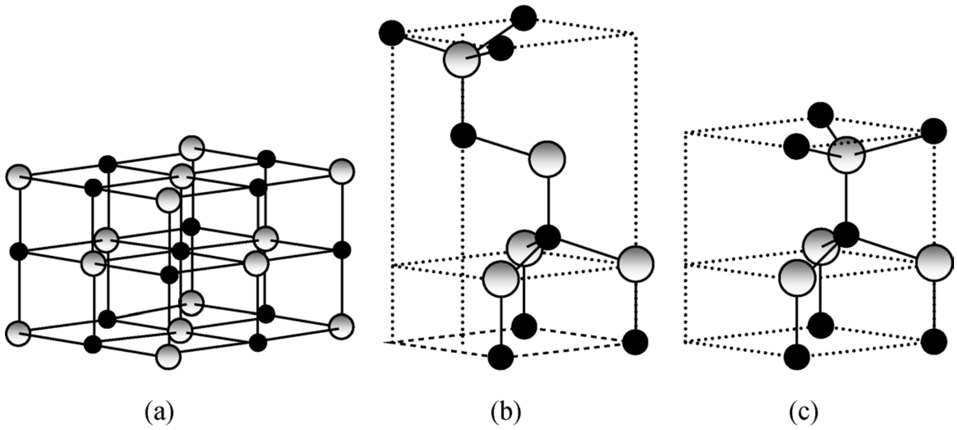

Fig. 7: The different crystalline structures of ZnO. (a) Cubic rock salt, (b) cubic zinc blend, (c) hexagonal wurtzite. Light grey and black spheres represent Zn and O, respectively.

Zinc blend ZnO can be obtained only by growth on substrates with cubic crystalline structure, whereas the $NaCl$ (rock salt) structure of ZnO is achieved at relatively high pressures, as in the case of GaN.
In standard conditions, the thermodynamically stable phase for ZnO is hexagonal wurtzite, the most interesting one for nanostructures.
An ideal wurtzitic structure belongs to the C_{6v}^4 (Schönflies notation) or $P6_3mc$ (Hermann-Mauguin notation) spatial group. It is characterized by the crystallographic parameters a and c, whose ratio is

$$\frac{c}{a} = \sqrt{\frac{8}{3}} \approx 1{,}633$$

and consists in two interpenetrated close-packed hexagonal sublattices, each corresponding to one kind of atom separated from the other one of a distance given by the parameter

$$u = \frac{3}{8} = 0{,}375$$

The crystalline planes are arranged in a $ABAB$ sequence.

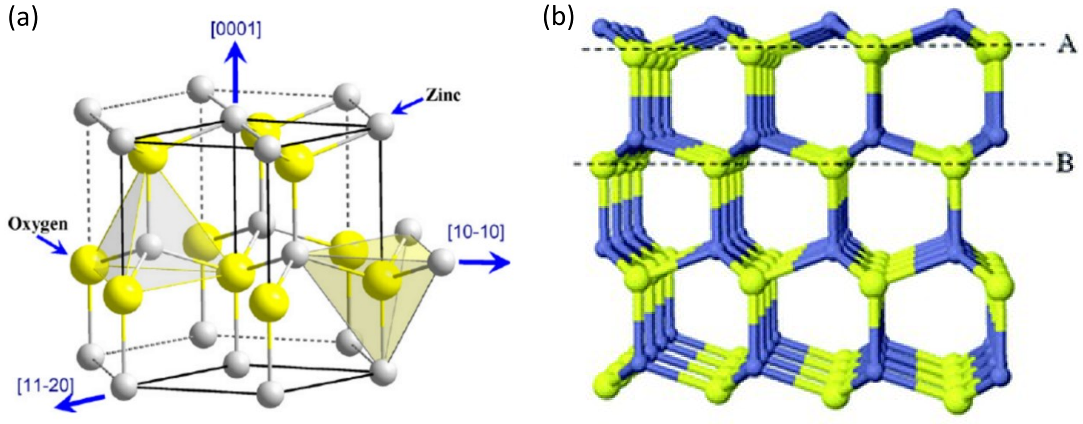

Fig. 8: (a) Hexagonal wurtzite structure. Tetrahedral coordination is highlighted [35]. (b) Plane sequence in the wurtzitic structure [36].

The bond length between nearest neighbor atoms along the [0001] direction is given by the parameter b, the value from which u is defined as the ratio ${}^{b}/_{c}$. The [0001] direction is very important for ZnO nanostructures since the big part of them grow anisotropically along it; it is called c axis.
Each sublattice includes four atoms per unit cell, and each type of atom is tetrahedrally coordinated by atoms of the other kind.
The base vectors of the cell are

$$\vec{a} = a\left(\frac{1}{2}, \frac{\sqrt{3}}{2}, 0\right) \quad ; \quad \vec{b} = b\left(\frac{1}{2}, -\frac{\sqrt{3}}{2}, 0\right) \quad ; \quad \vec{c} = c\left(0, 0, \frac{c}{a}\right)$$

In ZnO the structure slightly deviates from the ideal one due to the ${}^{c}/_{a}$ ratio (or rather u). In particular when ${}^{c}/_{a}$ decreases, u increases, since $u \propto {}^{1}/_{c}$. This sit-

uation corresponds to a compression of the structure along the c axis or, analogously, to an enlargement on the plane defined by the parameter a.
Owing to the partial ionic behavior of ZnO, the long-range electrostatic interactions provoke, indeed, this type of deformation.

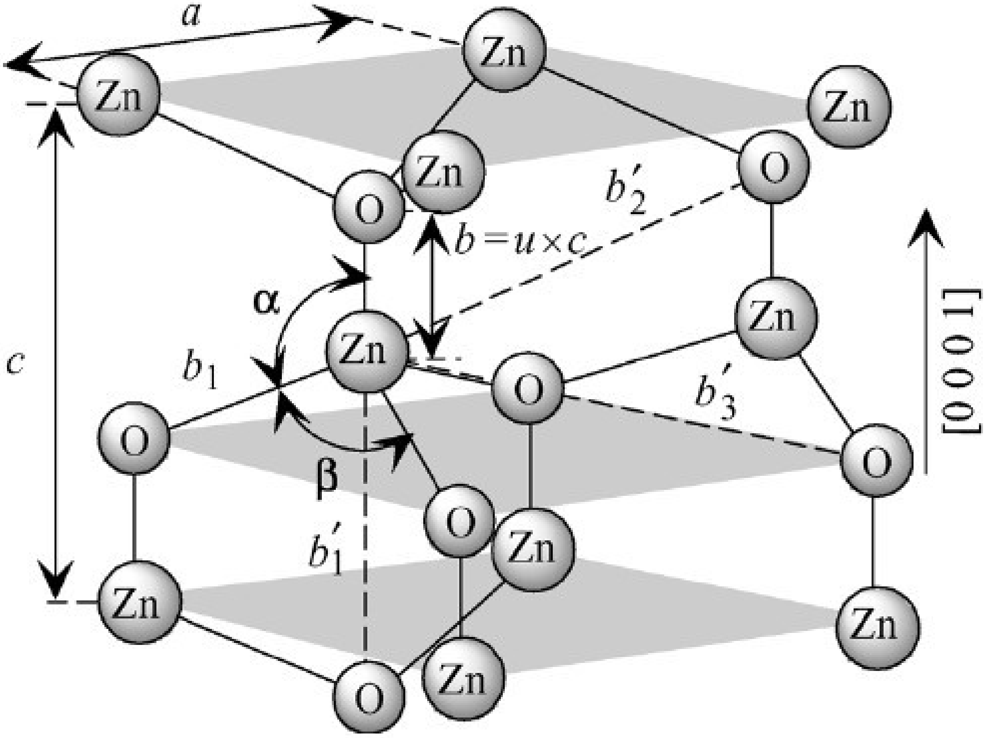

Fig. 9: Geometric parameters of the crystalline structure of ZnO.

The parameters b and b_1, referring to the distances between nearest neighbors that are parallel and non-parallel to the c axis respectively, are calculated as following:

$$b = cu$$

$$b_1 = \sqrt{\frac{1}{3}a^2 + \left(\frac{1}{2} - u\right)^2 c^2}$$

The distances between second nearest neighbors, represented by the parameters b'_1, b'_2 and b'_3, are given by

$$b'_1 = c(1 - u)$$

$$b_2' = \sqrt{a^2 + (uc)^2}$$

$$b_3' = \sqrt{\frac{4}{3}a^2 + \left(\frac{1}{2} - u\right)^2 c^2}$$

The corners α and β are written as

$$\alpha = \frac{\pi}{2} + arccos\left(\frac{1}{\sqrt{1 + 3\left(\frac{c}{a}\right)^2 \left(\frac{1}{2} - u\right)^2}}\right)$$

$$\beta = 2\ arcsin\left(\frac{1}{\sqrt{\frac{4}{3} + 4\left(\frac{c}{a}\right)^2 \left(\frac{1}{2} - u\right)^2}}\right)$$

Concerning the existence of piezoelectric effect in ZnO, the fundamental aspect of this structure is the absence of centrosymmetry [37].
Among the existent 230 spatial groups, only 21 does not possess a center of symmetry [38]. Except for the 432 group (O group in Schönflies notation), which presents high symmetry, for the non-centrosymmetrical groups a structural deformation results in a displacement of the net charge of the two types of ions, originating an electric dipole and, consequently, a potential difference: this phenomenon is called direct piezoelectric effect and will be deeply discussed in chapter 4.

1.3 Nanostructures

ZnO can be synthesized by various techniques. The different growth parameters and conditions lead, probably, to the widest multiplicity of nanostructures we know today [39]. This variety opens a vast range of new opportunities in different fields of technology.
ZnO nanostructures display spatial confinement ranging from 0D to 3D. Nanoparticles [40], nanotubes [41], nanoplatelets [42] and nanoflowers [43], nanodandelions (which can be considered actually as a substrate-driven growth of NRs) [44] are some examples of the diverse possible spatial configurations. Since the first oxide nanobelt was synthesized in 2001 [45], research about one-

dimensional nanostructures in particular has become fruitful because of the applicative possibilities that can originate from structural anisotropy, which is typical of wurtzitic materials [46].

Structures presenting round-like symmetries, such as nanorings, nanohelixes and nanosprings, can be explained by taking into account the polarity of the crystal surfaces. This bent structures result, indeed, from the equilibrium between elasticity and the tentative of reducing the electrostatic energy during growth [47] [48].

Another outcome of polarity and surface energy is visible in nanocombs [49]: the oppositely charged Zn- and O- terminated faces show very different growth rates that can bring to periodic structures.

Hierarchical fir-like nanostructures [50] are grown by the involvement of Sn catalyst particles in vapor-liquid-solid (VLS) method, whereas other catalytic and non-catalytic processes are employed in order to obtain vertically aligned ZnO NRs [46].

Due to the fact that diverse applications take advantage of properties arising from the ZnO crystal structure (*e.g.* piezoelectricity and field emission), vertical parallel arrangement is particularly interesting as regards the possibility to exploit spatial anisotropy [39].

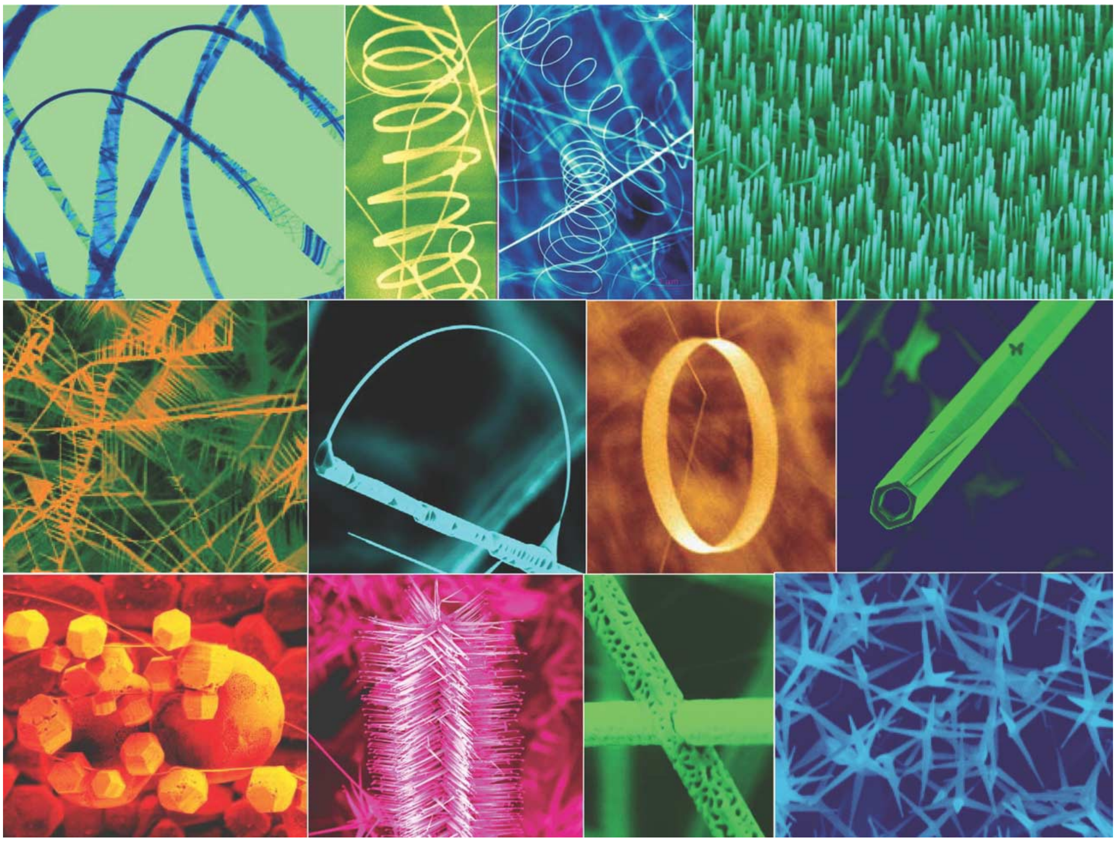

Fig. 10: Variety of ZnO nanostructures obtainable by different synthesis techniques [39].

1.4 Synthesis methods

1.4.1 Bulk

ZnO can be grown by means of gas transport, seeded vapor transport, hydrothermal and pressurized melt techniques [24].

Gas transport consists in the reduction of pure ZnO powder in the presence of hydrogen or graphite at high temperatures (~1300 °C) and the successive oxidation in air or oxygen in a low-temperature zone [51].

In the seeded vapor transport, ZnO powder and ZnO single crystal are placed at the opposite ends of a horizontal tube. The powder is heated up to temperatures higher than 1150 °C and vapor is then transferred by a gas carrier ($e.g.\ H_2$) to the low-temperature zone where ZnO single crystal acts as seed for the bulk growth [52].

In the hydrothermal method ZnO is dissolved in $KOH/LiOH$ solution inside a platinum-lined autoclave at $300 \div 400$ °C. ZnO in then precipitated in a region of lower temperatures. Large crystals of high crystalline quality are obtained [53].

Pressurized melt growth is a modified Bridgman process where radiofrequency is used as heating source in order to produce a molten phase in a cold-wall crucible. ZnO crystal is isolated from the crucible by a cooled ZnO layer [54].

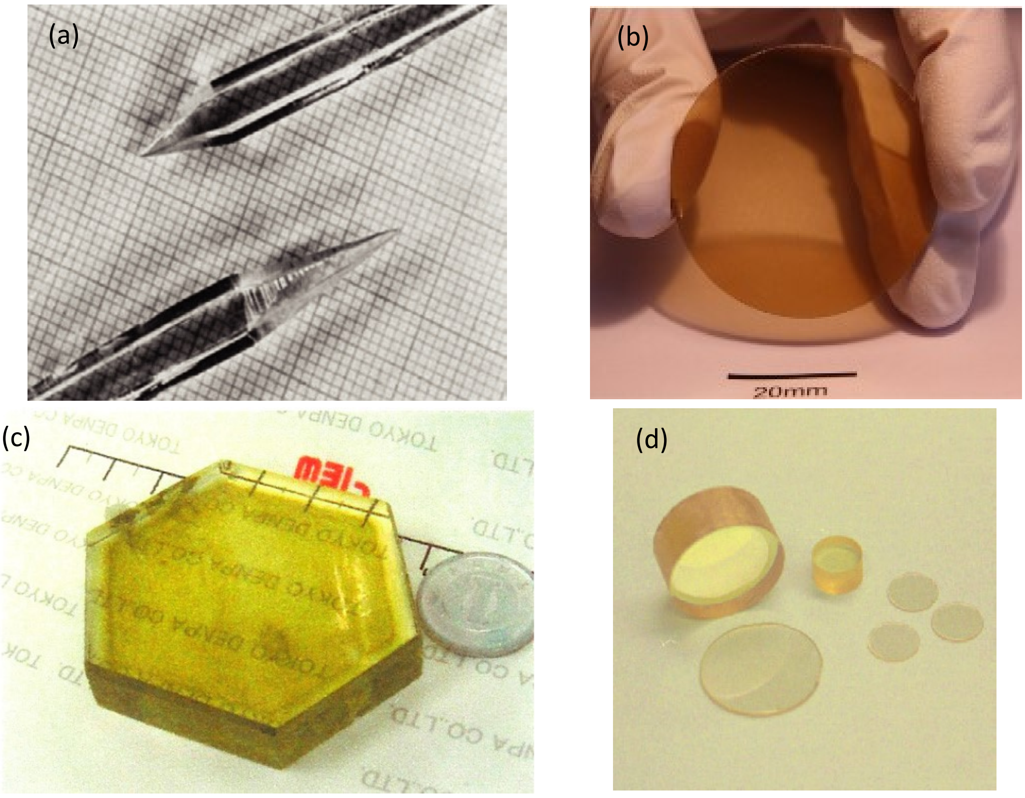

Fig. 11: ZnO bulk crystals grown by (a) gas transport [51], (b) seeded vapor transport [52], (c) hydrothermal method [53] and (d) pressurized melt process [54].

1.4.2 Epitaxial thin films

One of the main advantages of high-quality large single crystals is that thin films with reduced concentration of defects can be grown by epitaxial methods.

For most applications of ZnO, polycrystalline thin films are grown by means of chemical spray pyrolysis, screen painting, electrochemical deposition, sol-gel method and oxidation of Zn films. Nevertheless, for some applications such as optoelectronics, where high-quality crystals are required, these techniques produce ZnO with relatively high concentration of defects. Higher quality can be achieved by pulsed laser deposition (PLD) [55], chemical vapor deposition (CVD) [56], metal-organic CVD (MOCVD) [57], molecular beam epitaxy (MBE) [58] and sputtering (usually magnetron setup) [59]. This last technique is the most scalable one, although it provides lower crystalline quality [24].

In PLD a high-power pulsed laser beam strikes a ZnO target (sintered ceramic disk, single crystal or pure Zn with oxygen atmosphere). A plume of precursors is formed and condensation occurs on the surface of the substrate, which is usually either glass or sapphire. Recent improvements have

been reached by means of $ScAlMgO_4$ substrates in terms of crystalline quality [24].
MOCVD and MBE lead to very high crystalline quality but with the disadvantage of very slow growth rates (only $\sim 200\ ^{nm}/_{h}$ for MBE-grown ZnO) [60] and much more complicated setups. Whereas in the former chemical reactions take place, in the latter physical deposition is responsible for the growth.

1.4.3 Nano/microstructures

Methods for the synthesis of nano- and micro-structured ZnO can be divided into two main areas: metallurgical and chemical processes (fig. 12) [61].

- **Metallurgical processes**

Metallurgical processes are based on Zn ores manufacture and are classified in direct and indirect, depending on whether Zn is provided by ores and metallic form respectively.

- ***Direct (American) process***

In this method, Zn ore is reduced by heating in air in the presence of coal (coke or anthracite) and the obtained Zn vapor is then oxidized. Due to the presence of impurities in Zn ores, the resulting ZnO is a low-purity product. Lead, iron and cadmium oxides are removed through the formation of stable sulfates.
The resulting ZnO particles are mainly needle- and spheroidal-shaped.

- ***Indirect (French) process***

In this case, metallic Zn is melted and the formed vapor is oxidized by oxygen in air. Since the precursor is metallic Zn, this technique provides ZnO with lower concentration of impurities. The product is mainly spheroidal-shaped [62].

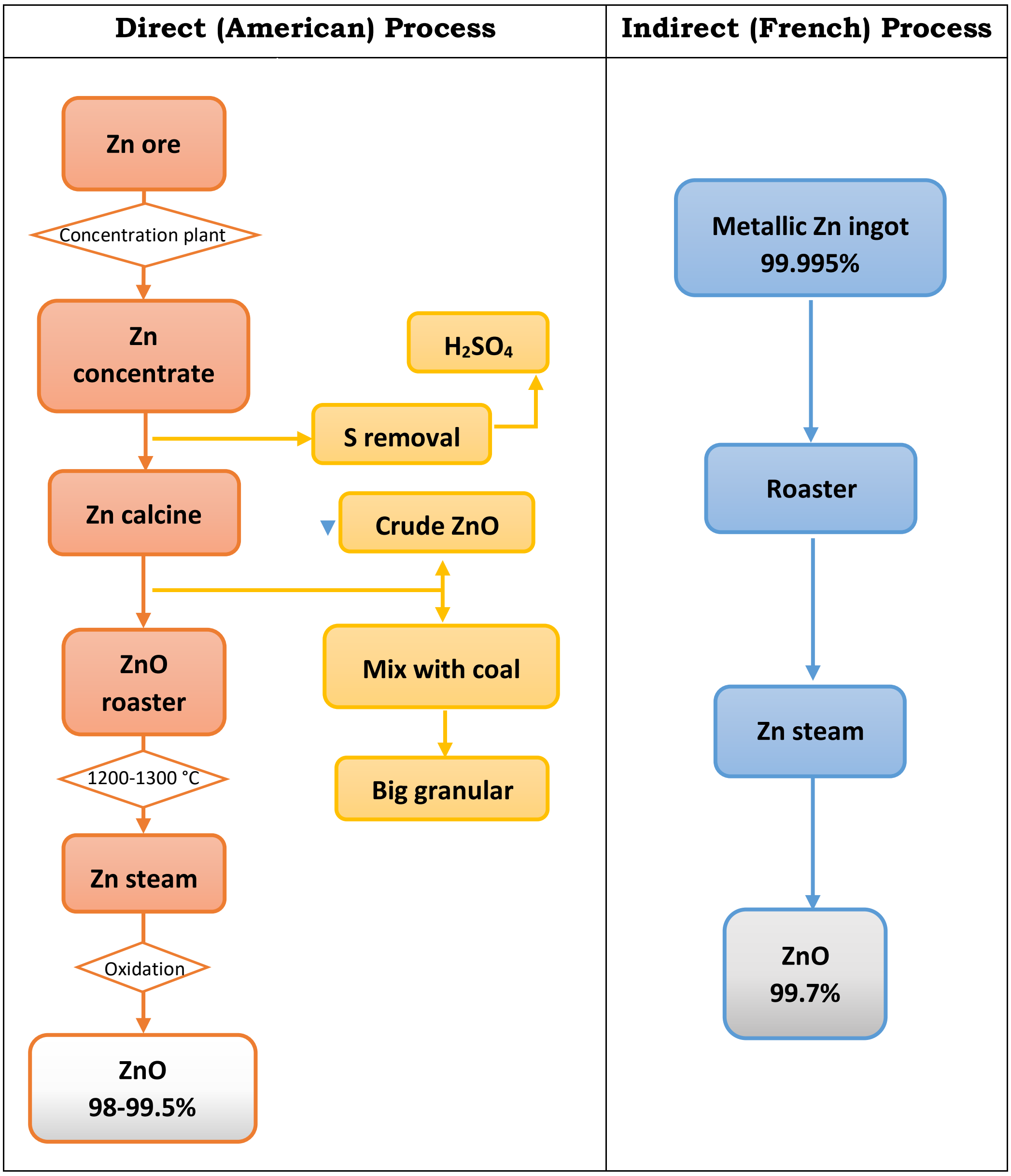

Fig. 12: direct and indirect processes.

- **Chemical processes**

- *Mechanochemical process*

This is a cheap method of obtaining nanoparticles on a large scale. Reaction is initiated by high-energy dry milling through ball-powder impacts at low temperatures. A so called thinner is added in the form of solid (usually $NaCl$) which prevents agglomeration between nanoparticles. A longer milling time means lower size of the particles, but also an increase of contamination. Another drawback is the lack of size control. Advantages lie, instead, in low cost, limited tendency to agglomerate,

small particle size and homogeneity of morphology and crystalline structure.
The starting materials are mainly anhydrous $ZnCl_2$ and Na_2CO_3. The ZnO precursor formed is $ZnCO_3$, which is calcined at 400 ÷ 800 °C.

$$ZnCl_2 + Na_2CO_3 \rightarrow ZnCO_3 + 2NaCl$$

$$ZnCO_3 \overset{T}{\rightarrow} ZnO + CO_2$$

By increasing the milling time it is possible to reduce the particles size, while the opposite occurs by increasing calcination temperature [63].

- ***Controlled precipitation***

This method is widely used thanks to the possibility to obtain repeatable properties. It involves fast reduction of zinc salt solution followed by precipitation of a ZnO precursor, which successively undergoes thermal treatment; milling takes place lastly for impurities removal.
Parameters such as concentration of reagents, substrate nature, pH, temperature and time are vital for the properties of the final product. ZnO nanoparticles can be prepared by potassium hydroxide KOH and $ZnCl_2/Zn(CH_3COO)_2$ (respectively Zn chloride and Zn acetate) aqueous solution and calcination of the zinc hydroxide $Zn(OH)_2$ being formed [64]. Another process makes use of $Zn(CH_3COO)_2$ and ammonium carbonate $(NH_4)_2CO_3$ aqueous solution, with polyethylene glycol (PEG) as surfactant. Thermal treatment is carried out by either calcining at 450 °C for 3 hours or following heterogeneous azeotropic distillation [65].
A low cost single-step process is fulfilled with aqueous Zn nitrate $Zn(NO_3)_2$, sodium hydroxide $NaOH$ and starch, this acting as anti-agglomeration agent thanks to the numerous $O-H$ functional groups [66]. ZnO nanoparticles are synthesized by means of the following reactions as well:

$$5ZnSO_{4(aq)} + 10(NH_4)HCO_{3(aq)} \rightarrow Zn_5(CO_3)_2(OH)_{6(s)} + 5(NH_4)_2SO_{4(aq)} + 8CO_{2(g)} + 2H_2O$$

$$Zn_5(CO_3)_2(OH)_{6(s)} \rightarrow 5ZnO_{(s)} + 2CO_{2(g)} + 3H_2O_{(g)}$$

The nanoparticles display, in this case, very narrow size distribution and crystalline purity [67].

Jia *et al.* [68] report transformation of stable ε-$Zn(OH)_2$ intermediate into ZnO, studied by time-resolved X-ray diffraction (XRD) and scanning electron microscopy (SEM) investigation and explainable by two different mechanisms. One is that, after the formation of $Zn(OH)_2$, this is dissolved by further addition of base (NH_3) to the solution and reprecipitated in the form of ZnO. The other one is the *in situ* transformation involving dehydration and internal atomic rearrangement.
The use of surfactants is very common in the synthesis of nanostructures, since they make possible to control size and prevent agglomeration. Well-dispersed ZnO nanoparticles are obtained by $ZnCl_2$ and NH_4OH solution in the presence of cationic cetyltrimethylammonium bromide (CTAB) [69]. Other ZnO nanostructures with various shapes are prepared by $Zn(NO_3)_2$ and $NaOH$ with cationic surfactants such as sodium dodecyl sulfate (SDS) and triethanolamine (TEA). In this case, they act on both size and shape of the nanostructures [70].

- ***Sol-gel method***

Low cost, simplicity, repeatability, reliability and relatively mild conditions of synthesis are the reasons why sol-gel method is largely employed for the preparation of ZnO nanostructures. Surface modification is often achieved by this method and the optical properties of the obtained nanoparticles is matter of interest.

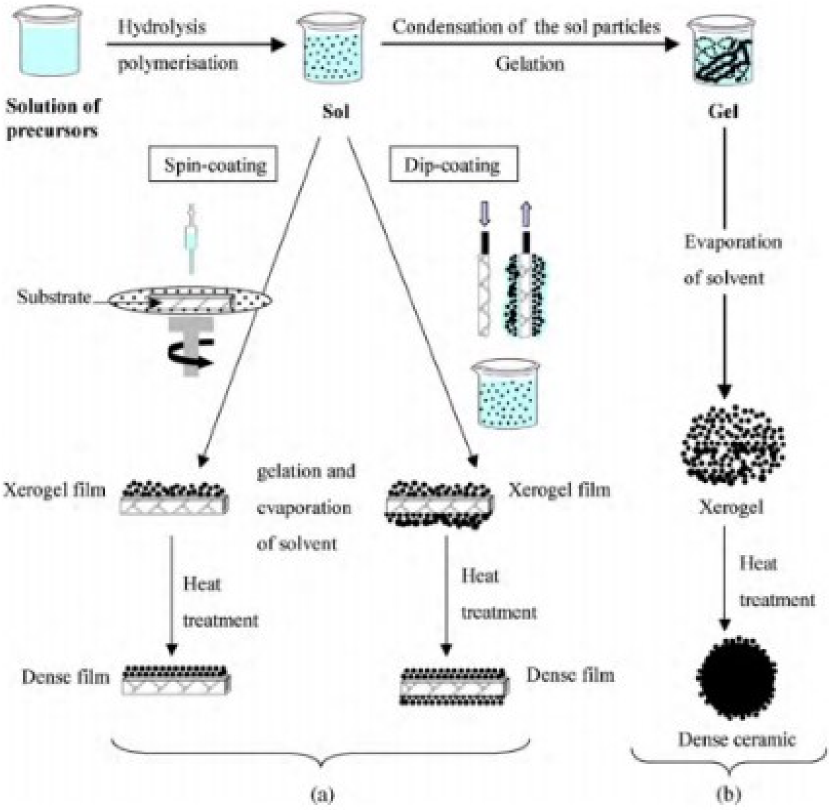

Fig. 13: (a) Films prepared from colloidal sol. (b) powder obtained by colloidal sol transformed into a gel [71].

In sol-gel process, organic compounds with different functional groups are used in order to stabilize the nanoparticles and form the gel. ZnO nanopowder can be obtained by $Zn(CH_3COO)_2$ and oxalic acid in ethanol [72]. Here $Zn(CH_3COO)_2$ is the Zn precursor, while oxalic acid is needed for the stabilization of nanoparticles and the successive formation of gel triggered by ethanol.

Another process, based on the same principles, makes use of zinc 2-ethylhexanoate (ZEH) and tetramethylammonium hydroxide (TMAH) in propan-2-ol [73]. This time a strong organic base (TMAH) is exploited, in order to prevent cation contamination that could bring to change in conductivity.

ZnO nanotubes were fabricated by directly injecting sol-gel, prepared by $Zn(CH_3COO)_2$ and diethanolamine (DEA) in ethanol, into the mesh of anodic aluminum oxide (AAO) [74]. This template-assisted growth of 1D nanostructures demonstrates that sol-gel method is not restricted to the synthesis of nanoparticles.

- ***Hydro/solvothermal methods and microwave/ultrasound use***

Hydrothermal method does not require organic solvents and high energy treatments after the synthesis. The process is carried out in autoclave, where solutions can be heated up to 100 ÷ 300 °C in controlled pressure, in order to speed up kinetics without reaching boiling points.
An example of hydrothermal reaction is the following:

$$ZnCl_2 + 2NaOH \rightarrow Zn(OH)_2 \downarrow + 2Na^+ + 2Cl^-$$

$$Zn(OH)_2 \rightarrow ZnO + H_2O$$

White $Zn(OH)_2$ precipitates and then pH is corrected to 5-8 through HCl, since as pH increases, size of the particles increases as well. By increasing temperature, the aspect ratio of the nanostructures decreases [75]. Another common way to obtain ZnO nanostructures is the following [76]:

$$Zn(CH_3COO)_2 + 2NaOH \xrightarrow{HMTA} Zn(OH)_2 + 2CH_3COONa$$

$$Zn(OH)_2 \overset{T}{\rightarrow} ZnO + H_2O$$

The first reaction is carried out in the presence of HMTA, whose role is essential to control the shape of crystals and will be discussed further in chapter 3.
By combining different Zn precursors ($Zn(CH_3COO)_2$, $Zn(NO_3)_2$) and bases ($LiOH$, KOH, NH_4OH) at different synthesis durations, dehydration of precursors and successive recrystallization lead to hexagonal structures with tunable diameter [77].
Ultrasounds and microwaves can be exploited in order to significantly raise reaction speed. The main advantages of these two technologies are the possibility to avoid surfactants and to scale up the processes with low costs. Microwaves, in particular, selectively act on solvent, reducing energy losses caused by heating the entire vessel and so improving yield of hydrothermal processes. The effect of both ultrasounds and microwaves have been studied by Hu *et al.* [78] for the synthesis of ZnO nanostructures. A solution of $Zn(NO_3)_2 \cdot 6H_2O$ and HMTA have been used, resulting in unlinked and linked NRs and multipods.
A systematic study on the effect of the use of microwaves, electrical current, Joule heating, high-voltage pulses and heating of the whole autoclave has been made by Strachowski, Łojkowski, Choduba *et al.* [79] [80]. They found that the phase composition closest to pure ZnO was obtained

by means of microwaves.
Microwaves are also used in a solvothermal process involving Zn acetylacetonate and Zn oximate in alkoxyethanols (methoxy-, ethoxy- and butoxyethanol). In this case, morphology and aggregation strongly depend on precursors, while size on both precursor and alcohol [81]. Solvothermal reactions, contrary to hydrothermal, do not make use of water as solvent.
Peculiar pierced microspheres, desert rose-like structures and hierarchical structures are synthesized through the following reactions:

$$2(1-x)OH^- + 2xF^- + Zn^{2+} \rightarrow Zn(OH)_{2-2x}F_{2x}$$

$$Zn(OH)_{2-2x}F_{2x} \rightarrow Zn_{1-x-y}F_{2x}(OH)_{2y} + (1-x-y)H_2O$$

Here solvo- and ionothermal processes take place, in the presence of ionic imidazolium tetrafluoroborate [82].
Another solvothermal synthesis consists in a reaction between Zn powder, trimethylamine N-oxide and 4-picoline N-oxide in organic solvents such as toluene, ethylenediamine (EDA) and N,N,N'N'-tetramethylenediamine (TMEDA) [83]. The different oxidizing agents and solvents lead to different morphologies and sizes; moreover, it is noticed that even traces of water can catalyze the reaction between Zn powder and 4-picoline N-oxide.

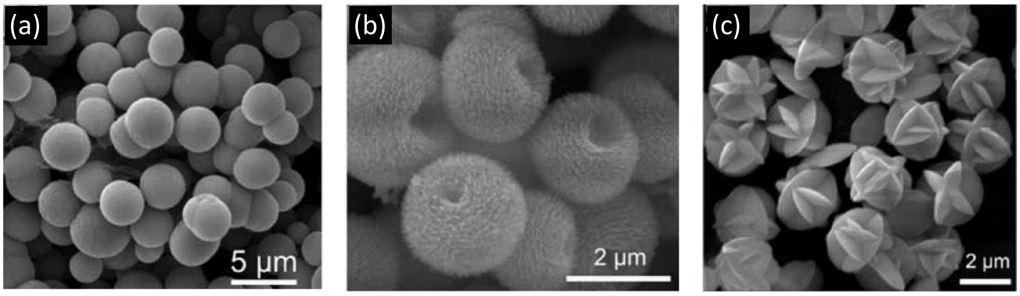

Fig. 14: (a) Spherical, (b) hierarchical hollow structures and (c) desert rose-like structures obtained by solvo/ionothermal process [82].

- ***Emulsions and microemulsions***

An emulsion is classified as a system where a discontinuous, immiscible liquid phase is dispersed into a continuous liquid one. This definition can be further sorted depending on whether matrix and dispersed phase are respectively hydrophilic and hydrophobic or *vice versa* [84] [61].
ZnO can be obtained by precipitation from interphase reaction between

Zn oleate dissolved in decane and $NaOH$ dissolved in either water or ethanol:

$$Zn(C_{17}H_{33}COO)_{2(decane)} + 2NaOH_{(water/ethanol)} \rightarrow ZnO + H_2O + 2C_{17}H_{33}COONa$$

Temperature, substrates and ratio of the two phases affects size of the nanostructures being formed, with shapes ranging from nanoneedles to spherical and hexagonal particles [85].

In another process [86] the aqueous phase is $Zn(CH_3COO)_2$ in de-ionized water, while the organic one is heptane, with specific surfactant Span-80 for water-in-oil emulsion stabilization. NH_4OH is added in order to obtain Zn^{2+}; lastly, calcination is carried out at $700 \div 1000$ °C.

ZnO can be prepared also by precipitation from emulsion with $Zn(CH_3COO)_2$ and either KOH or $NaOH$ as precipitating agent, whereas the organic phase is given by cyclohexane with a non-ionic surfactant. By changing some parameters such as precipitating agent and quantity of the organic phase, different shapes are obtained, ranging from ellipsoids to flakes and rods [87].

An interesting category of emulsions is represented by microemulsions, which are stable, transparent, isotropic liquids consisting of an aqueous layer, oil layer and surfactant. The drop size ranges between 1.5 to 150 nm. Unlike normal emulsions, microemulsions can form spontaneously in appropriate conditions [61].

One example of microemulsion used for the synthesis of nanometric ZnO consists in heptane and hexanol as oil phase and Triton X-100 as non-ionic surfactant; $Zn(NO_3)_2$ solution and $NaOH$ solution, both aqueous and with PEG 400 additive, are added to the oil phase and mixed together for the reaction that generates ZnO [84]. Different PEG 400 concentrations lead to various nanostructures, as shown in fig. 15.

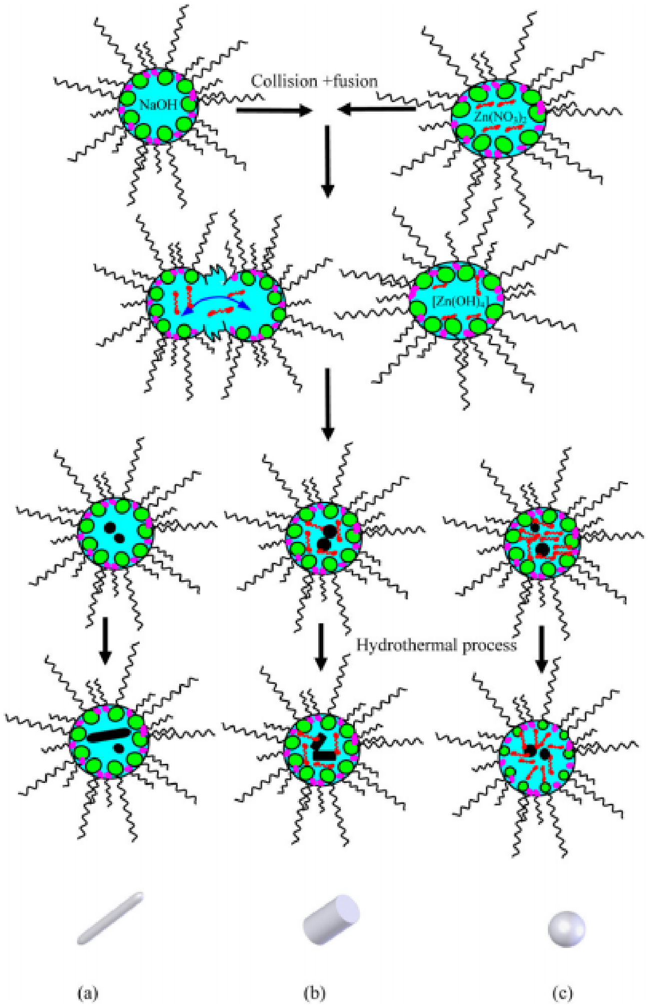

Fig. 15: Formation mechanism of ZnO nanostructures by PEG-assisted microemulsion process. Green and pink shapes represent surfactants, while red chains depict PEG molecules. (a) Nanowires are formed in the absence of PEG. (b) NRs and (c) nanoparticles grow in the presence of 12.5-25% and 50% of PEG respectively [84].

Another process involves a microemulsion of isooctane, ethanol and a Zn precursor. Zn precursor is prepared by mixing $Zn(NO_3)_2$ in dry ethanol with sodium bis(2-ethylhexyl) sulfosuccinate Na(DEHSS) (Aerosol OT, or AOT) in dry ether. Dry solvents are needed in order to avoid collateral dissolution of $NaNO_3$ with consequent contamination. Na is substituted by Zn for the formation of $Zn(DEHSS)_2$. The final precursor, namely Zn oxalate, is formed by addition of oxalic acid and calcined at 300 °C for 3 hours to get ZnO nanoparticles [88].

AOT is present also in a modified microemulsion method used for the synthesis of size-monodisperse ZnO nanoparticles. The reverse microemulsion system consists in AOT as surfactant, glycerol as polar phase and n-heptane as non-polar phase. $Zn(CH_3COO)_2$ and $NaOH$ solutions are added but ZnO is not formed directly since glycerol, acting as complexing agent for Zn, prevents precipitation and subsequent agglomeration. Final

ZnO results from thermal decomposition of the Zn-glycerol complex during calcination. The shape of nanostructures depends from the amount of surfactant; in fact, by increasing the quantity of AOT, more hydrophilic heads interact, forming a micellar layer with larger area and promoting growth of NRs at the expense of nanoparticles [89].

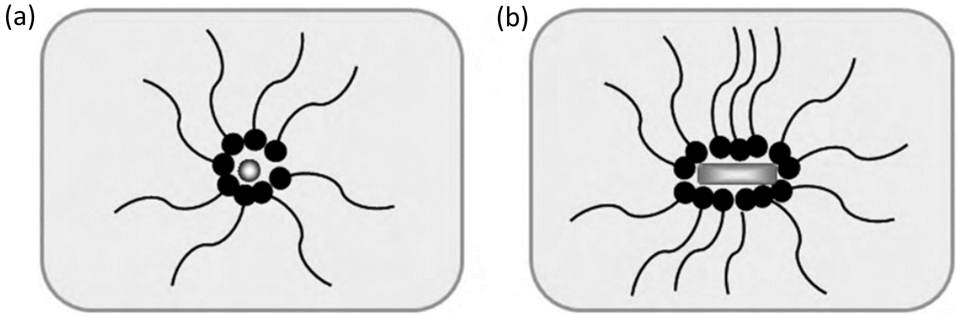

Fig. 16: Growth of ZnO NRs (b) is favorite at higher surfactant concentrations with respect to nanoparticles (a).

In a study by Xu *et al.* [90] ZnO nanostructures resulting from emulsion, microemulsion and chemical precipitation are compared. In all of these methods, the starting Zn precursor is $Zn(NO_3)_2$ and final calcination is carried out at 600 ℃ for 2 hours.
The emulsion consisted in $Zn(NO_3)_2$ and surfactants with different ionic behaviors (cationic, anionic or non-ionic). Nanoparticles in the presence of cationic surfactant showed larger size, followed by the non-ionic and anionic case.
Microemulsion was prepared from $Zn(NO_3)_2$, cyclohexane, acrylonitrile-butadiene-styrene copolymer (ABS, anionic surfactant), ortho-butanol and hydrogen peroxide H_2O_2. Chemical precipitation was carried out by simply dissolving $Zn(NO_3)_2$ with no surfactant.
The smallest nanoparticles were obtained by microemulsion ($< 20\,nm$), while the largest by chemical precipitation ($50\,nm$).

- ***Spray methods***

Ultrafine particles can be prepared by means of two different aerosol processes: one involves gas-to-particle conversion (build-up method) and the other liquid-to-solid particle conversion (break-down method). In the first case particles are generated by cooling a supersaturated vapor by physical vapor deposition (PVD) and chemical vapor deposition (CVD).
In PVD, vapor is formed by evaporation of a solid or liquid. In the cooling stage, nucleation and condensation of the saturated vapor take place and solid particles are formed. In CVD, instead, vapor arises from the solution

precursors and it thermally decomposes or reacts with another precursor vapor; finally, the solid particles are formed by nucleation, condensation and coagulation. The primary advantages of the gas-to-particle conversion method are the small particle size (a few nanometers to micrometer), narrow size distribution and high purity of the particles. However, hard agglomerates can form and it is difficult to synthesize multicomponent materials (*e.g.* phosphors and superconductors), because the differences in chemical reaction rate, vapor pressure, nucleation and growth rate may lead to non-uniform composition.

Spray pyrolysis is, by contrast, a break-down method. A starting solution is prepared by dissolving the metal salt of the product in a solvent. Droplets are atomized from the starting solution by different methods, such as air-assist (pneumatic), two-fluids nozzle, ultrasonic, vibrating orifice or spinning disk; they are sent then to the furnace.

Spray drying is similar to spray pyrolysis except for the fact that precursors are colloidal particles or sols. Spherical and submicron particles can be synthesized by using this technique.

Electrospray pyrolysis overcomes the limited size control of the aforementioned spray methods. A high voltage (several kilovolts with respect to a counter electrode) is applied to the end of a capillary tube. A conical meniscus of precursor solution is formed and the continuous breakup of the solution jet generates droplets [91].

Flame spray pyrolysis is one of the established commercial low cost processes to produce ceramic nanoparticles. In 2002 ZnO, in particular, was the third largest flame-aerosol made material after carbon black and pigmentary TiO_2.

In this technique, a precursor solution is dosed into the nozzle of a flame atomizer, supplied with oxidizer and combustible gas (usually oxygen and methane). Oxidation of the Zn precursor provides ZnO nanoparticles [92].

Different ZnO nanostructures are synthesized through all these spray methods by varying precursors, substrate temperature, spray rate and other growth conditions. Nanoparticles and NRs are obtained, for example, with $Zn(CH_3COO)_2 \cdot 2H_2O$ [93] and $ZnCl_2$ [94], respectively.

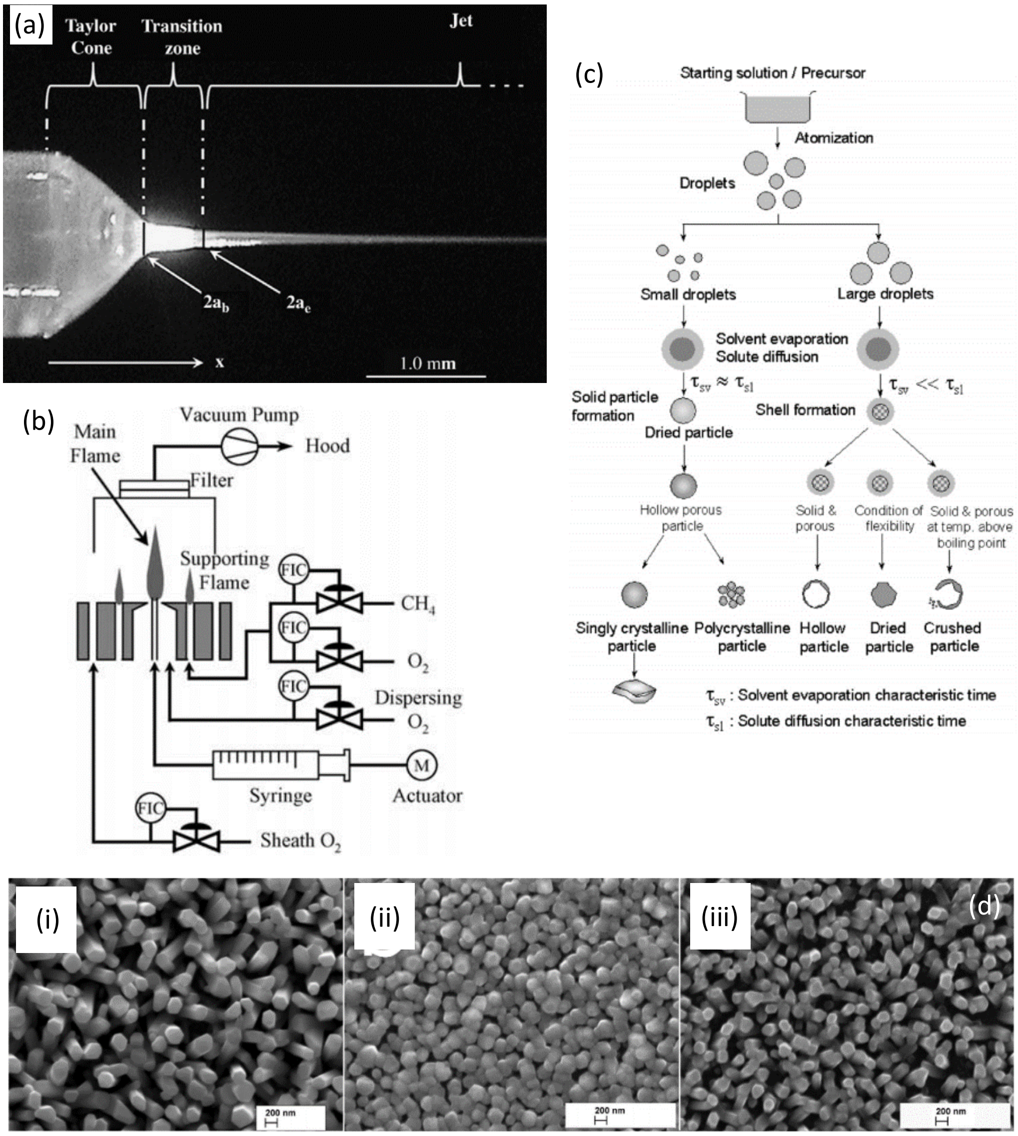

Fig. 17: (a) Micrography of liquid jet produced by electrospray pyrolysis [95]. (b) Diagram of a flame pyrolysis system [92]. (c) Different products depending on the initial droplet size [91]. (d) ZnO NRs grown onto indium tin oxide (ITO)/soda lime glass (SGL) substrate by spray pyrolysis at growth temperature of 550 °C *(i) or* 480 °C *(ii, iii) using aqueous (i, ii) or alcoholic solutions (iii) [94].*

- ***Gas phase***

In the vapor-solid processes, precursors are vaporized under certain temperature, pressure, atmosphere and flow rate conditions and successively recondensed, for the formation of ZnO. The process is usually carried out in a horizontal tube furnace; carrier gas is injected into the tube in order to allow the transport of precursors from the source to the final substrate, which is kept at a temperature lower than the condensation temperature of the product [46]. Carrier gas can be either inert (*e.g.* argon, Ar) or participate to the reaction. If ZnO powder is the precursor, Ar is used, otherwise in the case of metallic Zn as precursor, oxygen is needed for oxidation.

Highly oriented *ZnO* NRs and other types of *ZnO* nanostructures, such as nanotetrapods, can be grown by means of this technique [96] [97].

- ***Vapor-liquid-solid (VLS)***

VLS crystal growth mechanism was first proposed by Wagner and Ellis in 1964 [98]. It is a catalyzed process in which the 1D growth of the desired material is assisted by a specific liquid alloy droplet. The catalyst can be rationally chosen from the phase diagram by identifying metals in which the nanowire elements are soluble in the liquid phase, but do not form solid compounds more stable than the desired nanowire phase.
The liquid droplet represent a preferential site for absorption of gas reactant and, when supersaturated, it acts as nucleation site for crystallization. Nanowire growth begins as soon as the liquid becomes supersaturated in reactant materials, and it continues as long as the catalyst alloy remains in a liquid state and reactant is available. During growth, the catalyst droplet directs the nanowire growth direction and defines its diameter. Ultimately, the growth terminates when the temperature is below the eutectic temperature of the catalyst alloy (or the reactant is no longer available, as stated above).
For the growth of 1D *ZnO* nanowires via a VLS process, the commonly used catalysts are gold [99] and tin [50] and the growth proceeds along [0001].

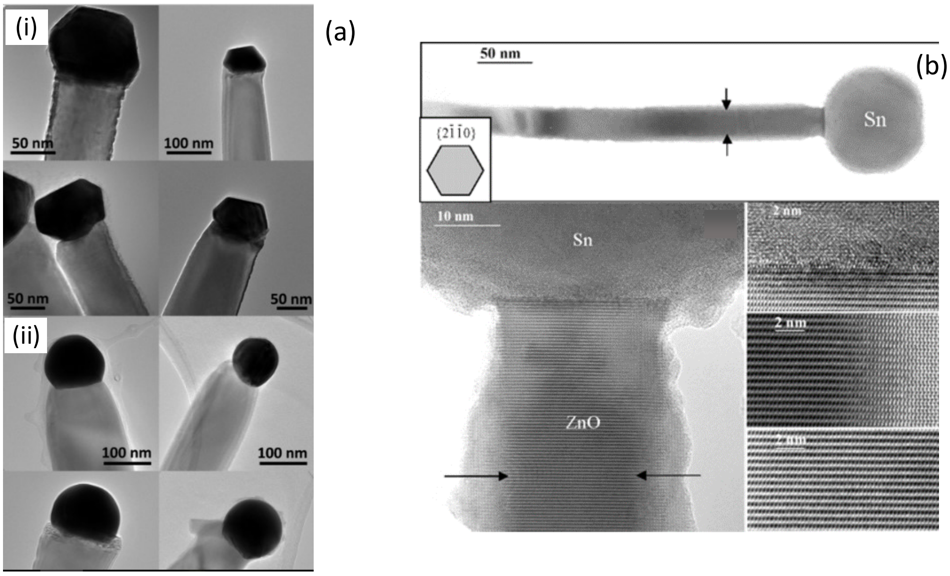

Fig. 18: ZnO nanowires grown by VLS method. (a) Faceted (i) and non-faceted (ii) gold catalyst droplets [100]. (b) Tin [101] catalyst droplets.

METHOD	PRECURSORS	SYNTHESIS CONDITIONS	PROPERTIES AND APPLICATIONS
Mechano-chemical process	$ZnCl_2$, Na_2CO_3, NaCl	calcination: 2 h, 600 °C	hexagonal structure; particles diameter: 21–25 nm
		400–800 °C	hexagonal structure; particles diameter: 18–35 nm
		400 °C	regular shape of particles; diameter ~27 nm, BET: 47 m^2/g
		0.5 h	particles diameter: 27–56 nm
		300–450 °C	particles diameter: ~51 nm, BET: 23 m^2/g
Precipitation process	$Zn(CH_3COO)_2$, and KOH as a water solutions	temperature of process: 20–80 °C; drying: 120 °C	particles diameter: 160–500 nm, BET: 4–16 m^2/g
	$Zn(CH_3COO)_2$, $(NH_4)_2CO_3$, PEG10000 as a water solutions	drying: 12 h, 100 °C; calcination: 3 h, 450 °C	zincite structure; spherical particles ($D \sim$ 30 nm); application: as a photocatlyst in photocatalytic degradation
	$Zn(NO_3)_2$	calcination: 2 h, 600 °C; aging: 240 h, 320 °C	wurtize structure; particles diameter: 50 nm; application: as a gas sensor
	$Zn(NO_3)_2$, NaOH	synthesis: 2 h; drying: 2 h, 100 °C	particles of spherical size of around 40 nm
	$ZnSO_4$, NH_4HCO_3, ethanol	drying: overnight, 100 °C; calcination: 300–500 °C	wurtize structure; crystallite size 9–20 nm; particle size D: ~12 nm, BET: 30–74 m^2/g
	$Zn(CH_3COO)_2$, NH_3 aq.	precipitation temperature: 85 °C; drying: 10 h, 60 °C	hexagonal structure, shape of rods, flower-like particles: L: 150 nm, D: 200 nm
	$ZnSO_4$, NH_4OH, NH_4HCO_3	reaction: 30 min, 60 °C; drying: 12 h, 100 °C; calcination: 2 h, 400 °C	hexagonal structure, flake-like morphology (D: 0.1–1 µm, L: 60 nm)
	microsized ZnO powder, NH_4HCO_3	reaction: ~2 h, 25 °C; drying: 80 °C; calcination:1 h, 350 °C	hexagonal wurtize structure; flower-like and rod-like shape (D: 15–25 nm, BET: 50–70 m^2/g)
	$Zn(CH_3COO)_2$, NaOH	reaction: 30 min, 75 °C; drying: overnight, room temperature	hexagonal structure; flower shape (L: >800 nm); application: antimicrobial activity
Precipitation in the presence of surfactants	$ZnCl_2$, NH_4OH, CTAB	aging: 96 h, ambient temperature, calcination: 2 h, 500 °C	zincite structure; particles diameter: 54–60 nm, $BET = \sim 17$ m^2/g
	$Zn(NO_3)_2$, NaOH, SDS, TEA (triethanolamine)	precipitation: 50–55 min, 101 °C	wurtize structure, shape of rod-like (L: 3.6 µm, D: 400–500 nm) shape of nut-like and rice-like, size: 1.2–1.5 µm
Sol-gel	$Zn(CH_3COO)_2$, oxalic acid, ethanol and methanol	reaction temperature: 60 °C; drying: 24 h, 80 °C; calcination: 500 °C	zincite structure; aggregate particles: ~100 nm; shape of rod; particles L: ~500 nm, D: ~100 nm; BET: 53 m^2/g; application: decontamination of sarin (neuro-toxic agent)
	$Zn(CH_3COO)_2$, oxalic acid ($C_2H_2O_4$), ethanol	reaction: 50 °C, 60 min; dried of gel: 80 °C, 20 h; calcined: under flowing air for 4 h at 650 °C	hexagonal wurtize structure; uniform, spherically shaped of particles
	zinc 2-ethylhexanoate, TMAH ($(CH_3)_4NOH$), ethanol and 2-propanol	reaction: room temperature; drying: 60 °C	cylinder-shaped crystallites, D: 25–30 nm; L: 35–45 nm
	$Zn(CH_3COO)_2$, diethanolamine, ethanol	reaction: room temperature; annealed of sol: 2 h, 500 °C	hexagonal wurtize structure; particles: nanotubes of 70 nm

Solvothermal, hydrothermal and microwave techniques	$ZnCl_2$, NaOH	reaction: 5–10 h, 100–220 °C in teflon-lined autoclave	particles morphology: bullet-like (100–200 nm), rod-like (100–200 nm), sheet (50–200 nm), polyhedron (200–400 nm), crushed stone-like (50–200 nm)
	$Zn(CH_3COO)_2$, NaOH, HMTA (hexamethylenetetraamine)	reaction: 5–10 h, 100–200 °C; HMTA concentration: 0–200 ppm	spherical shape; particles diameter: 55–110 nm
	$Zn(CH_3COO)_2$, $Zn(NO_3)_2$, LiOH, KOH, NH_4OH	reaction: 10–48 h, 120–250 °C	hexagonal (wurtize) structure, size of microcrystallites: 100 nm–20 µm
	$Zn(CH_3COO)_2$, NH_3, zinc 2-ethylhexanoate, TMAH, ethanol, 2-propanol	time of autoclaving: 15 min, 2–72 h; final pH: 7–10	particles with irregular ends and holes; aggregates consist particles of 20–60 nm, *BET*: 0.49–6.02 m^2/g
	trimethylamine N-oxide, 4-picoline N-oxide, HCl, toluene, ethylenediamine (EDA), N,N,N',N'-tetramethylethylenediamine (TMEDA)	reaction: 24–100 h, 180 °C	wurtize structure; particles morphology: NRs (40–185 nm), nanoparticles (24–60 nm)
	$Zn(CH_3COO)_2$, $Zn(NO_3)_2$, ethanol, imidazolium tetrafluoroborate ionic liquid	reaction: 150–180 °C; drying: 80 °C in vacuum oven; calcinations: 500 °C	hexagonal (wurtize) structure, hollow microspheres (2–5 µm) consisted nano-sized particles and contained channels (10 nm); hollow microspheres consisted of NRs (~20 nm); flower-like microspheres (2.5 µm)
	zinc acetylacetonate, methoxy-ethoxy- and n-butoxyethanol, zinc oximate	precursor concentration: 2.5–10 wt%; microwave heating: 800 W, 4 min; drying: 75 °C in air	zincite structure; average crystallite size: 9–31 nm; particles diameter: 40–200 nm; *BET*: 10–70 m^2/g
	$Zn(NO_3)_2$, deionized water, HMT (hexamethylenetetramine)	microwave heating: 2 min, 90 °C; drying: 2 h, 60 °C	hexagonal wurtize structure, nanorod and nanowire shape (*L*: ~0.7 µm, *D*: ~280 nm); application: electronic and optoelectronic devices
Emulsion	$Zn(NO_3)_2$, surfactant (ABS, Tween-80 and 40, $C_{21}H_{38}BrN$)	reaction: 25 °C, pH~8; drying: 24 h, 80 °C; calcination: 2 h, 600 °C	grain size: cationic surfactants (40–50 nm), nonionic surfactants (20–50 nm), anonic surfactants (~20 nm)
	$Zn(C_{17}H_{33}COO)_2$, NaOH, decane, water, ethanol	reaction: 2 h, room temperature or 90 °C	particles morphology: irregular particles aggregates (2–10 µm); needle-shaped (*L*: 200–600 nm, T: 90–150 nm); nearly spherical and hexagonal (*D*: 100–230 nm); spherical and pseudo-spherical aggregates (*D*: 150 nm)
	$Zn(CH_3COO)_2$, heptanes, Span-80, NH_4OH	reaction: 1 h; aging: 2.5 h; drying: in rotary evaporator; calcination: 2 h, 700–1000 °C	hexagonal structure; spherical shape; particles diameter: 0.05–0.15 µm
	$Zn(CH_3COO)_2$, NaOH and KOH, cyclohexane, non-ionic surfactants	reaction: ambient temperature; drying: 24 h, 120 °C	hexagonal structure; particles morphology: solids (164–955 nm, *BET*: 8 m^2/g), ellipsoids (459–2670 nm, *BET*: 10.6 m^2/g), rods (396–825 nm, *BET*: 12 m^2/g), flakes (220–712 nm, *BET*: 20 m^2/g); crystallites size: 32–77 nm; application: as a photocatalyst

Microemulsion	$Zn(NO_3)_2$, NaOH, heptane, hexanol, Triton X-100, PEG400	reaction: 15 h, 140 °C; drying: 60 °C	hexagonal (wurtize) structure; particles morphology: needle (*L*: 150–200 nm, *D*: ~55 nm), nanocolumns (*L*: 80–100 nm, *D*: 50-80 nm), spherical (~45 nm)
	$Zn(NO_3)_2$, oxalic acid, isooctane, benzene, ethanol, diethyl ether, chloroform, acetone, methanol, Aerosol OT	reaction: 1 h; calcination: 3 h, 300 °C	equivalent spherical diameter: 11.7–12.9 nm, *BET*: 82–91 m^2/g; grain size: 11–13 µm
	$Zn(CH_3COO)_2$, Aerosol OT, glycerol, $C_{20}H_{37}NaO_7S$, n-heptane, NaOH, methanol, chloroform	reaction: 24 h, 60–70 °C; drying: 1 h, 100 °C; calcination: 3 h, 300–500 °C	hexagonal wurtize structure, spherical shape (15–24 nm), rods shape (*L*: 66–72 nm, *D*: 21–28 nm)
	$ZnCl_2$, $Zn(CH_3COO)_2$, heptane, BTME (1,2-trimethoxysilyl)ethane, TMOS (tetramethoxysilane), methanol, Aerosol OT, NaOH	reaction: 2–3 h, room temperature or 40 °C; drying: under vacuum overnight; calcinations: 24 h, 700 °C	hexagonal structure, uniformly dispersed small particles, size of particles ~10 nm
Other methods	$Zn(CH_3COO)_2$	thermal decomposition: 350–800 °C	uniform size of particles 20–30 nm
	$Zn(NO_3)_2$, deionized water, HMT (hexamethylenetetramine)	ultrasonic irradiation: 30 min, 80 °C; drying: 2 h, 60 °C	hexagonal wurtize structure, nanorod and nanowire shape (*L*: ~1 µm, *D*: ~160 nm); application: electronic and optoelectronic devices
	micron scale zinc metal powder	feed rate: 1 g/min; plasma power: 1 kW; O_2 flow rate: 2.5 lpm; N_2 flow rate: 12.5 lpm; reaction: 900 °C	nanowires shape (*L*: 1–30 µm, *D*: 5–50 nm) application: as hydrodesulfurization catalyst
	diethylzinc (DEZ), oxygen	helium as a carrier gas	wurtize structure; average particle size: 9 nm
Note: BET surface area calculated based on BET equation; D = particles diameter; L = particles length.			

Tab. 2: Overview of methods of obtaining ZnO [61].

1.5 Applications

1.5.1 Non-electronic fields

Thanks to the physical and chemical properties displayed in the previous chapters, ZnO is exploited for applications ranging from food to rubber industry, from agriculture to electronics, from cosmetics to pharmacy [61] [102] [103].

FIELD	PURPOSE
Rubber Industry	Filler to increase thermal conductivity, curing agent, cross-linking agent
Pharmacy and Cosmetics	Antibacterial, disinfectant, epilepsy and diarrhea medicines, suppositories, anti-inflammatory, anti-itch, dental pastes, healing agent, UV absorber (sunscreen), peeling
Textile Industry	Self-cleaning, water repellent and UV-blocking textiles
Photocatalysis	Photocatalyst for organic pollutants
Electronics	*See below*
Miscellaneous	Concrete filler, Zn silicates (water- and fire-resistant paints) precursor, catalyst for methanol, inks filler, Zn supplement in food, packaging, fungicides, anti-mould, animal feed additive, artificial fertilizer, fingerprint analysis, HCN and H_2S remover from tobacco, removal of S and its compounds from gases, lubricant additive, cell marker, biosensors, immobilizer for proteins or enzymes with low isoelectric point.

Tab. 3: Industrial and research fields where ZnO is utilized and purposes of its use.

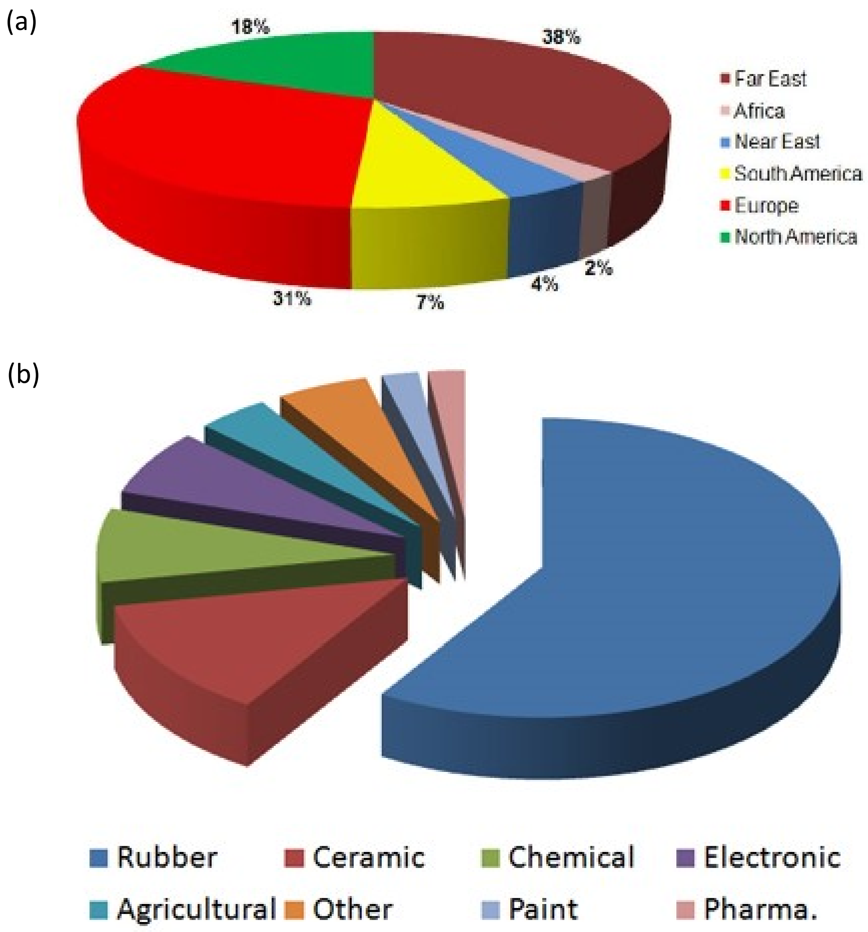

Fig. 19: (a) Use of ZnO for each continent [61] and (b) in the various application fields [103].

1.5.2 ZnO in electronics

- **Zno & GaN**

Crystalline structure and optoelectronic properties of ZnO are similar to gallium nitride's (GaN), reason why in the past the main application of ZnO in the semiconductors field has been as substrate for GaN devices [104]. While the main drawback of ZnO is the already-mentioned lack of control in doping and conductivity (chapter 1.1), the advantages with respect to GaN lie especially in high quality large bulk crystals [104], easier growth technologies, higher exciton energy and higher resistance to radiations [105].

- **Near UV bandgap**

The bandgap of ZnO is 3.37 eV at room temperature [106], which makes this material suitable for light-emitting diodes, laser diodes, photodetectors and other optoelectronic applications in the blue/UV range of spectrum.

- **Bandgap engineering**

  Another interesting point that makes ZnO adaptable for different semiconductor-related applications, is the possibility to engineer its bandgap: in particular by magnesium doping a bandgap increase is achieved [107], while cadmium is employed in order to decrease it [108].

- **High exciton binding energy**

  The ZnO exciton binding energy of $60\,meV$ [104] is high enough to avoid interferences caused by temperature-triggered excitations, since $K_BT \approx 25\,meV$. It can be used, hence, for optical devices based on excitonic effects.

- **Luminescence**

  ZnO also present strong luminescence in the green-white region of the spectrum [21]. The origin of this emission is not clear, but it is often attributed to O vacancies or Zn interstitials [109], even though Zn vacancies appear to be more probable as cause of the green luminescence. This feature is important, however, for in-vacuum fluorescent displays and field emission displays.

- **Gas sensing**

  Owing to surface conductivity variation in the presence of adsorbed species, ZnO is a good material for gas sensing [97] [110]. Whilst the working principle is known to be related to charge transfer between the analyzed substance and sensing oxide, a deep understanding of the surface mechanism has not been achieved yet.

- **I-V characteristic and non linear optics**

  More peculiarities of this material are the strong non-ohmic current-voltage characteristic of polycrystalline ZnO (useful for varistors) [111] and second- and third-order non-linear optical behavior [112].

1.5.3 ZnO in piezoelectric devices

Given the aim of this thesis, it is worth deepening about the use of ZnO for piezoelectric devices.

ZnO present a non-centrosymmetric crystalline structure, which makes it piezoelectric. This property has been widely exploited recently in order to obtain deformation sensors, nanogenerators and nano-energy harvesters. Nanostructured ZnO is one of the most common materials for piezoelectric devices, owing to ease in low temperature synthesis methods with respect to ceramic materials. Moreover, ZnO nanostructures can be easily arranged in aligned configuration, so poling is not needed for piezoelectricity exploitation [113]. Despite this, its use for piezoelectric devices is relatively recent. The first measurements of piezoelectricity in ZnO NRs were carried out by means of Atomic Force Microscope (AFM) by Wang and Song [114]. Nevertheless, the measured quantity was, in this case, the open-circuit voltage and not the current. Because of the presence of spurious effects caused by contacts and capacitance, this type of measurement can result to be tricky, as explained by Alexe *et al.* [115]. Additional lectures [116] [117] helped to clarify some aspects, but this controversy demonstrates the complexity to confidently explain piezoelectricity in such material.

Further studies have been made by means of Transmission Electron Microscopy (TEM) [118]. Despite better reliability of this analysis thanks to the fixed contact between nanorod and electrodes, some points about the possibility of current generation in static conditions still remains unclear [119] [120] [121].

In early ZnO-based piezoelectric devices, zig-zag electrodes were employed with the aim to imitate the function of AFM in piezoelectric characterizations [117] [122] [123]. In some cases, polymers were employed in order to protect ZnO nanostructures from high mechanical stresses [124] [125].

With a view to maximize the piezoelectric output, flexible devices are realized. This is possible because ZnO nanostructures can be grown by low temperature techniques on many different substrates, including flexible polymers. Since the very first work of this kind [126] plenty of flexible devices have been fabricated and placed onto many different deformable surfaces in order to take advantage of mechanical energy, ranging from human to animal body [127], from flags [128] to tires [129] and so on. With regard to this, wearable technologies are evidently particularly interesting [130] [131], since several kind of body movements can be exploited for self-charging portable devices.

Schottky barrier between ZnO and electrode (Au or Pt for example) was initially considered essential for the device to operate [114] [132], but this theory has been overcome by non-contact arrangements with ZnO completely immersed within insulating polymers [133] [134].

Recently by putting in contact ZnO with p-type materials (such as PEDOT:PSS or $CuSCN$), new devices based on p-n junction have been developed [135] [136] with the aim to improve the piezoelectric output.

Vertical arrangement is not the only feasible configuration: devices with horizontally aligned ZnO NRs have been prepared [137] [138] in order to take advantage of in-plane substrate deformations. In any case, vertical arrangement has the advantage to be achieved by easier synthesis.

Even though piezoelectric effect can arise from other ZnO nanostructures, NRs and nanowires are able to maximize deformation owing to the strong anisotropic structure, so the piezoelectric output. Furthermore, they are synthesized by easy and somehow “standard” techniques.

With regard to the device efficiencies, given the dependence of output power by voltage and current, both have to be maximized. Some of the devices presented above show high open-circuit voltage but low short-circuit current, while it is opposite for others. It must be said that lower values can be ascribed to the way the single measurements are executed, such as the different spatial distribution of deformations, stress intensities and mechanical modulus of each part of the device structure. Hence, some standardization of piezoelectric characterizations should be fulfilled [113].

Deeper dissertation about piezoelectric measurements will be given in chapters 4 and 5.

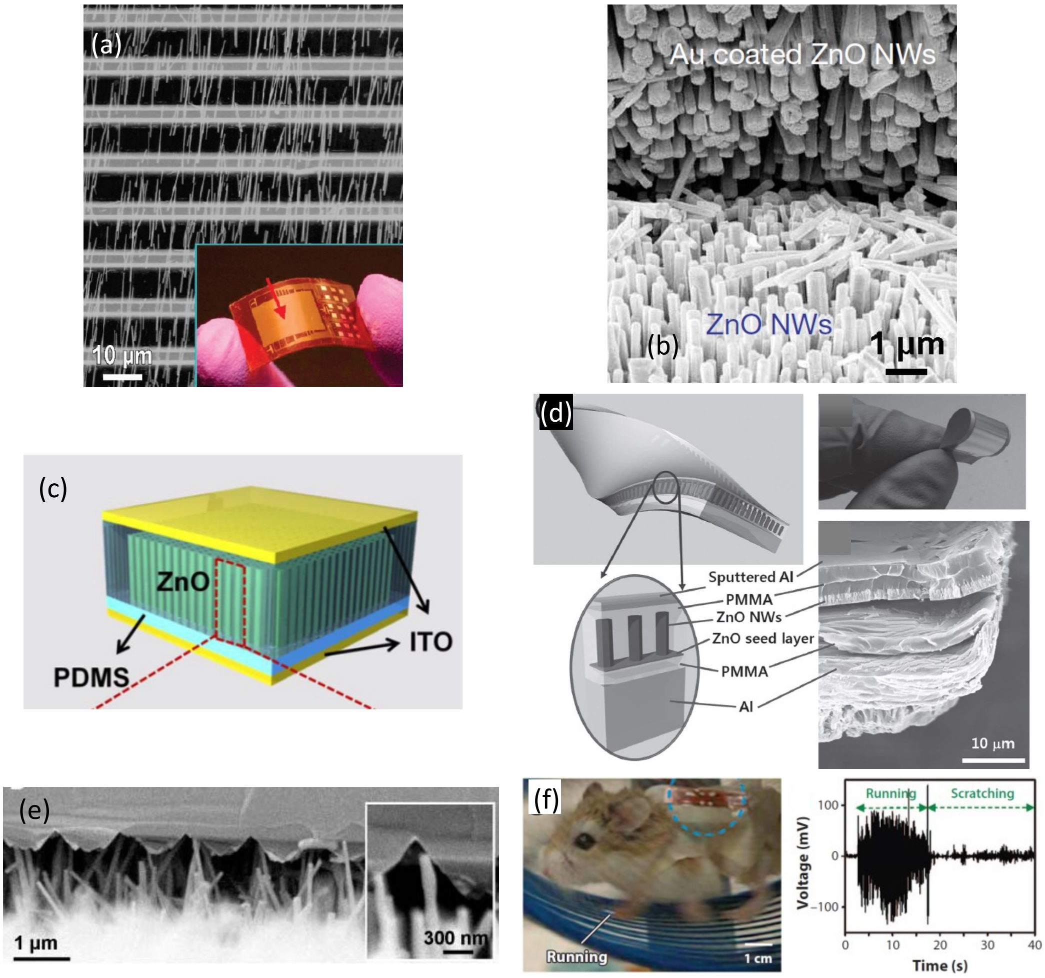

Fig. 20: (a) Horizontally arranged ZnO NRs [137]. (b) ZnO are coated with Au in order to obtain nanostructured Schottky barrier [132]. (c, d) Configurations where ZnO NRs are not in contact with metallic electrodes [134] [128]. (e) Zig-zag electrode [117]. (f) ZnO-based device applied to a mouse back and its piezoelectric response [127].

2 Basics of crystal growth

2.1 Nucleation

2.1.1 Classical homogeneous nucleation

According to simple solubility considerations, a precipitate is formed when the product of the concentrations of anions and cations exceeds the solubility product. From another point of view, phase transformation occurs when the free energy of the new phase is lower than that of the initial (metastable) phase. However, there are many examples where the ion product exceeds K_{sp}, yet no precipitation occurs. This is known as the phenomenon of supersaturation. The solubility product also does not provide information on how the particles of the precipitate form. Nucleation involves various physical processes, and both thermodynamic and kinetic aspects must be considered.

Homogeneous nucleation can occur due to local fluctuations in the solution, whether in concentration, temperature, or other variables. The first stage in growth is collision between individual ions or molecules to form embryos (embryos are nuclei that are intrinsically unstable against re-dissolution). Embryos grow by collecting individual species (may be ions, atoms, or molecules in general) that collide with them. They may also grow by collisions between embryos; however, unless the embryo concentration is large, this is less likely [139].

These embryos may redissolve in the solution before they have a chance to grow into stable particles (nuclei). Because of the high surface areas and, therefore, high surface energies of such small nuclei, they are very reactive and thermodynamically unstable against re-dissolution (critical nuclei). They may, however, be kinetically stabilized by low temperatures, which increase their lifetime, possibly enough for them to grow to a size where they are thermodynamically stable. This is an important reason why smaller particles can be formed at lower temperatures in a precipitation reaction; the subcritical embryos last long enough to grow into stable particles, while at higher temperatures they would redissolve, reducing the density of nuclei. This results in an increase of the particle size, since there is more reactant per nucleus.

The homogeneous nucleation process is the result of the competition between surface and bulk energies, E_S and E_V:

$$E_S = 4\pi r^2 \sigma$$

$$E_V = \frac{4}{3}\pi r^3 \Delta G_V$$

$$\Delta G = 4\pi r^2 \sigma + \frac{4}{3}\pi r^3 \Delta G_V$$

where σ is the surface energy per unit area and ΔG_V the volume free energy. ΔG_V is dependent upon temperature T, Boltzmann's constant k_B, supersaturation S and molar volume v using the following equation:

$$\Delta G_V = \frac{-k_B T\, ln(S)}{v}$$

Due to the surface free energy always being positive and the bulk free energy always negative, a maximum of the total free energy with respect to radius can be identified, corresponding to the critical radius r_{crit}. This is the size where the embryo (critical nucleus) has a ½ chance of either redissolving or growing into a stable nucleus. By differentiating ΔG with respect to radius and setting it to zero, critical radius is found, so the critical free energy (activation energy barrier):

$$\frac{d\Delta G}{dr} = 0$$

$$r_{crit} = -\frac{2\sigma}{\Delta G_V} = \frac{2\sigma v}{k_B T\, ln(S)}$$

$$\Delta G_{crit} = \frac{4}{3}\pi \sigma r_{crit}^2$$

The rate of nucleation of N particles in time can be described by means of Arrhenius-type equation [140]:

$$\frac{dN}{dt} = A\, e^{-\frac{\Delta G_{crit}}{k_B T}} = A\, e^{-\frac{16\pi\sigma^3 v^2}{3{k_B}^3 T^3\, (\ln(S))^2}}$$

where A is the pre-exponential factor. As shown by the last equation, supersaturation, temperature and surface free energy are the variables that can

significantly change nucleation rate. The strongest contribution, however, comes from supersaturation: this dominancy was studied in 1926 by Volmer [141]. Calculations showed that, for the specific case of a supercooled water vapor, if supersaturation rises from $S = 2$ to $S = 5$ the time needed for the spontaneous appearance of stable nuclei hugely varies from 10^{62} years to 10^{-13} seconds (about 82 orders of magnitude). σ variation by means of surfactants can strongly affect nucleation rate as well [142].
The balance between E_S and E_V is shown in fig. 21. The typical size of r_{crit} is about 100 units, between 1 and 2 nm in diameter. Solvent molecules can adsorb onto the embryos too, and change their surface energy: the critical radius will depend, therefore, not only on the material of the nucleating phase but also on the solution content.

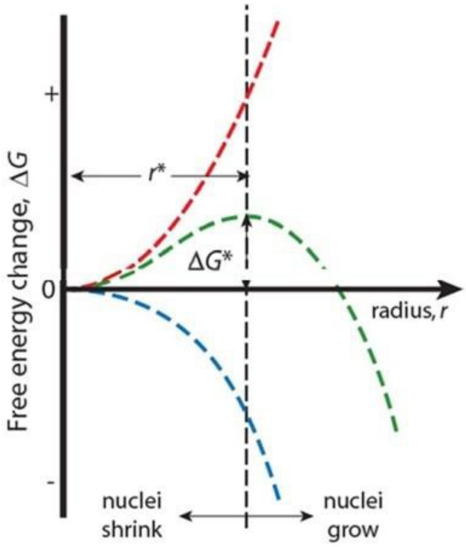

Fig. 21: Balance between surface and volume energy as a function of particle dimension.

2.1.2 Classical heterogeneous nucleation

Heterogeneous nucleation occurs at the interface between the solution and a body presenting different state of matter, such as solid impurities or the container walls.
In this type of nucleation subcritical embryos (or even individual ions) are adsorbed onto a solid substrate surface. The energy required for the formation of an interface between the embryo and the solid substrate is usually less than that required for homogeneous nucleation, where no such interface exists. Therefore, heterogeneous nucleation is energetically preferred over homogeneous nucleation and can occur near equilibrium saturation conditions, compared with the high degree of supersaturation often required for homogeneous nucleation. These subcritical nuclei can grow, either by

surface diffusion or by material addition from solution. It should also be noted that nuclei that are subcritical in solution may be supercritical when adsorbed onto a substrate. This is a consequence of reduced contact between nucleus and solution as well as stabilization of the adsorbed nucleus [139]. It was noted earlier that even individual ions may adsorb onto a surface. More specifically, depending on the surface chemistry of the substrate, individual ions or molecular species may actually be chemisorbed, creating a nucleus for reaction and further growth. Pure homogeneous nucleation is probably less common that might appear from the above discussion. Because of the greater ease of nucleation on a solid phase than homogeneously, any solid matter in the solution will act as a preferential nucleation center, so it can be considered as a “catalyst”.

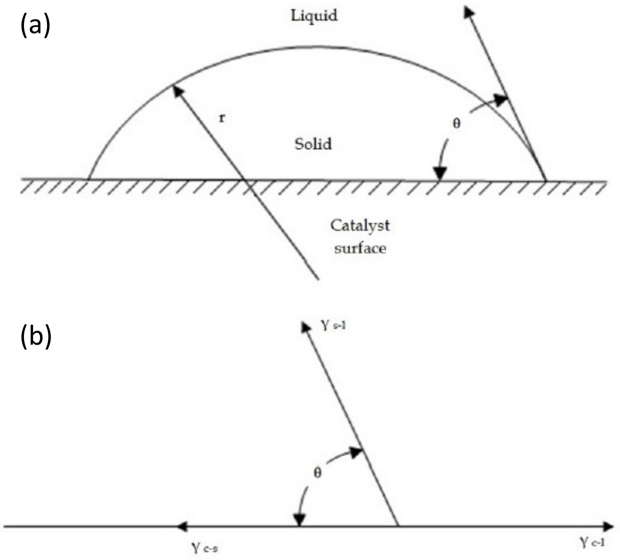

Fig. 22: (a) Nucleus on a catalyst surface with its contact angle θ. (b) Energies related to the different interfaces.

Assuming a spherical nucleus forming on the solid surface, the surface energy is calculated as

$$2\pi r^2(1-\cos\theta)$$

for the solid-liquid interface, and

$$\pi r^2(1-\cos^2\theta)$$

for the catalyst-solid interface, where r is the radius of curvature of the nucleus and θ the contact angle.
The free energy of the surface can be written as

$$\Delta G_{surf} = 2\pi r^2(1 - \cos\theta)\gamma_{s-l} + \pi r^2(1 - \cos^2\theta)(\gamma_{c-s} - \gamma_{c-l})$$

where γ_{s-l}, γ_{c-s} and γ_{c-l} are the solid-liquid, catalyst-solid and catalyst-liquid interfacial energies, respectively.
The relation between these three terms can be expressed as following:

$$\gamma_{c-l} = \gamma_{c-s} + \gamma_{s-l}$$

The volume of the nucleus can be written as a function of its geometrical values:

$$V = \frac{4}{3}\pi r^3\left[\frac{(2 + \cos\theta)(1 - \cos\theta)^2}{4}\right] = \frac{4}{3}\pi r^3 f(\theta)$$

and the variation of volumetric Gibbs free energy

$$\Delta G_{vol} = \frac{4}{3}\pi r^3 \Delta G_V f(\theta)$$

It is worth noting that by differentiating ΔG with respect to radius and setting it to zero, as did previously in the case of homogeneous nucleation, the expression of the critical radius is the same of the homogeneous case:

$$r_{crit} = -\frac{2\gamma_{s-l}}{\Delta G_V}$$

whereas the critical Gibbs free energy ΔG_{crit} is strongly influenced by the wettability:

$$\Delta G_{crit} = \frac{16}{3}\frac{\pi\gamma_{s-l}^3}{\Delta G_V^2} f(\theta)$$

being $f(\theta)$ the ratio between the volume of the nucleus and the volume of a sphere with the same radius of curvature.
It can be finally affirmed that the critical Gibbs free energies in the two cases of homogeneous and heterogeneous nucleation only differ by a geometrical factor, strongly dependent on the wettability between nucleus and catalyst substrate [143] [144]:

$$\Delta G_{crit}^{hetero} = f(\theta)\Delta G_{crit}^{homo}$$

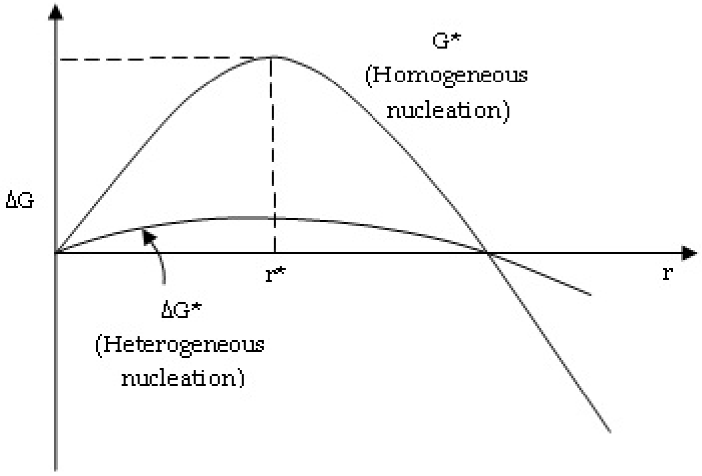

Fig. 23: Free energies involved in the homogeneous and heterogeneous nucleation. Critical radius is the same in both cases, while the energy barrier is lower in the heterogeneous case thanks to wettability.

2.1.3 Non-classical multistep nucleation

The classical model of nucleation with a single energy barrier to overcome has been called into question by recent studies, about magnetite and $CaCO_3$ especially, that reveal much more complex mechanisms. The formation of intermediate metastable stages seems to be more realistic, with aggregation of pre-nucleation clusters [145], formation of dense liquid-liquid phase [146] and phase transitions [147]. Pre-nucleation clusters could even be more stable than single ions themselves [148] and they have been observed in undersaturated conditions. These phenomena are not completely understood yet, but the key is the Gibbs free energy of each possible configuration, whose minima (stability) are strongly affected by the system parameters, their slight fluctuations and even by the experimental conditions as well.

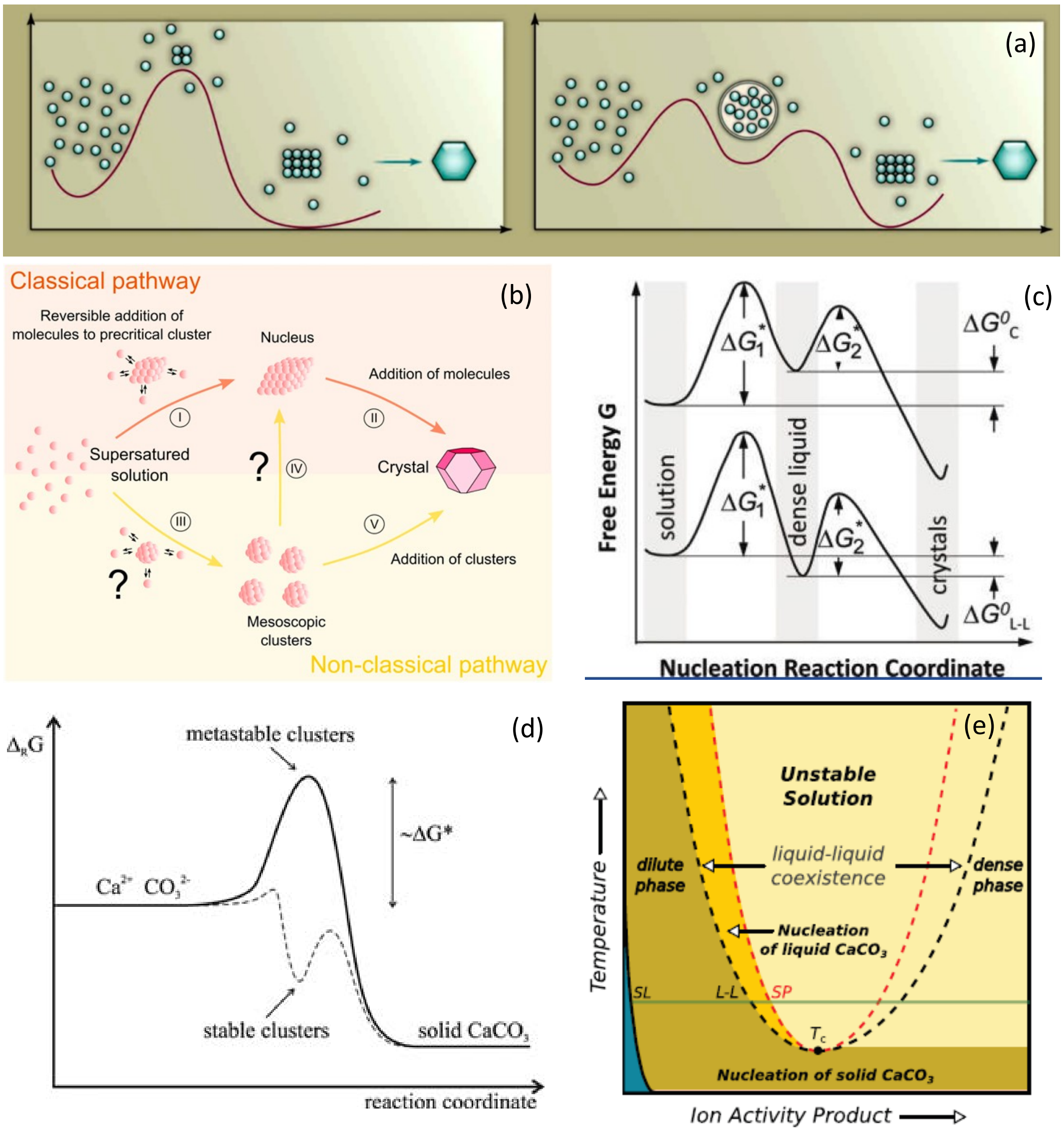

Fig. 24: (a, b) Classical vs. non-classical nucleation pathways [149] [150]. (c, d) Stable and metastable species correspond to free energy minima; pre-nucleation clusters could own higher stability with respect to single ions themselves [148]. (e) Phase stabilities as a function of temperature and ion activity; the liquid-liquid phase is one of the possible metastable conditions [146].

2.1.4 Successive Ionic Layer Adsorption and Reaction (SILAR)

A particular type of heterogeneous nucleation is realized by the so-called Successive Ionic Layer Adsorption and Reaction (SILAR).
Semiconductor films are deposited by solution methods since a long time. Advantages lie in simple setups, low cost and low temperatures. Some advantages shows up as well, such as the interference of solvents in the process.
SILAR consists in a successive immersion of a substrate in a cationic solution first, then in an anionic solution; this process is repeated many times in order to fulfill a controlled layer-by-layer growth by deposition and reaction of cationic and anionic precursors on the substrate.
This method was described for the first time by Nicolau in 1985 [151] and it has been used especially for the growth of oxide and chalcogenide thin films.
The growth takes place in four sequential steps:

1) The substrate is immersed in a solution containing the cations, which are adsorbed on the substrate surface. A double layer is formed with cations inside and anions outside;
2) The substrate is rinsed with distilled water, in order to remove unreacted precursor;
3) The substrate is immersed in a solution containing the anion that will form the specie with the previously deposited cation;
4) The substrate is rinsed with distilled water once again.

The process is repeated as many times as is needed for the formation of a thin film with controlled thickness.

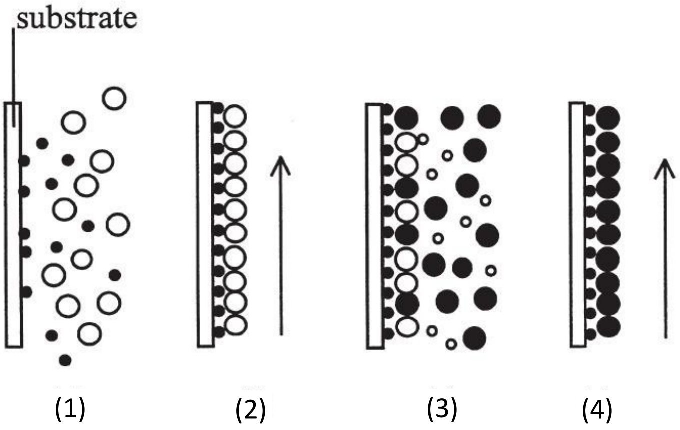

Fig. 25: The four steps of the SILAR process.

The total reaction can be expressed as:

$$mM^{n+}_{(aq)} + nA^{m-}_{(aq)} \rightarrow M_mA_{n(s)}$$

Among the factor mainly influencing the film growth one can include concentrations, pH, nature and dimension of the anion, and temperature, which conditions ion mobility and thermodynamics of the reaction.
The main advantage of this technique is the possibility to work at low temperatures and atmospheric pressure. Furthermore, the thickness can be easily controlled depending on the number of deposition cycles.
The local supersaturation needed for the growth is found at the interface, so it is possible to keep low concentrations, avoiding homogeneous nucleation and the formation of precipitates.
Some advantages exist though, such as low velocity with respect to some vapor phase techniques.
A typical thickness increment for each deposition cycle is about 1 ÷ 3 Å, which is higher, for instance, than the value achievable by the atomic layer deposition (ALD), the gas-phase equivalent of SILAR; nevertheless, as already said, the time needed for SILAR is higher.
More observed disadvantages are the instability of some type of substrates in aqueous and alkaline solutions, as well as oxygen contamination in the case of chalcogenides.
The most used methods for the growth of films by SILAR are essentially two [152]:

- The most common is the deposition of the ionic hydroxide of the metal, followed by thermal treatment, in order to convert the hydroxide into oxide;
- The use of hydrogen peroxide as anion source and transformation of the metal peroxide into oxide.

2.2 Growth

The growth of nanoparticles mainly depends on two phenomena: monomer diffusion and surface reaction. Fick's first law can be used for modelling the diffusion-driven growth:

$$J = 4\pi x^2 D \frac{dC}{dx}$$

where J is flux of monomers, x the radius, D diffusion coefficient and C concentration. If δ is the distance between the particle surface and the bulk solution (where concentration of monomers is homogeneous), C_b the bulk concentration and C_i the concentration at the particle/liquid interface, then the Fick's first law can be rewritten as

$$J = \frac{4\pi Dr(r+\delta)}{\delta}(C_b - C_i)$$

If the solution is in a steady state, J is constant and irrespective of x, so the integration of $C(x)$ from $(r+\delta)$ to r gives

$$J = 4\pi Dr(C_b - C_i)$$

A similar equation can be written in the case of surface reaction, with the rate of a surface reaction k independent from the particle size:

$$J = 4\pi kr^2(C_i - C_r)$$

Here C_r is the solubility of the particle.
Either monomer diffusion or surface reaction can represent the limiting factor of the process. In the first case the change of particle size in time is

$$\frac{dr}{dt} = \frac{Dv}{r}(C_b - C_r)$$

while in the second case

$$\frac{dr}{dt} = kv(C_b - C_r)$$

Stable nuclei can increase in size by several ways. One is a continuation of the process of embryo growth discussed earlier: adsorption of ionic species from the solution onto the nucleus. Crystal growth of this type can be considered a self-assembling process. This process can continue until either all the ions of any type are used up or growth is blocked, *e.g.*, by aggregation or by blocking of the crystal surface by a foreign adsorbed species.

Another mechanism for crystal growth is known as Ostwald ripening. If a small nucleus or embryo is close to a larger crystal, the ions formed by (partial) dissolution of the smaller and less stable crystal can be incorporated into the larger crystal. As the smaller crystal becomes even smaller, its dissolution will become ever more favorable and eventually it will disappear. The result is that the larger crystals grow at the expense of the smaller ones [153].

If the concentration of particles is sufficiently high, then the probability of collisions between these particles becomes high. This can result in either aggregation or coalescence. When two particles approach each other, the Van der Waals (VdW) force of attraction between them will often cause them to stick together. This can continue until a large particle (large in relation to the original particle size) comprising the individual particles has formed. This is the process of aggregation, and the resulting large particle is called aggregate (in colloidal chemistry, the alternative terms of flocculation and floc are often encountered). The properties of the aggregate may be similar to those of the individual particles in some ways (such as X-Ray diffraction peak broadening, quantum size effects) and very different in others (*e.g.*, light scattering, sedimentation). In an aggregate, there are grain boundaries between individual crystallites. However, in some cases, particularly if the temperature is high enough to allow appreciable diffusion of the crystal atoms, surface diffusion may occur where two (or more) particles have aggregated, resulting in the formation of a neck. This is termed *coalescence* and may continue until one large particle is formed from the original two or more particles [139].

If nucleation occurs in a very short time, whereas growth occurs separately, often over a much longer time but without further nucleation, then the size distribution is likely to be narrow, since all the original nuclei should be of similar size and grow at the same rate. The opposite case, where nucleation and growth occur simultaneously, usually results in a wide size distribution. Homogeneous nucleation normally requires a supersaturated solution, while growth can occur close to the saturation concentration. Therefore, rapid nucleation can occur if a large supersaturation is rapidly reached. This nucleation lowers the concentration of reactants below that needed to cause further nucleation. If one of the reactants is supplied at a low concentration after nucleation has occurred (such as by *in situ* homogeneous formation in the solution), then growth can occur without further nucleation, resulting in a narrow size distribution [154].

2.3 Dimensional control

The requirements for monodispersity are a high rate of nucleation (leading to the burst formation of nuclei in a short period), an initial fast rate of growth of these nuclei to reduce the concentration below the nucleation concentration rapidly and an eventual slow rate of growth leading to a long growth period compared to the nucleation period.

While investigating the formation of sulfur suspensions, La Mer [153] postulated the necessity of temporal separation of the nucleation and growth phases for the formation of monodisperse colloids. La Mer burst nucleation is described with reference to the La Mer plot shown below, which describes the evolution of supersaturation S with time, where supersaturation is defined as the ratio between the monomer concentration in the solution and the surface density of adsorbed species at the equilibrium.

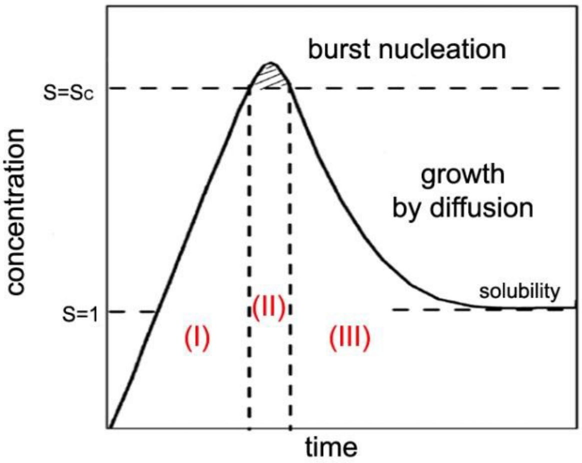

Fig. 26: La Mer diagram [153].

During phase I, the supersaturation remains below the critical supersaturation required for the kinetic barrier to homogenous nucleation to be surpassed and nucleation to occur ($S = S_C$). During phase II some event increases the supersaturation of solution above the critical level, and the rate of nucleation increases to some finite level. In the case where further monomer is not supplied to replace that consumed in nucleation, the supersaturation will eventually fall back below the critical supersaturation, causing further nucleation to cease. Phase III is now entered, where monomer continues to be consumed solely by growth of existing particles until eventually equilibrium is reached ($S = 1$). Provided that Phase II (nucleation) is quick and temporally distinct from Phase III (growth), all nuclei emerge from Phase II with a uniform size, a condition identified as a prerequisite for monodispersity of particles at the end of Phase III (growth) [155]. When the monomer concentration falls below the critical level for nucleation (critical supersaturation level), nucleation ends. A colloidal particle growth can be considered as a sequence of monomer diffusion towards the surface followed by reaction of the monomers at the surface of the nanocrystal.

The interfacial energy (the energy associated with an interface due to differences between the chemical potential of atoms in an interfacial region and atoms in neighboring bulk phases) plays a key role in the growth process. For a solid species present at a solid/liquid interface, the chemical potential of a particle increases with decreasing particle size and the equilibrium solute concentration for a small particle is much higher than for a large particle, as described by the Gibbs–Thompson equation [156]:

$$ln\left(\frac{S_C}{S_\infty}\right) = \sigma V\left(\frac{R_1^{-1} + R_2^{-1}}{kT}\right)$$

where S_C and S_∞ are the solubility of a curved solid surface and a flat surface respectively, σ is the surface energy, V the volume of the particle and R the curvature radii of the surface/particle**.** The equilibrium concentration of the nanocrystal in the liquid phase is dependent on the local curvature of the solid phase. The resulting concentration gradients lead to transport of the solute from the small particles to the larger particles. Differences in the local equilibrium concentrations due to variations in curvature, concentration gradients provide the driving force for the growth of larger particles at the expense of smaller particles [157]. These coarsening effects, controlled by either mass transport or diffusion, are often referred as the Ostwald ripening process. It is the most predominant growth mechanism and was first quantified by Lifshitz and Slyozov [158], followed by a related work by Wagner [159], known as the LSW theory. Beside the theoretical formulation, the key idea of separating the nucleation stage and growth process in time is often exploited to obtain nearly monodisperse particles. In most of the cases, synthesis is carried out in recent times by injecting one of the components into the remaining ones, in a very short time. This is to ensure that the entire nucleation takes place in that short time, followed by a much slower growth process, thereby attempting to separate the two stages temporally. Therefore, the key to achieve efficient control of particle growth, is to decouple the nucleation and growth processes. Primary particles grow by addition of soluble species coming from the solution. These species attach themselves at the surface and, if necessary, diffuse along the surface to the position corresponding to a minimum energy.

Nanometric particles are subject to Brownian motion and hence often collide with one another. Then they tend to associate via either weak bonds (agglomeration) or strong bonds (aggregation) to form larger particles. This is the well-known phenomenon leading to flocculation in colloidal dispersions. To avoid such processes, which lead to the formation of polydispersed powders, collisions between primary particles must be avoided [160].

VdW forces are the primary source of attraction between colloidal particles and they are always present between particles of similar composition. Therefore, a colloidal dispersion is considered to be stable only when a sufficiently strong repulsive force counteracts VdW attraction [161]. There are three different possible origins for VdW forces: permanent dipole-permanent dipole (Keesom) forces, the permanent dipole-induced dipole (Debye) interactions and transitory dipole-transitory dipole (London) forces. The first two are very short-range interactions, but the London forces act at longer range. Since only London forces contribute to the long-range attraction between colloidal particles, the magnitude and range of the Van der Waals–London (VdWL) attraction are decisive in determining strategies for stabilizing colloid particles. For many colloid systems, the range of significant VdWL attraction is between 5 and 10 nm. Since there are always strong, long-range attractive forces between similar colloidal particles, it is necessary to provide a long-range repulsion between the particles in order to impart stability. This repulsion should be at least as strong as the attractive force and comparable in range of the attractive interaction. Stability can be obtained by surrounding colloidal particles:

- with an electrical double layer (electrostatic or charge stabilization).
- with adsorbed or chemically attached polymeric molecules (steric stabilization).

Combination of the first two stabilization mechanisms lead to electro-steric stabilization (ionic polymers).

An effective way to counterbalance the VdWL attraction between colloidal particles in polar liquids is to provide the particles with Coulombic repulsion. In liquid dispersion media, ionic groups can adsorb to the surface of a colloidal particle through different mechanisms to form a charged layer. To maintain electroneutrality, an equal number of counter-ions with the opposite charge will surround the colloidal particles and give rise to overall charge-neutral double layers. Charge stabilization, is provided by the mutual repulsion between these surrounding double layers.

Charge stabilization is not effective in media of low dielectric constant (the vast majority of organic solvents), and steric stabilization is required for maintaining dispersed particles in a stable non-flocculated state. Steric stabilization relies on the adsorption of a layer of polymer chains onto the surface of the particle. For polymers with molecular weights > 10000, the chain dimensions are comparable to, or in excess of, the range of the VdWL attraction. Hence, as long as they can generate repulsion, these polymer molecules can be used to impart colloid stability.

As particles approach each other these adsorbed polymeric chains intermingle and in so doing they lose a degree of freedom which they would otherwise possess [160] [155]. This loss of freedom is expressed, in thermodynamic terms, as a reduction in entropy, which is unfavorable and provides the necessary barrier to prevent further attraction. Alternatively, one can consider that, as the chains intermingle, solvent is forced out from between particles. This leads to an imbalance in solvent concentration, which is resisted by osmotic pressure tending to force solvent back between the particles, thus maintaining their separation. The use of a steric stabilizer should be preferable rather than an electrostatic one. However, steric stabilization has several distinct advantages: it is relatively insensitive to the presence of electrolytes (while the electrostatic one is strongly dependent on the ionic strength of the solution) and is effective in both aqueous and non-aqueous dispersion media (since it is unaffected by the solvent dielectric constant) [154].

3 Growth of 1D ZnO crystals by aqueous chemical bath deposition

The most common method for the growth of ZnO NRs in chemical solution is a SL-assisted chemical bath deposition (CBD) in alkaline aqueous solution. The reasons for the success of this approach are the low cost, ease of synthesis, the use of water as solvent and low temperature.

For the growth of ZnO, Zn acetate and nitrate are the most common Zn precursors.

Anisotropic wurtzitic ZnO grown along the c axis presents high energy polar (0001) and (000$\bar{1}$) surfaces which are Zn^{2+}- and O^{2-}-terminated, respectively. Due to this, incoming precursor in solution tends to preferentially attach to these polar surfaces, in order to minimize surface energy. Therefore, during growth alternate Zn^{2+}- and O^{2-}-terminated layer are formed [162], until the reaction is stopped by the intervention of an event such as lack of precursors, low kinetic (low temperature), addition of a capping agent or change of electrical properties of the solution.

3.1 Growth in alkaline solution

ZnO is an amphoteric oxide with isoelectric point of about 9.5 [163] and crystallizes by hydrolysis of Zn salts in basic solutions. Depending on pH and temperature of the solution, Zn^{2+} can form different intermediates, whose dehydration leads to the formation of ZnO (fig. 28) [164].

Normally divalent metal ions do not hydrolyze in acidic environment [165] [166] so alkaline solution is needed in order to achieve Zn^{2+} hydrolysis for the first step of formation of ZnO.

The solubility of ZnO generally increases with alkali concentration and temperature and a growth zone can be identified depending on pH [166].

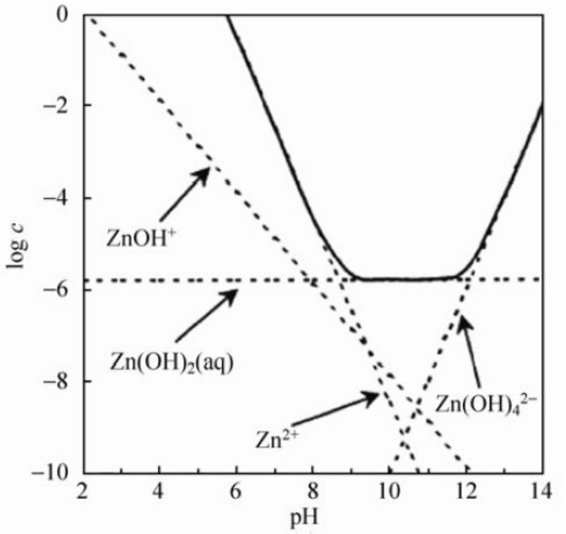

Fig. 27: Phase stability diagram for $ZnO_{(s)}$-H_2O system at 25 °C as a function of precursors concentration and pH. The dashed lines denote the thermodynamic equilibrium between Zn^{2+} soluble species and the corresponding solid phase.

The main reactions involved in the growth process are the following [167] [168]:

$$Zn^{2+} + 2OH^- \leftrightarrow Zn(OH)_2$$

$$Zn(OH)_2 + 2OH^- \leftrightarrow [Zn(OH)_4]^{2-}$$

$$[Zn(OH)_4]^{2-} \leftrightarrow (ZnO_2)^{2-} + 2H_2O$$

$$(ZnO_2)^{2-} + H_2O \leftrightarrow \boldsymbol{ZnO} + 2OH^-$$

$$\boldsymbol{ZnO} + OH^- \leftrightarrow ZnOOH^-$$

The different intermediates can be dominant depending on the reaction conditions.

The process can be described as following: initially Zn^{2+} and OH^- ions coordinate each other and they undergo dehydration by proton transfer, forming $Zn^{2+} \cdots O^{2-} \cdots Zn^{2+}$ bonds and leading to the formation of $[Zn_x(OH)_y]^{(2x-y)+}$ aggregates, which exhibit octahedral coordination. At the beginning these contain less than 50 ions and the formation of O^{2-} ions provoke modifications inside the aggregates.

Water molecules formed by dehydration migrate in solution as the process goes on. When the aggregates reach the quantity of about 150 ions, in their central region wurtzitic ZnO domains start to appear.

Therefore, the nucleus of the aggregate comprehends only Zn^{2+} and O^{2-} while, at the outer surface, Zn^{2+} and OH^- are present.

Aggregates with more than 200 units show nanometric nuclei, which grow increasingly as further dehydration occurs [169].

It is important to underline that O^{2-} ions in the aforementioned reactions does not come from water, but from the basic species; hence the presence of water as solvent is not essential [170], but also alcohols [171] [172] [173] and other ionic solvents [174] [175] can be used.

The aspect ratio of the NRs can be tuned by changing the concentration of OH^- (so the pH) and reaction time.

The growth of inorganic polar nanocrystals is sensitive to the solvents and their morphology can be controlled by tuning the vapor pressure of the solvents, as well as the reactions taking place at the crystal/solvent interface [171]. Solvents with higher polarity interact preferentially with the polar facets of the ZnO crystal, inhibiting the action of precursors and reducing the aspect ratio.

The alkaline environment can be obtained also by means of both strong ($NaOH$, KOH) [166] and weak (NH_3) [176] bases. Ammonia can mediate reactions by reversely stabilizing Zn^{2+}. As the reaction proceeds, Zn^{2+} is gradually consumed and the stable ammonia-complex of Zn with formula $[Zn(NH_3)_4]^{2+}$ decomposes [177], maintaining a steady concentration of Zn^{2+} and allowing to keep a relatively low supersaturation. At temperatures between 70 and 95 ℃ this inhibits precipitation and homogeneous nucleation in solution, giving advantage to the substrate-assisted heterogeneous nucleation [162].

Another important factor is the concentration of O_2 dissolved in solution. In the presence of H_2O_2, for instance, H_2O and O_2 are formed and sharp NRs are obtained [178], whereas jagged NRs arise if oxygen is eliminated by boiling water [162].

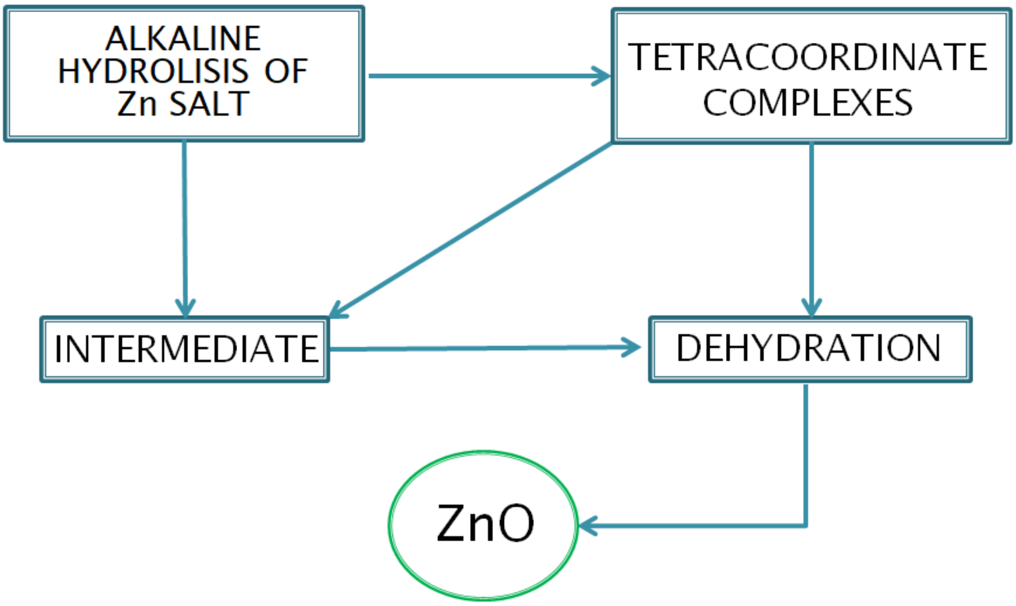

Fig. 28: General mechanism of ZnO growth by alkaline solution.

3.2 The role of hexamethylenetetramine

HMTA (formula $(CH_2)_6N_4$) seems to be essential for the anisotropic growth of 1D ZnO crystals along its c axis [179] [180].
HMTA is a non-ionic heterocyclic tertiary amine, as shown in the structure formula.

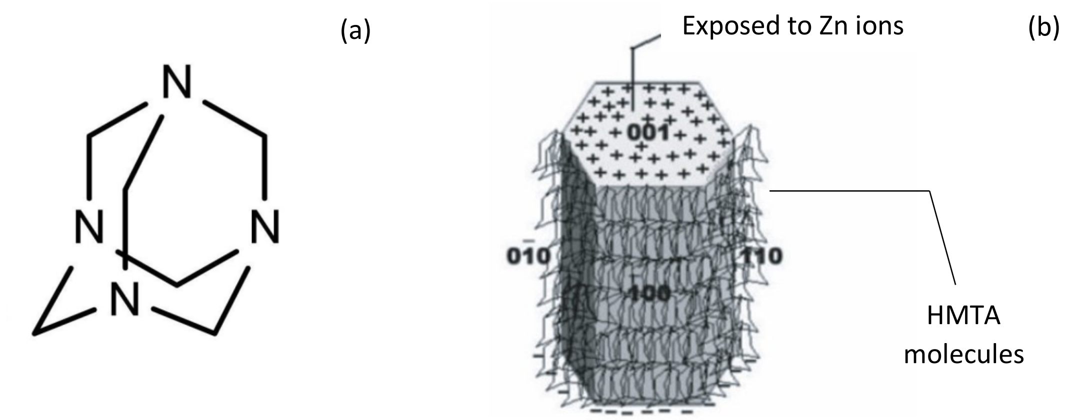

Fig. 29: (a) Structure of the HMTA molecule. (b) Role of the polarity of HMTA in the 1D growth oh ZnO NRs [181].

Its role in the growth of ZnO NRs is still unclear, even though some interesting theories have been proposed. The most accredited are three:

1) being HMTA a non-polar molecule, it interacts with the non-polar $\{10\bar{1}0\}$ faces, inhibiting their growth [181];
2) owing to its nature of weak base, it acts as pH buffer and as source of OH^-. This time it is not the alkali that provides O^{2-}, but water [182];
3) it acts as bidentate Lewis base that coordinates and bridges two Zn^{2+} ions [183].

The decomposition of HMTA implies a decrease of free energy, due to both the increase of entropy related to the loss of rigidity of the HMTA molecule and the augment of the number of molecules in the system.
The HMTA hydrolysis rate decreases by increasing pH, and *vice versa* [182].
HMTA rapidly hydrolyzes in water, generating formaldehyde $HCHO$ and ammonia.

The main reactions that take place in the presence of HMTA are the following [162] [184]:

$$(CH_2)_6N_4 + 6H_2O \rightarrow 6HCHO + 4NH_3$$

$$(CH_2)_6N_4 + Zn^{2+} \rightarrow [Zn(CH_2)_6N_4]^{2+}$$

$$[Zn(CH_2)_6N_4]^{2+} + 2OH^- \rightarrow \boldsymbol{ZnO} + 4NH_3 + H_2O$$

$$NH_3 + H_2O \rightarrow (NH_4)^+ + OH^-$$

$$Zn^{2+} + 4NH_3 \rightarrow [Zn(NH_3)_4]^{2+}$$

$$Zn^{2+} + 4OH^- \rightarrow [Zn(OH)_4]^{2-}$$

$$[Zn(OH)_4]^{2-} \rightarrow \boldsymbol{ZnO} + H_2O + 2OH^-$$

$$Zn^{2+} + 2OH^- \rightarrow Zn(OH)_2$$

$$Zn(OH)_2 \rightarrow \boldsymbol{ZnO} + H_2O$$

Here too, the reactions are sensitive to different parameters such as precursors concentration, temperature and time. Generally, the first determines the NRs density, whereas temperature and time direct morphology and aspect ratio. By increasing time, higher aspect ratio is achieved [185] [186].

At atmosphere temperature the kinetic of reaction is very low, so it is favorable to immerse the substrate (covered with a ZnO SL beforehand) in an aqueous alkaline solution with a Zn salt and HMTA, at temperatures up to 95 °C.

Theoretically, ammonia would be sufficient to synthesize ZnO NRs, being the direct product of hydrolysis of HMTA, but perhaps the combined advantages of non-polarity and buffering power arising from HMTA produce better results. The formation of ammonia is, nevertheless, a crucial step; if HMTA would hydrolyze giving abundant OH^- directly, a big quantity of Zn hydroxide would be formed, which will precipitate subtracting precursor [187].

Ammonia plays two central roles: first of all, it creates the alkaline environment that is necessary for $Zn(OH)_2$ to form; furthermore, it coordinates Zn^{2+} ions stabilizing them in the solution.

Finally $Zn(OH)_2$ dehydrates to form ZnO by undergoing thermal treatment [180], microwaves [188], ultrasounds [189] or sunlight [190].

3.3 Seed layer-assisted growth

One of the most important advantages of the wet chemical synthesis is that by exploiting a ZnO SL it is possible to grow ZnO NRs on a remarkable variety of substrates, ranging from silicon [180] to polydimethylsiloxane (PDMS) [191], from polyurethanes [192] to paper [193], from organic [132] to carbon fibers. During growth, the NRs preferentially nucleate between the corners of grain boundaries [194]. The order of magnitude of the NRs width is around 100 nm, due to the dimensions of the SL grains, while their length can reach up to 10 μm [195].

By the energy point of view, homogeneous and heterogeneous nucleation are in competition, but the activation energy of the latter is significantly lower, reason why the heterogeneous nucleation is favorite even at lower supersaturation levels with respect to the values needed for homogeneous nucleation (see chapter 2).

The particles of the SL that are oriented toward the [0001] direction possess superficial polarity, as already mentioned; so the precursors preferentially tend to react on these surfaces, in order to reduce polarity (so the energy of the system). A model has been proposed to explain the formation of an aligned 1D ZnO NRs [184].

Stabilization of polar surfaces can be achieved through reconstruction, faceting, surface non-stoichiometry and adsorption of external species. The first adsorbates are hydroxyl groups, arising from the decomposition of Zn salt. The growth is favored thanks to the “free space” along the [0001] direction, and the tetrahedral coordination of $[Zn(OH)_4]^{2-}$ furtherly facilitates the attachment.

Thin crystals prefer [0001] orientation because of the strong dependence of the [0001] superficial energy on thickness.

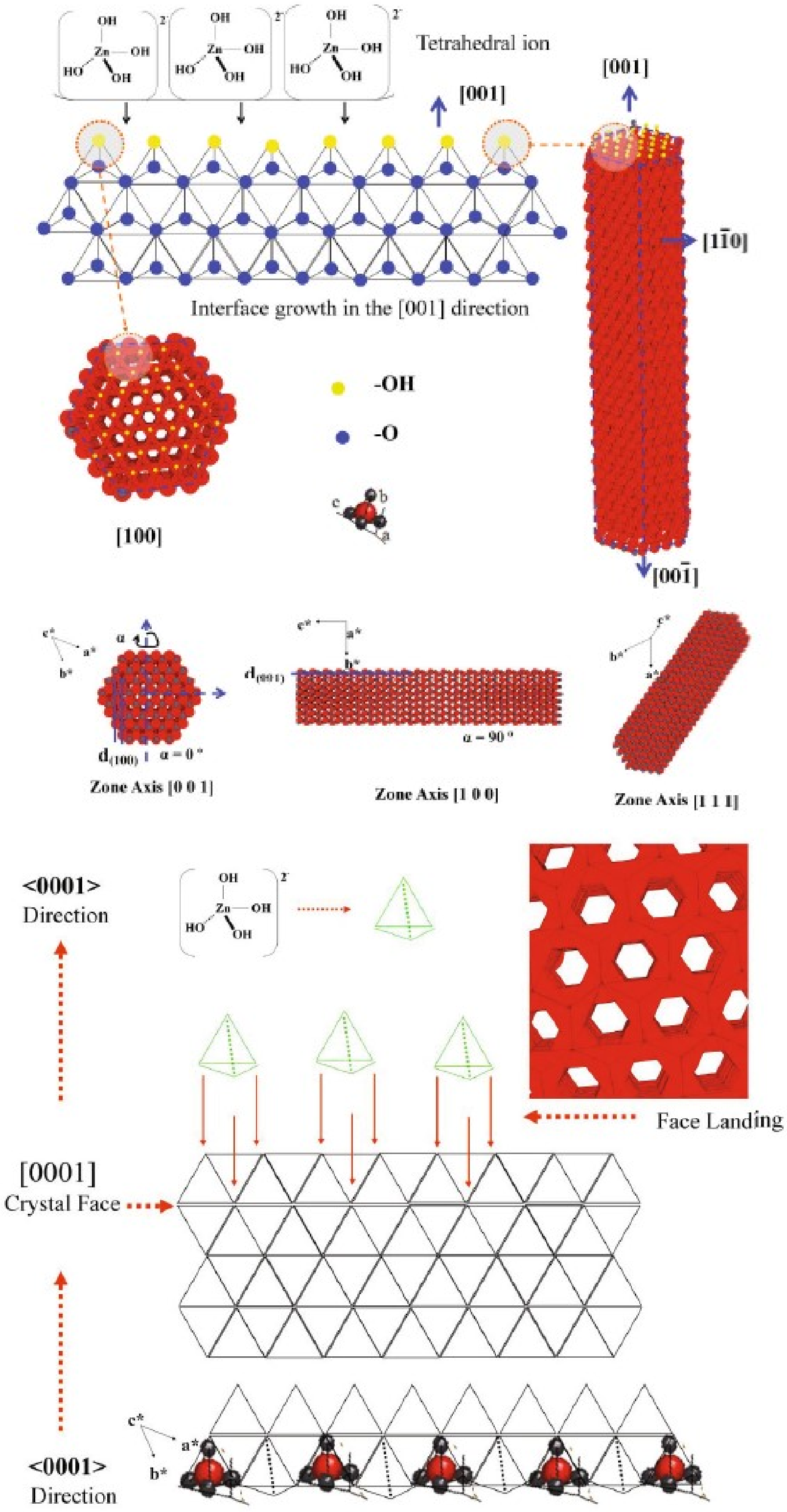

Fig. 30: Role of the tetrahedral coordination of $[Zn(OH)_4]^{2-}$ in the growth of aligned 1D ZnO NRs [184].

4 Piezoelectric effect

4.1 Discovery and equations

Non-centrosymmetry of some crystalline systems gives rise to a series of interesting physical phenomena, such as piezoelectricity, pyroelectricity and ferroelectricity.

Ferroelectricity is the property of a material, possessing permanent electric dipole, of changing polarization direction under electric field. These materials are included into the category of pyroelectrics, meaning materials that can generate electric polarization when subjected to thermal gradient. Pyroelectric materials are part, in turn, of the class of piezoelectric materials.

The word “piezoelectricity” arises from the Greek words *πιέζω (piezō)* or *πιέζειν (piezein)*, which means to squeeze or press, and *ήλεκτρον (ēlektron)*, which means amber, known already in antiquity as source of electric charge.

Piezoelectric effect was discovered by the brothers Jacques and Pierre Curie in 1880. They found out that by applying pressure on a quartz crystal along certain axis, opposite crystal faces showed opposite electric polarization; by reversing the solicitation (traction), reverse polarization was observed. This is called **direct piezoelectric effect**.

One of the most interesting peculiarities of piezoelectric effect is that it can act “in opposite ways”: indeed it is possible to produce electric polarization by deforming the crystal, but the contrary effect is obtainable as well, that is the deformation of the crystal caused by the application of electric polarization. This phenomenon was observed, for the first time, by Gabriel Lippmann in 1881 and it is called **inverse (or converse) piezoelectric effect** [196].

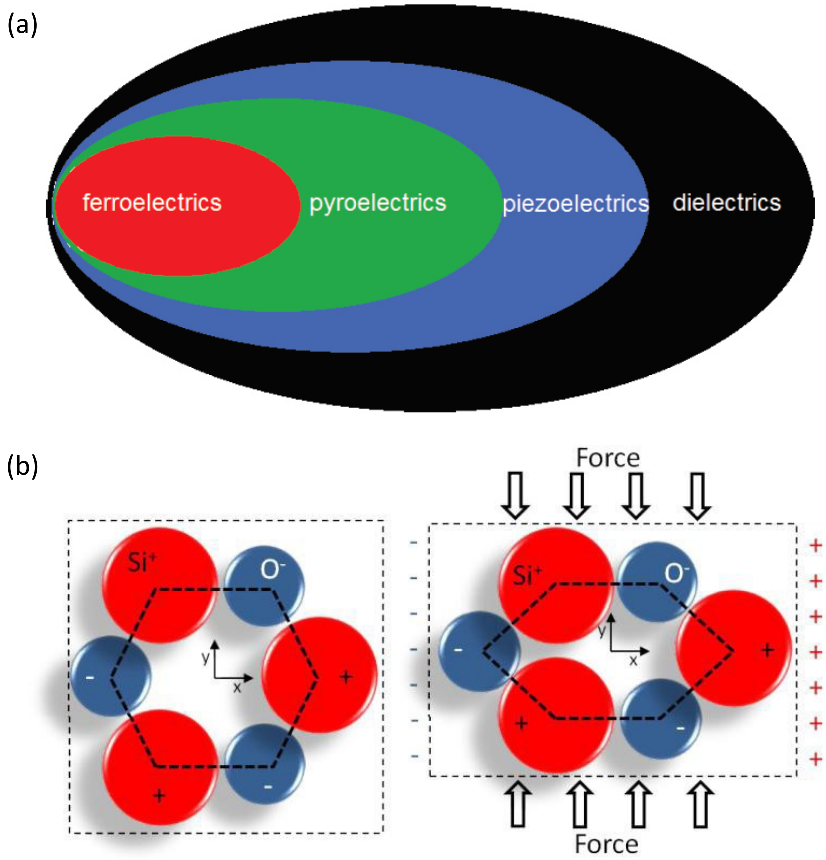

Fig. 31: (a) Classes of dielectric materials. They are distinguished by the non-polar (dielectric), induced polarization (piezoelectric), spontaneous irreversible polarization (pyroelectric) and spontaneous reversible polarization (ferroelectric) characters [197]. (b) Representation of the direct piezoelectric effect in a silica crystal.

The application of an electric field on an insulating material can polarize it causing separation of positive charges from the negatives. A macroscopic mark of this separation is surface charge, described by the electric polarization vector P_i $(i = 1, 2, 3)$.
Electric field and polarization are linked by the equation

$$P_i = \chi_{ij} E_j$$

where χ_{ij} represents the components of the electric susceptibility tensor. The total surface charge density, inducted by the application of electric field, is given by the electric displacement field D_i, which includes the contribution of charges originated by the polarization of the material.
Given that

$$D_i = \epsilon_0 E_i + P_i = \epsilon_0 E_i + \chi_{ij} E_j$$

and introducing the Kronecker function δ_{ij}

$$D_i = \epsilon_0 \delta_{ij} E_j + \chi_{ij} E_j = \left(\epsilon_0 \delta_{ij} + \chi_{ij}\right) E_j = \epsilon_{ij} E_j$$

where ϵ_0 and ϵ_{ij} are the vacuum and material dielectric permittivity.
For most of the ferroelectric materials the following conditions can be accepted:

$$\epsilon_0 \delta_{ij} \ll \chi_{ij}$$

$$\epsilon_{ij} \approx \chi_{ij}$$

Rather than electric permittivity ϵ_{ij}, relative electric permittivity

$$\kappa_{ij} = \frac{\epsilon_{ij}}{\epsilon_0}$$

often called dielectric constant of the material, is generally used. Typical values of κ_{ij} for piezoelectric materials range from 10 to 10^4.
The relation existing between the applied stress Π_m and resulting deformation x_{mn} is given, in linear approximation, by the Hook's law:

$$\Pi_m = C_{mn} x_n$$

where C_{mn} is the elastic stiffness tensor and $m, n = 1, 2, \dots, 6$ following the Voigt notation (same-index pairs $ii = 11, 22, 33$ are $1, 2$ and 3 respectively, while pairs $ij = ji = \ 11, 22, 33$ are $4, 5$ and 6 respectively).
For the inverse relation

$$x_m = S_{mn} \Pi_n$$

the elastic compliance tensor S_{mn} is present.
Piezoelectric materials represent a low-symmetry class of materials, which can be polarized, as well as by an electric field, also by a mechanical stress.

The linear relation between applied stress and resulting charge density describes the so called direct piezoelectric effect:

$$D_i = d_{im}\Pi_m$$

where d_{im} represents the piezoelectric coefficents.
The piezoelectric effect presents also an inverse behavior, described by the following equation:

$$x_m = d_{km}E_k = d_{mk}^{T}E_k$$

where T indicates the transpose of the matrix.
Coefficients d are the same for both direct and inverse piezoelectric effect

$$d_{dir} = d_{inv}$$

and the sign of D_i and x_m depends, as well as on the piezoelectric coefficients, also on both the stress and the electric field direction.
The coefficients measured along and perpendicularly with respect to direction of the force are generally indicated as longitudinal and transversal piezoelectric coefficients, respectively.
Symmetry impose conditions limiting the number of independent and non-zero coefficients.
Given the dual dependence of the piezoelectric effect by electric field and mechanical stress, it is useful to introduce a set of equations, which couple the electric and elastic parameters involved in the phenomenon. The equations seen previously can be written in complete form, under isothermal conditions, as following:

$$\begin{cases} x_m = S_{mn}^{T,E}\Pi_n + d_{im}^{T,\Pi}E_i \\ D_i = d_{im}^{T,E}\Pi_m + \epsilon_{ij}^{T,\Pi}E_j \end{cases}$$

where superscripts indicate variables which are maintained constant. These are known as the **fundamental equations of piezoelectricity** [198].

4.2 Piezoelectricity in wurtzite structure

ZnO presents some of the highest piezoelectric constants among tetrahedrally coordinated crystals. Together with the ease of synthesis and functionalization, low toxicity and low cost, as already explained in the first chapters, this is the reason why research is pushing its efforts toward this material for the development of piezoelectricity-based technologies.
Owing to its symmetry, independent rigidity coefficients for wurtzitic structure come down to just five, and the general Hook's law becomes

$$\begin{pmatrix} \Pi_{xx} \\ \Pi_{yy} \\ \Pi_{zz} \\ \Pi_{yz} \\ \Pi_{zx} \\ \Pi_{xy} \end{pmatrix} = \begin{pmatrix} C_{11} & C_{12} & C_{13} & 0 & 0 & 0 \\ C_{21} & C_{12} & C_{13} & 0 & 0 & 0 \\ C_{13} & C_{13} & C_{33} & 0 & 0 & 0 \\ 0 & 0 & 0 & C_{44} & 0 & 0 \\ 0 & 0 & 0 & 0 & C_{44} & 0 \\ 0 & 0 & 0 & 0 & 0 & C_{66} \end{pmatrix} \begin{pmatrix} x_{xx} \\ x_{yy} \\ x_{zz} \\ x_{yz} \\ x_{zx} \\ x_{xy} \end{pmatrix}$$

where

$$C_{66} = \frac{C_{11} - C_{12}}{2}$$

This is the direct form of the general Hook's law for a wurtzitic structure, whereas the inverse form is the following:

$$\begin{pmatrix} x_{xx} \\ x_{yy} \\ x_{zz} \\ x_{yz} \\ x_{zx} \\ x_{xy} \end{pmatrix} = \begin{pmatrix} S_{11} & S_{12} & S_{13} & 0 & 0 & 0 \\ S_{21} & S_{12} & S_{13} & 0 & 0 & 0 \\ S_{13} & S_{13} & S_{33} & 0 & 0 & 0 \\ 0 & 0 & 0 & S_{44} & 0 & 0 \\ 0 & 0 & 0 & 0 & S_{44} & 0 \\ 0 & 0 & 0 & 0 & 0 & S_{66} \end{pmatrix} \begin{pmatrix} \Pi_{xx} \\ \Pi_{yy} \\ \Pi_{zz} \\ \Pi_{yz} \\ \Pi_{zx} \\ \Pi_{xy} \end{pmatrix}$$

where

$$S_{66} = 2(S_{11} - S_{12})$$

The elastic constants C_{11} and C_{33} correspond to the longitudinal modes along [1000] and [0001] directions respectively, while C_{44} and C_{66} can be calculated from the sound velocity of transverse modes propagating along the [0001] and [1000] directions respectively. The remaining constant C_{13} is present in combination with four other moduli in the velocity of modes propagating in less symmetrical directions, such as [0011].

Thanks once again to symmetry, with regard to the piezoelectric coefficients tensors, polarization can be written as

$$\begin{pmatrix} P_{xx} \\ P_{yy} \\ P_{zz} \end{pmatrix} = \begin{pmatrix} 0 & 0 & 0 & 0 & e_{15} & 0 \\ 0 & 0 & 0 & e_{15} & 0 & 0 \\ e_{31} & e_{31} & e_{33} & 0 & 0 & 0 \end{pmatrix} \begin{pmatrix} x_{xx} \\ x_{yy} \\ x_{zz} \\ x_{xy} \\ x_{yz} \\ x_{zx} \end{pmatrix} = \begin{pmatrix} 0 & 0 & 0 & 0 & d_{15} & 0 \\ 0 & 0 & 0 & d_{15} & 0 & 0 \\ d_{31} & d_{31} & d_{33} & 0 & 0 & 0 \end{pmatrix} \begin{pmatrix} \Pi_{xx} \\ \Pi_{yy} \\ \Pi_{zz} \\ \Pi_{xy} \\ \Pi_{yz} \\ \Pi_{zx} \end{pmatrix}$$

where independent strain piezoelectric coefficients e_{ij} (or the stress piezoelectric coefficients d_{ij}, equivalently) are reduced to three values. e_{31} and e_{33} represent the polarization induced along c axis by a strain acting on the perpendicular plane and along the c axis itself, respectively. e_{15}, instead, describes the polarization induced by a shear strain, which is usually neglected for simplicity. The simplified relation

$$P_z^{piezo} = e_{33}x_z + e_{31}x_{\perp}$$

can be now written, where x_z and $x_{\perp}$ are the components of strain along the c axis and on the plane perpendicular to it.

The sign of the piezoelectric tensor is generally fixed assuming that the positive direction along c axis goes from the cation to the anion [37].

5 Experimental setup

5.1 Scanning electron microscope (SEM)

The SEM used in this work for imaging the samples is a dual beam Zeiss Auriga Compact system equipped with a GEMINI Field-Effect column [199].
The SEM analysis is important in order to ascertain the correct functionalization of the carbon fibers; moreover, it allows to study the resin layer in the encapsulation stage.
Two kinds of detectors are used here:

- Everhart-Thornley Detector (ETD), for secondary electrons, allows better 3D view and higher depth of field, so it is more suitable for high-distance imaging.
- In-lens detector, placed inside the microscope column, captures secondary electrons as well. Due to its location, lateral illumination is limited and contrast is more influenced by backscattered electrons, hence also compositional information are carried.
  It exhibits higher resolution and it helps in the presence of high insulating materials, such as ER used for composite preparation in this work.

Usual values of electron beam voltage range from 15 to 20 kV to achieve high resolution and contrast. When insulating resin is present, nevertheless, the electron beam voltage must be reduced to $3 \div 5\ kV$ to prevent blinding effects caused by static charges. A trick to meliorate visualization of insulating materials is to connect the sample to its holder by means of a piece of conductive carbon tape, and inspect the area of the sample nearby the ribbon.

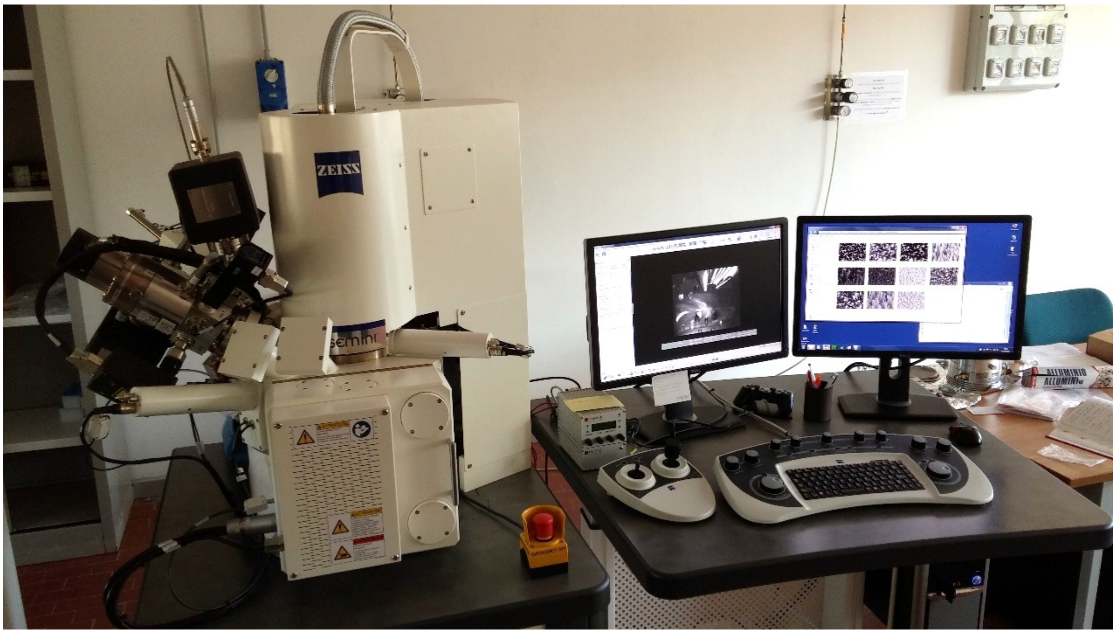

Fig. 32: The dual beam Zeiss Auriga Compact system equipped with a GEMINI Field-Effect column used in this study.

5.2 Ferroelectric tester

The characterization of the direct piezoelectric effect is carried out by means of the ferroelectric tester Thin-Film Analyzer 2000E by aixACCT GmbH.

High concentration of free carriers causes non-negligible conductivity in piezoelectrics, and as regards the measurement of the piezoelectric properties, the request of insulating character becomes an important constraint.

If an electric bias is applied on a material presenting polar structure but simultaneous high conductivity, the current flow arising from the free carriers overwhelms the polar current and drops it to zero, so that no evidences of polarity can be recorded. In the extreme conditions of a quasi-metallic system, piezoelectric characterizations are even impossible operations.

Fortunately, it is possible to overcome this limitation by acting on the impedance of the studied material. The idea consists in the separation between the dielectric and ohmic response. In terms of current intensity, the two situations show completely different voltage dependent signals:

$$I = \frac{1}{R} V$$

$$I = \frac{dQ}{dt} = C\frac{dV}{dt}$$

If both equations are integrated as function of time, one obtains

$$Q = \frac{1}{2R} V^2$$

$$Q = CV$$

Consequently, during a charge vs. voltage (Q-V) measurement, an ohmic or low-gap semiconducting material will display a parabolic trend (fig. 33/a), while a linear behavior will be observed for a pure dielectric material (fig. 33/b). Hence, for a sample characterized by a superposition of dielectric and ohmic characters, a convolution of these two trends should be expected; this is the case also of a capacitor showing robust capacitive losses. In this scenario, one regime can be distinguished from the other by means of dynamic voltage pulse of variable frequency. In the low frequency regime the resistive nature will be favored, whereas in the high frequency regime the dielectric part will dominate. In other words by means of a proper (fast) AC voltage signal it is possible to isolate and detect the dielectric response of the material, which includes also information about the possible polarization of the system, cutting out the ohmic contribution.

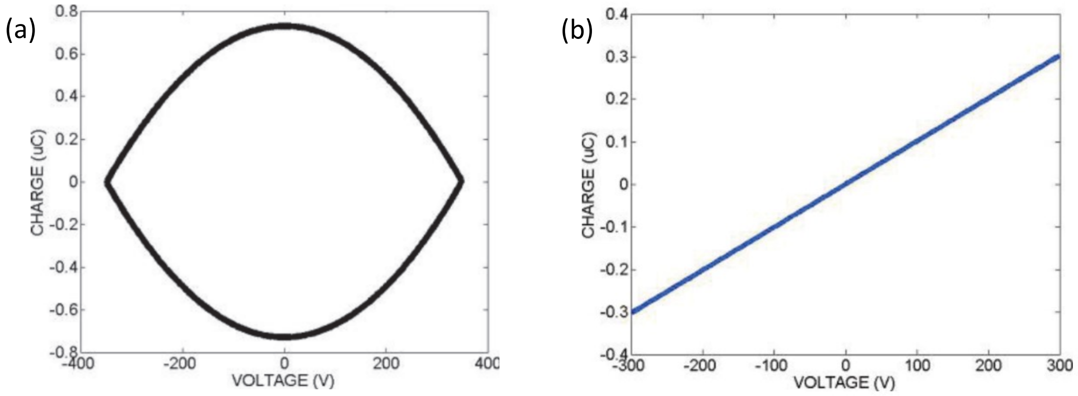

Fig. 33: Typical charge vs. voltage dynamic measurement of an ohmic material (a) and a dielectric material (b).

The instrument exploited in order to carry out these studies is the Thin-Film Analyzer 2000E (TFA) equipped with the Ferroelectric Module, produced by the German company aixACCT Systems GmbH. This versatile hardware/software package is conceived for the characterization of piezoelectric, pyroelectric and ferroelectric thin-film devices, but simple setup modifications allow to study bulk materials as well.

In principle a variety of measurement systems are designed with the TFA system as core component to fulfill different measurement tasks (*e.g.* thin films and MEMS devices, bulk ceramics, and multilayer actuators). For this purpose, the TFA can control external hardware components like a temperature controller or a high-voltage amplifier, and reads additional data from displacement, temperature or force sensors.

To summarize the experimental methods of this tester, one has to consider that electrical and electromechanical characterization of dielectric materials are the decisive factors for the investigation of their suitability for piezoelectric, pyroelectric and ferroelectrics sensors and actuators.

Substantial for electrical characterization of a sample is the measurement of its current or charge response produced by the application of electrical excitation voltage. In piezoelectrics, the electromechanical response can be measured either by applying an electrical excitation signal and measuring the sample mechanical displacement, or by applying a mechanical strain and recording the resulting charge displacement. The first method is commonly used as it allows the simultaneous electrical and electromechanical characterization.

Let us consider the magnitude of the current I, given by the charge Q, flowing during a polarization reversal in a ferroelectric capacitor; it can be calculated as

$$Q = D \cdot A \approx P \cdot A$$

$$I = \frac{dQ}{dt} = A \frac{dP}{dV} \frac{dV}{dt}$$

where A is the area of the capacitor, P the polarization of the material, V the applied voltage and ${}^{dV}/_{dt}$ the slew rate of the signal form that is applied.

Due to the switching process around the coercive voltage V_C, ${}^{dP}/_{dV}$ is not constant and the peak switching current will increase in one or two orders of magnitude. Besides the current magnitude, it is necessary to know the bandwidth of the current in order to decide how the current can be recorded. The frequency spectrum of the current will define the bandwidth requirements for the recording amplifier. Furthermore, the noise and ground bouncing is an important aspect, which will finally result in the estimation of the signal-to-noise ratio (SNR). These parameters all together determine how well the electrical properties of a piezo or ferroelectric capacitor can be assessed. There are three established methods to record the charge and current response of the sample: the Sawyer Tower method, the Shunt method and the Virtual Ground method.

- **Sawyer Tower Method**

The Sawyer Tower method is based on a charge measurement method, which relies on a reference capacitor in series with the ferroelectric capacitor.

The voltage drop at the reference capacitor is proportional to the polarization charge, as defined by

$$V = \frac{Q}{C}$$

But if the voltage on the reference capacitor increases, the voltage at the sample decreases (back voltage effect). Therefore, the reference capacitor has to be much larger than the measured capacitor. For instance, if the reference capacitor is 100 times larger, the voltage drop is about 1%. This means the reference capacitor has to be adjusted to each sample.

The Sawyer Tower method can be used up to high speeds, which is primarily limited by cable reflections. The parasitic effects of cabling capacitances of the wiring between sample, reference capacitor and the recording amplifier are in parallel to the reference capacitor. For small capacitors, the capacitance of the ferroelectric material is blinded in the total measured capacitance. Furthermore, it is difficult to get precise reference capacitors, which typically show several percent tolerance and, in addition, the cable capacitance has to be added to this capacitance. Moreover, the input resistance of the voltage measurement device is in parallel to the reference capacitor. This leads to a discharge with a corresponding time constant, hence the Sawyer Tower method is less suitable for slow measurements.

- **Shunt method**

The Shunt measurement substitutes the reference capacitor of the Sawyer Tower circuit with a reference resistance (shunt resistor). This measurement method is a current based method, thus the switching current is measured as a voltage drop at the shunt resistor, since

$$V = IR$$

and integrated to get the polarization charge Q. Similar difficulties as in case of the Sawyer Tower setup appear. Though it is easier to get precision resistors, the resistance value of choice depends not only on the sample capacitance but also on the excitation frequency.

Thus, the voltage drop increases with increasing frequency and the time constant of ferroelectric capacitor and shunt resistor influences the result at higher speed. Additionally the cable, as well as the input capacitance for the voltage-measuring device, are in parallel to the reference resistor. Therefore, accurate measurements for large systems are possible but increasingly difficult in case of small areas, where the parasitic capacitances become non-negligible.

- **Virtual Ground method**

The two peculiar limits of the presented methods, *i.e.* the difficulty to measure small ferroelectric capacitors or anyhow there are capacitance losses, can be prevented by a Virtual Ground based circuital methodology.
The Virtual Ground method uses a current-to-voltage converter, which is constituted by current measurement device using an operational amplifier with feedback resistor (fig. 34). The output of the current-to-voltage converter is connected to the inverting input of the operational amplifier via the feedback resistance; the non-inverting input is connected to ground. The voltage difference between both inputs is ideally zero, but just a few microvolts in reality. Therefore, the inverting input is virtually at ground level. This is helpful for the measurement (especially of small capacitors) as the cable capacitance is physically in place but electrically ineffective, because both electrodes of the capacitor are kept on the same potential. Moreover, the sample always undergoes the full excitation voltage, since there is no back voltage.
For high-speed measurements, or voltage pulses, the inductance of the setup and the impedance mismatch, caused by sample and sample holder, will lead to reflection in the cable and, therefore, to a measurable change of signals related to the setup. Moreover, stability, bandwidth, and phase shift of the operational amplifier must be taken into account.
However, as a whole, the Virtual Ground method enables the highest precision for piezoelectric measurements.

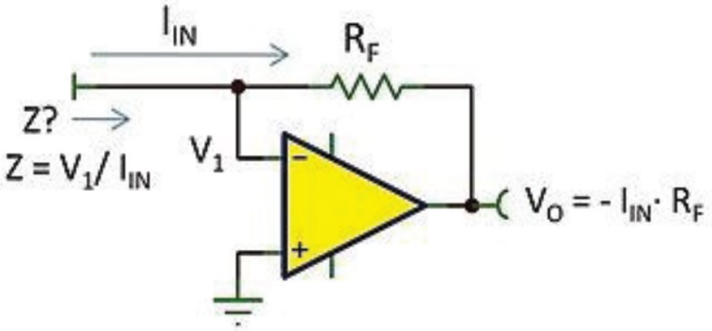

Fig. 34: Equivalent circuit of the Virtual Ground Feedback system.

For all these reasons, Virtual Ground Feedback is used as integral part of aixACCT Measurement System.

In this configuration, this system allow to perform several dynamic and static charge, current and capacitance measurements as presented below:

- Dynamic Hysteresis Measurement (DHM)
- Pulsed Measurement (PUND)
- Static Hysteresis Measurement (SHM)
- Leakage Current Measurement (LM)
- Capacitance Measurement (CM)

The system can also work at two different voltage ranges: specifically, from $10\,mV$ to $20\,V$ for low-voltage and from $5\,V$ to $2\,kV$ for high-voltage. These two configurations give also the possibility to study a wide set of samples with different thickness.

The most peculiar and uncommon type of measurement which is possible to carry out by means of this technique is the DHM. This charge measurement for recording hysteresis loops exploits an excitation bias, like a triangular (or sinusoidal) signal. The range of signal frequencies, guaranteed by the FE module, goes from $10\,mHz$ to $5\,kHz$. There is a pre-polarization pulse and three bipolar excitation signals generated if the default settings are used (fig. 35).

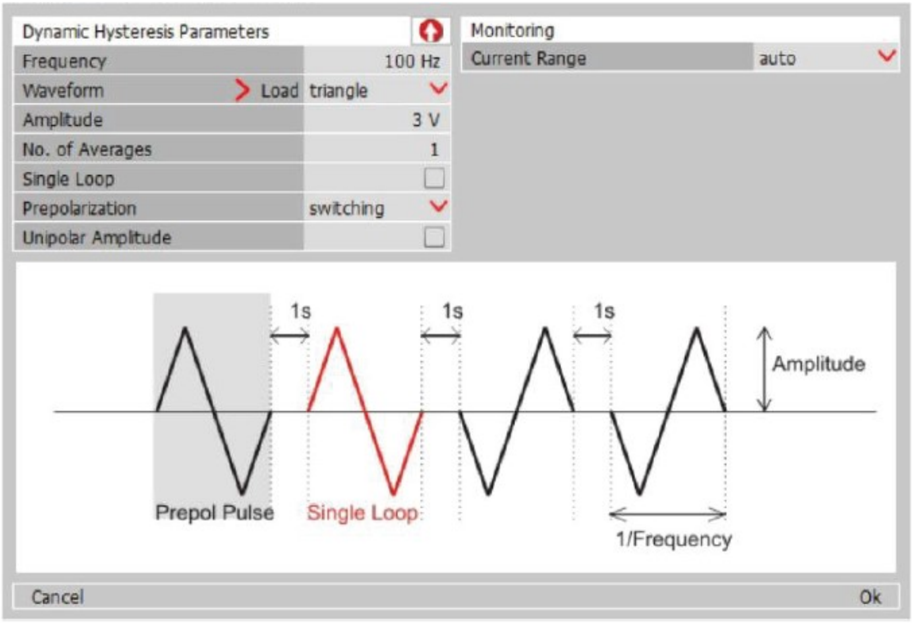

Dynamic Hysteresis Parameters
Frequency 100 Hz
Waveform Load triangle
Amplitude 3 V
No. of Averages 1
Single Loop ☐
Prepolarization switching
Unipolar Amplitude ☐

Monitoring
Current Range auto

Fig. 35: The typical excitation signal of a DHM preformed with the TFA system.

Each signal is followed by a relaxation time pause of 1 second. The pre-polarization pulse and the second pulse of the excitation signal establish defined polarization states. The pre-polarization pulse has a negative state of relaxed remnant polarization; the second pulse ends in the positive state of relaxed remnant polarization. The corresponding hysteresis loop is an elaboration of the recorded charge signal for each step [200] [201].

The characterization of the direct piezoelectric effect is carried out, thanks to Prof. Massimo Solzi, in collaboration with Dr. Davide Delmonte (IMEM-CNR) at Dipartimento di Fisica e Scienze della Terra “Macedonio Melloni” of the Università di Parma.

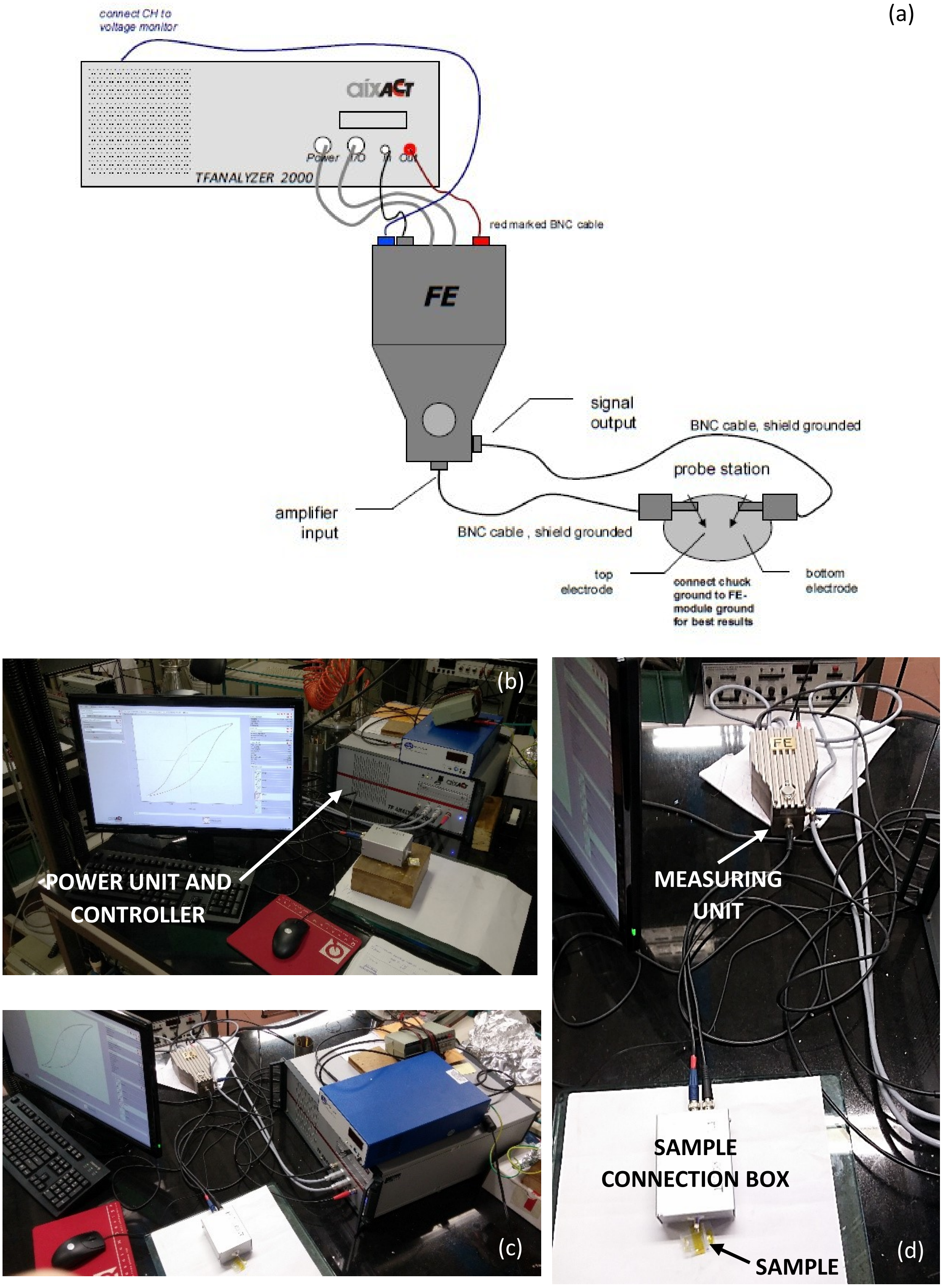

Fig. 36: (a) Structure of the aixACCT Thin-Film Analyzer 2000E. (b-d) Pictures of the instrument at Dipartimento di Fisica e Scienze della Terra “Macedonio Melloni” in Parma.

5.3 Piezoresponse force microscope (PFM)

PFM is used in order to measure the inverse piezoelectric effect. The general setup is analogous to the Atomic Force Microscope (AFM), which represents an ideal platform for the local study of piezoelectricity, thanks to the exceptional vertical resolution at picometer scale.

PFM is a contact-mode AFM where an electrically biased conductive tip serves as a probe. The tip is part of a cantilever, whose deformation is measured through the shift of a laser beam reflecting on its surface (fig. 37).

High localization of the electric field is achieved at the junction between sample surface and metalized tip. Nevertheless, the image formation mechanism is complementary to the AFM one, which is force-based.

In PFM voltage is applied to the conductive tip:

$$V_{tip} = V_{DC} + V_{AC}\cos(\omega t)$$

where V_{DC} is the DC bias (switching bias), V_{AC} the AC bias (probing bias) and ω the AC bias driving frequency. The piezoelectric crystal consequently expands/contracts owing to the inverse piezoelectric effect and the related tip deformation is measured by means of a lock-in amplifier as

$$A = A_0 + A_{1\omega}\cos(\omega t + \varphi)$$

where A_0 is the static surface displacement and φ is the phase shift between V_{AC} and the voltage-induced deformation

$$A_{1\omega} = d_{33}^{eff,V_{AC}} + \left(\frac{\partial C}{\partial z}\right)(V_{DC} - V_S)V_{AC}$$

The term $d_{33}^{eff,V_{AC}}$ is the true piezoresponse along the z direction (c axis), the second term is the local deformation caused by both local and non-local Maxwell stress [202], V_S is the surface potential and C the total capacitance of the cantilever/sample system.

The PFM amplitude provides information on the magnitude of the local electromechanical coupling, while the PFM phase image gives local polarization orientation.

The resolution is limited by the tip-sample contact area (nominally determined by the radius of the tip apex), but some mechanisms are able to broaden it, such as electrostatic interactions and the formation of a liquid neck in the tip-surface junction.

The cantilever can exhibit three displacement modes:

- **vertical deflection**, as a result of the out-of-plane force due to the d_{33}^{eff} coefficient;
- **torsion**, related to the shear piezoelectric coefficient d_{15}^{eff};
- **buckling**, from the interaction with the surface when an in-plane force acts along the cantilever axis.

The first type of deformations are referred to as out-of-plane (or vertical PFM, or VPFM) measurements, with the others denoted as in-plane (or lateral PFM, or LPFM) measurements.

If the polarization and applied electric field are parallel, the deformation is positive (expansion) and the piezoresponse is in phase with V_{AC}. On the contrary, if the applied electric field is antiparallel to the spontaneous polarization, this will cause piezoelectric to contract, with the consequent lowering of the cantilever; in this case the applied electric field and the piezoresponse signal are shifted in phase by 180° [203].

For this study, the piezoelectric coefficient d_{33} of ZnO NRs is characterized by means of the PFM Park Systems XE-100 with Pt-coated silicon tip (Multi 75E-G, Budget Sensors, 3 $^{N}/_{m}$ of force constant and 75 kHz of resonant frequency). AC voltage of 0 to 5 V with 17 kHz is applied from a lock-in amplifier (Stanford Research, SR830) to the ZnO nanorod and the subsequent axial deformation is measured.

The PFM characterization has been performed, thanks to Prof. Sang-Woo Kim, by Mr. Tae-Yun Kim at the Nano Electronic Science and Engineering Laboratory (NESEL) of the School of Advanced Materials Science & Engineering (AMSE), Sungkyunkwan University (SKKU), Suwon, South Korea.

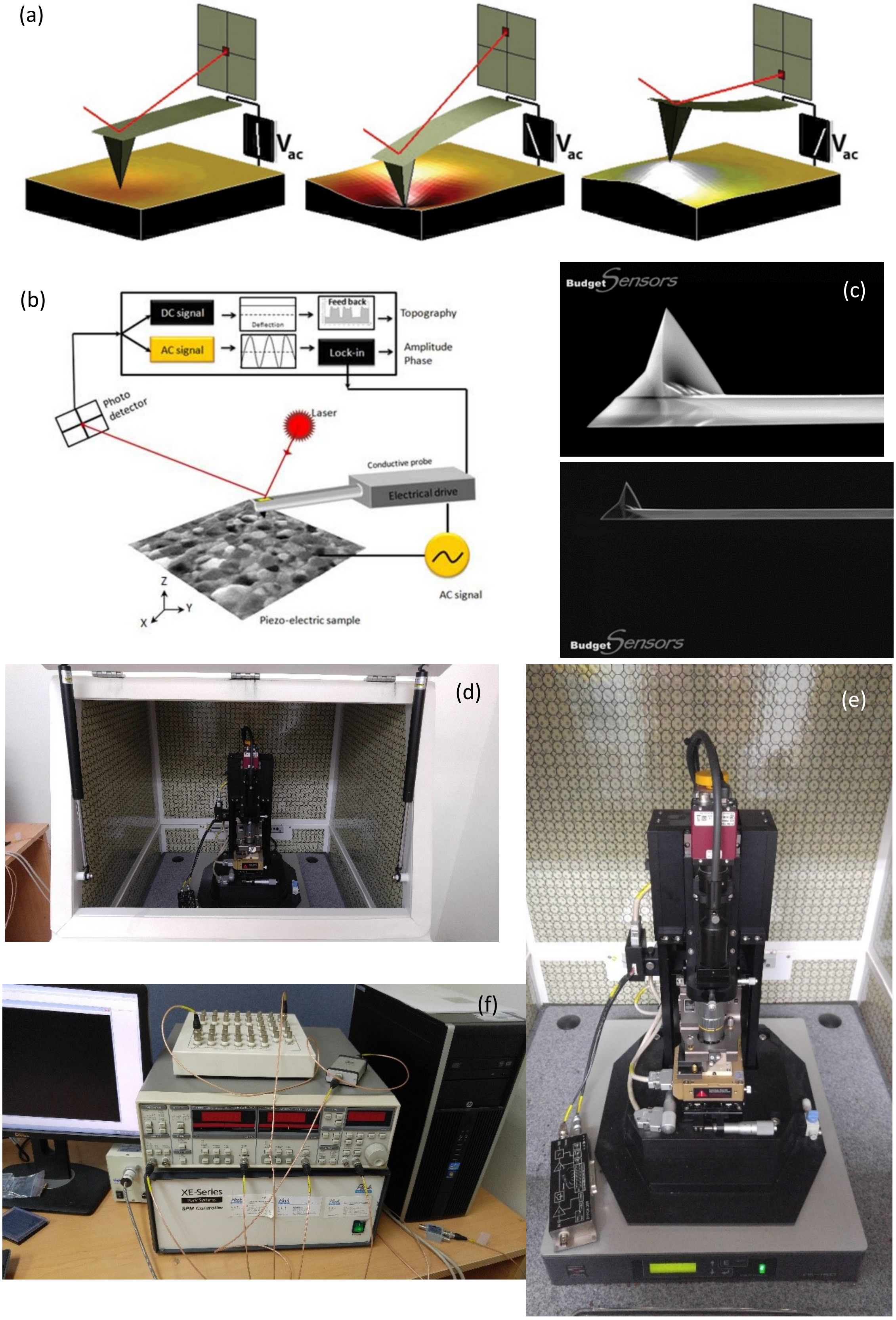

Fig. 37: (a, b) Working principle of the PFM [204] [205]. (c) SEM image of the Pt-coated tips used in the experiments [206]. (d, e) The PFM Park Systems XE-100 [207] inside an anti-seismic Faraday cage at NESEL, South Korea. (f) The PFM controller.

5.4 X-ray diffractor

XRD is a versatile, non-destructive analytical method for identification and quantitative determination of various crystalline phases of compound present in powder and solid samples. Diffraction occurs as waves interact with a regular structure whose periodic distance is about the same as the wavelength. The phenomenon is common in the natural world, and occurs across a broad range of scales. For example, light can be diffracted by a grating having scribed lines spaced the order of a few thousand angstroms, about the wavelength of light. It happens that X–rays have wavelengths the order of a few angstroms, the same as typical inter-atomic distances in crystalline solids. When certain geometric requirements are met, X–rays scattered from a crystalline solid can constructively interfere, producing a diffracted beam. In 1912, W. L. Bragg recognized a predictable relationship among several factors summed in the well-known Bragg equation:

$$n\lambda = 2d\cos\vartheta$$

where n is a positive integer, λ the wavelength, d the distance between two adjacent crystalline planes and ϑ the angle between a crystalline plane and the outgoing beam.

Bragg's law states the condition for a sharp diffraction peak from an infinite crystal with perfect 3D order. Typically, the diffraction peak has a finite width, which is associated with imperfections in some of the Bragg parameters. These imperfections can be associated with beam divergence, a somewhat polychromatic source, or defects in the crystals. The latter can be a basis for quantitative measurement of the deviation from the Bragg requirement for perfect crystal, which is infinite in all spatial directions.

Deviations from the latter requirement have been explained in terms of three features:

1) finite crystallite size (Scherrer equation [208])
2) distortions of the first kind, which are random motion of atoms in a crystalline lattice (Debye thermal broadening) or other local randomization of lattice sites which do not disturb the 3D repetition or crystalline motif;
3) distortions of the second kind, which involve destructive of long range order in the crystal, *i.e.* at long distances the lattice does not repeat perfectly.

These usually lead to preferential broadening of high order peaks. The Scherrer equation can be written as

$$D = \frac{\kappa\lambda}{\beta\cos\vartheta}$$

where D is the mean diameter, κ the shape factor and β the full-width at half maximum. Since small angular differences in angle are associated with large spatial distances (inverse space), broadening of a diffraction peak is expected to reflect some large-scale feature in the crystal. The simplest way to obtain the Scherrer equation is to take the derivative of Bragg's law holding the wavelength constant and allowing the diffraction angle and the Bragg spacing to vary. Take derivative in d and ϑ yields

$$2\Delta d\cos\vartheta\,\Delta\vartheta = \lambda$$

since $\Delta\vartheta$ can be positive or negative the absolute value must be taken and it reflects the half width of the peak (really half-width at half-height) so $2\Delta\vartheta$ is the peak full-width at half-height (β). The shape factor provides information about the “roundness” of the particle. For a spherical particle the shape factor is 1, for all other particles it is smaller than 1. The formula for this calculation is:

$$\kappa = 4\pi\frac{A}{p^2}$$

where A is area and p perimeter.
If a Gaussian function is used to describe the peak, a pre-factor of 0.9 occurs so the Scherrer equation is given as [209]:

$$\Delta D = \frac{0.9\lambda}{\beta\cos\vartheta}$$

XRD patterns are recorded by using a Thermo Scientific Thermo ARL X’tra diffractometer. The equipment has a Bragg-Brentano Θ-Θ configuration (fig. 38/a) with a maximum 2ϑ excursion ranging from $-8°$ and $180°$. X-Ray source is $Cu\ K\alpha$ ($\lambda = 1.542$ Å) and the accelerating voltage can be set in the range $20 \div 40\ kV$.

Diffracted rays are collected through a solid state $Si(Li)$ detector cooled by Peltier element.
XRD patterns are recorded by Dr. Francesco Mezzadri at Laboratorio di Strutturistica “M. Nardelli”, Università di Parma.

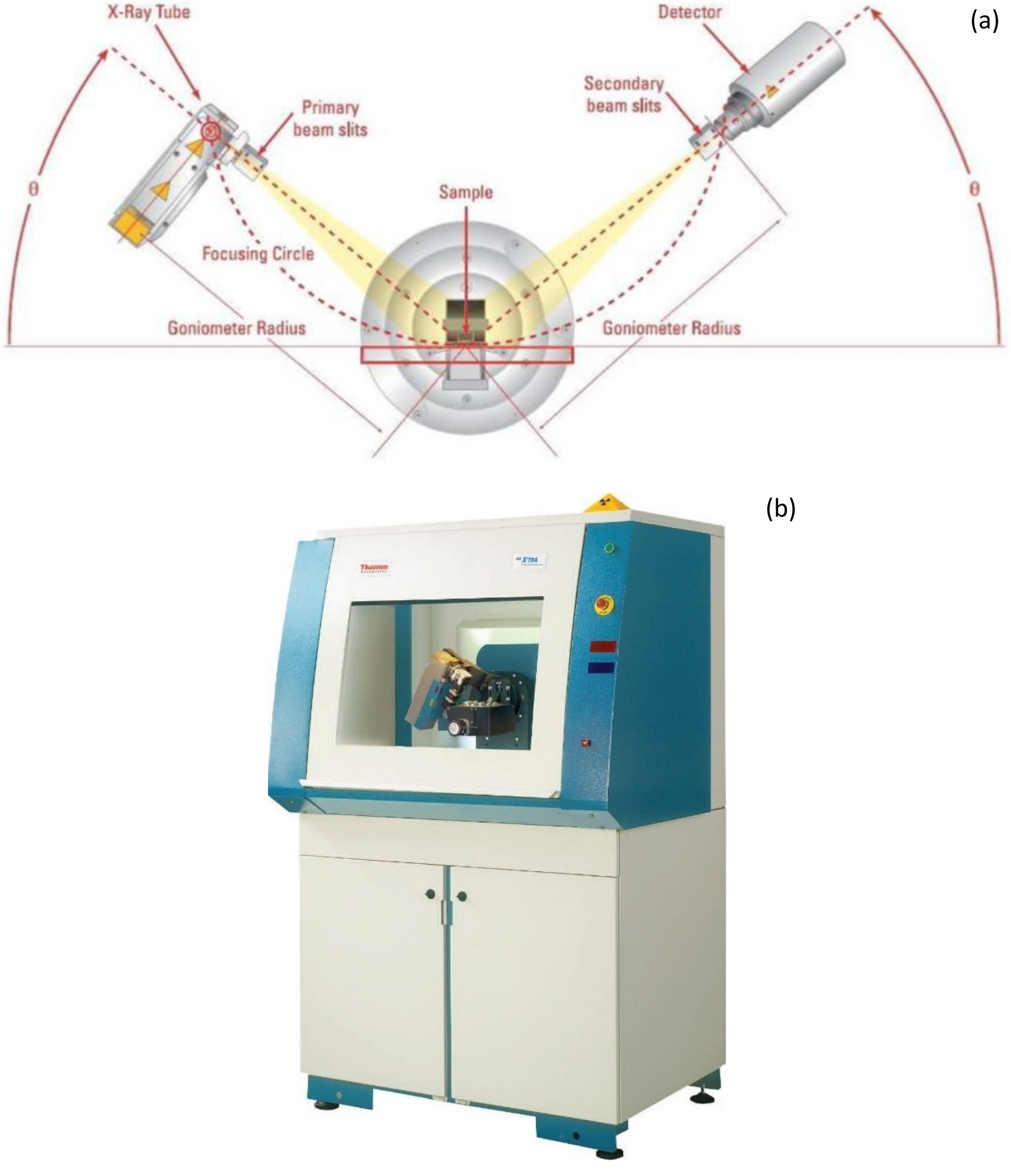

Fig. 38: (a) Bragg-Brentano Θ-Θ geometry in a XRD system. (b) Thermo ARL X’tra diffractometer.

5.5 Dynamometer for InterLaminar Shear Strength

InterLaminar Shear Strength (ILSS), is evaluated according to ASTM D2344 industrial standard (short-beam strength of polymer matrix composite materials and their laminates). The analysis is carried out by means of a Metrocom dynamometer with 50 kN full scale of the load cell.

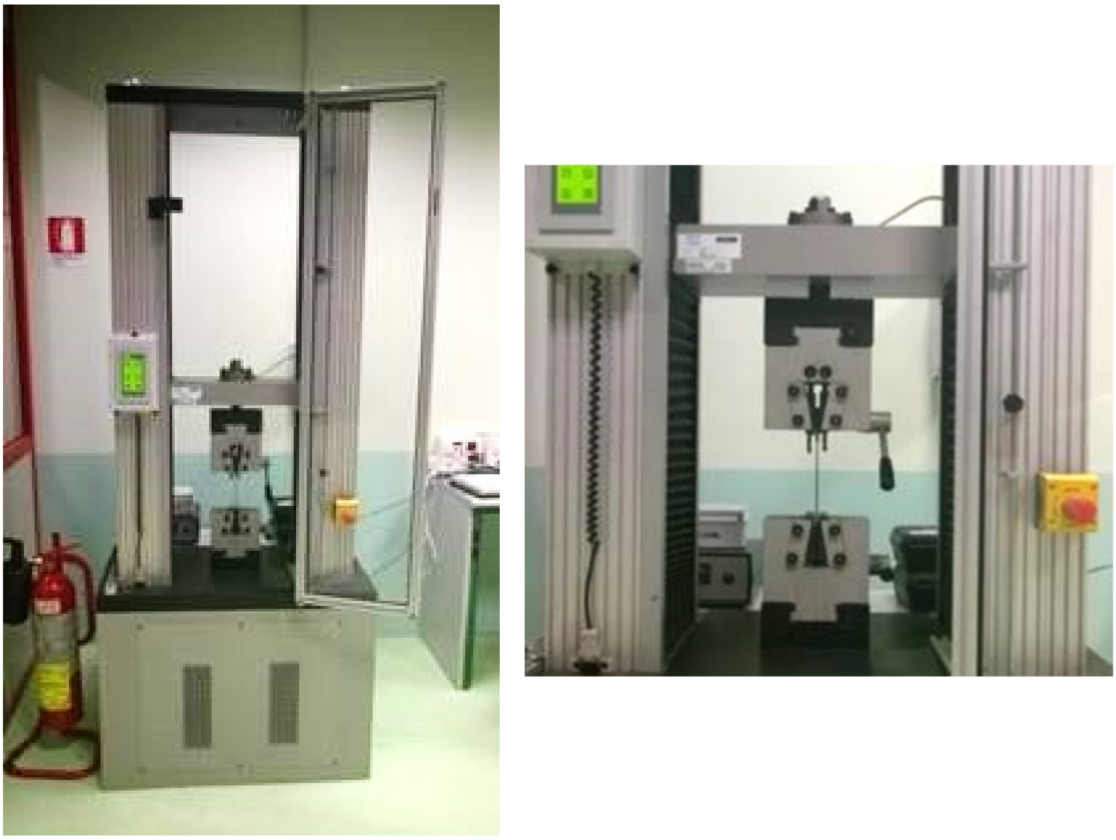

Fig. 39: The Metrocom dynamometer used for the mechanical analysis at Bercella s.r.l., Varano de' Melegari (Parma).

EXPERIMENTAL

6 Synthesis

The aim of this work is the realization of a deformation-sensing device based on the functionalization of carbon fibers with piezoelectric ZnO NRs.
The growth of ZnO NRs on carbon fibers needs to respect the following constraints in order to meet the industrial requirements:

- Low cost
- Low environmental impact
- Low temperature

ZnO is a low cost material, so the possibility of a low cost process depends on the use of low cost precursors, solvents and synthesis facilities.
Thanks to the alkaline CBD described in chapter 3 it is possible to exploit water as solvent, which is the best choice for environmental issues and low cost as well. Other than for a cost matter, carbon fibers undergo fast oxidative degradation in the presence of oxygen at high temperatures, which must be kept as low as possible. CBD works well at temperatures below the boiling point of water, so it is considered a low temperature technique.
The growth of ZnO NRs needs, however, the pre-deposition of a ZnO SL that will work as nucleation site.
The synthesis of ZnO NRs is fulfilled at IMEM-CNR and some of the samples were prepared in collaboration with Dr. Marco Villani (IMEM-CNR) and Ms. Sara Beretta (Università di Parma). SEM characterization was effectuated in collaboration with Dr. Davide Calestani at IMEM-CNR.

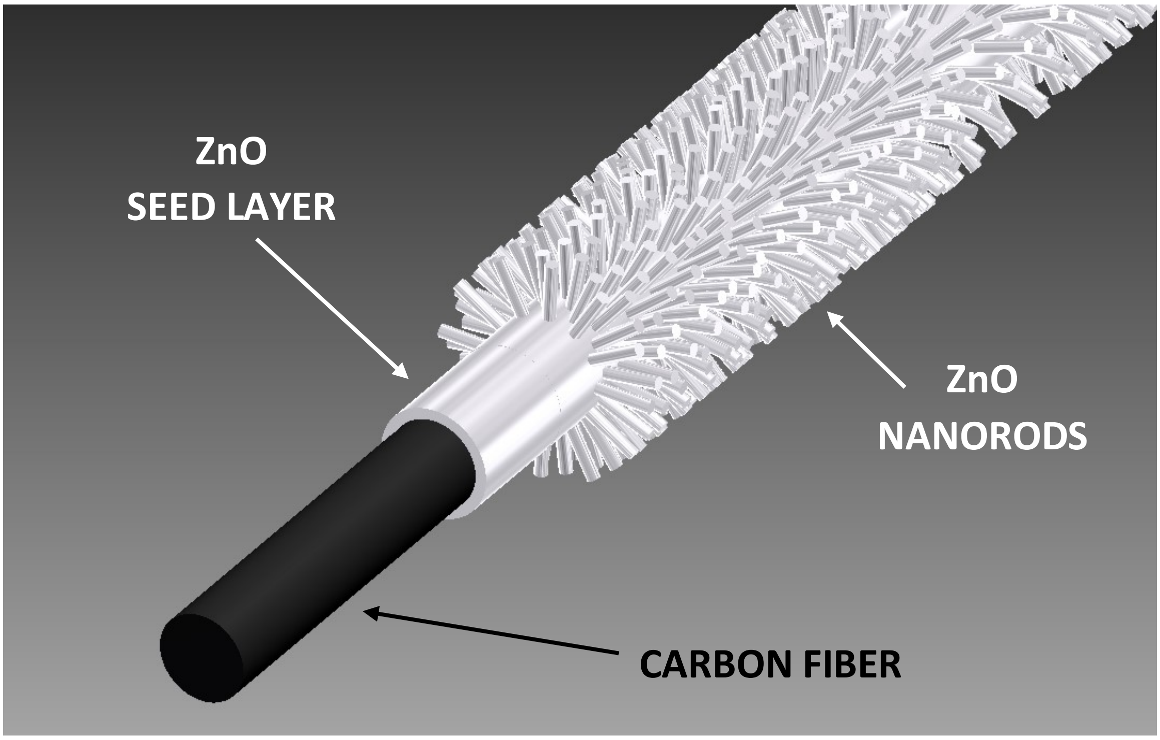

Fig. 40: The wanted structure is a ZfCF, but the first step is the deposition of a ZnO SL that will act as nucleation site.

6.1 Seed layer

The deposition of a SL on the surface of the carbon fibers is a crucial step for the subsequent growth of NRs. ZnO SL is seen by the precursors as a substrate where nucleation is facilitated. As explained in chapter 2, heterogeneous nucleation is energetically favored with respect to the homogeneous one: at certain supersaturation and temperature conditions, when precursors will be transported close to the SL by convective motion, they will find also advantageous crystalline coordination and geometry for starting the growth of the 1D nanostructure.
The SL can be prepared by two different methods:

1. CFs are immersed sequentially into the solution containing the Zn^{2+} ions and the one with alkaline environment (OH^{-} ions). Between the first and the second immersion, the sample is rinsed with bidistilled water in order to remove precursor excess. The rinsing step has to be made gently, in order to avoid removal of the deposited seed layer. Eventually, the substrate is put on hot plate to remove solvent.
   By varying the number of repetitions, it is possible to tune the thickness of the seed layer. A low number of cycles can lead to uncomplete coverage, while if the number or cycles is high, the film conformation can result irregular, therefore, the subsequent nanostructure growth would not be morphologically homogeneous. The optimal number of repetitions turned

out to be twenty.

The alkaline precursor can be DEA or ammonia, but the latter is preferable thanks to its lower toxicity and viscosity.

2. Deposition of ZnO nanoparticles. Tests reveal that two depositions are enough for a satisfactory growth of NRs. The substrate is placed first on a paper filter and eventually into the oven at 100 ℃ for 10 minutes in 210 $mbar$ vacuum, in order to dehydrate.

It is worth mentioning that different types of carbon fibers can lead to different SL deposition and NRs growth; indeed, the carbon fiber manufacturing processes involve use of primer, surface and other treatments (usually secret) that can change the surface properties of the fibers.

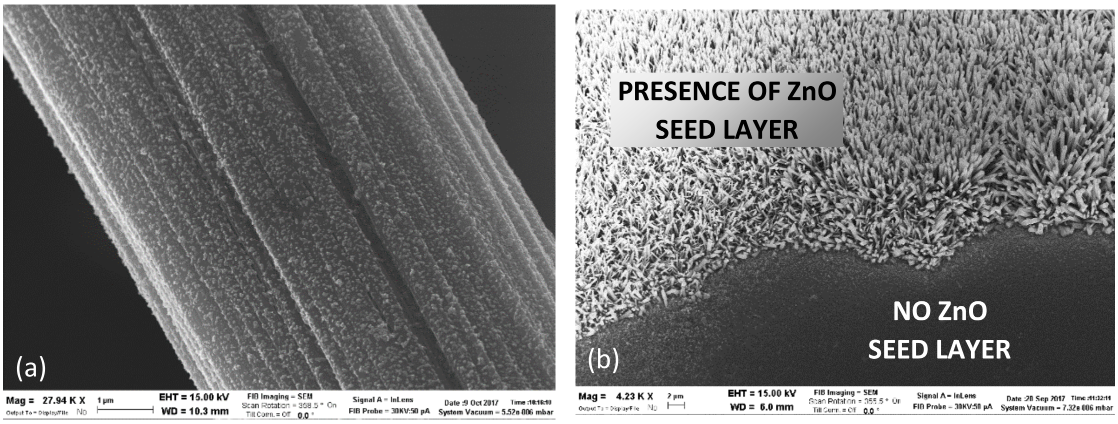

Fig. 41: (a) SEM image of the ZnO SL on a carbon fiber. (b) Functionalization comparison between areas where ZnO SL is present and absent.

6.2 Nanorods

Once SL is deposited, the growth of ZnO NRs is favored by the presence of the ZnO grains, which helps precursor involvement for geometrical and energetic reasons.

Different growth parameters can be changed in order to tune the aspect ratio and surface density of nanostructures, but these are highly affected especially by precursors concentration. While the dependence of temperature, time, SILAR parameters and nature of precursors has been studied in my Master's degree thesis [210], here the influence of precursor concentration is investigated in particular.

The morphological study is performed on flat glasses where ZnO SL is deposited, rather than carbon fibers; this can be done without significant errors inasmuch the surface that precursors encounter is a homogeneous layer of ZnO nanoparticles, so the nature of the underlying surface is irrelevant. Since density and,

consequently, alignment of the NRs depend (as well as on precursors concentration) on the availability of free space, a minimal variation can be observed for the growth on carbon fibers, owing to their curvature with respect to a flat surface. However, aspect ratio is not affected by these geometrical characteristics. A systematic study is fulfilled by changing the concentration of Zn nitrate hexahydrate ($Zn(NO_3)_2 \cdot 6H_2O$, Sigma-Aldrich, purity $\geq$ 99.0%) and HMTA (Sigma-Aldrich, purity $\geq$ 99.5%). The growth solution is equimolar in most cases, while some deviation from equimolarity is attempted in order to verify the role of the single precursors.
The steps for the NRs growth are the following:

1. Both precursors are put in a 500 ml beaker and 500 ml of bidistilled water are added.
2. The solution is kept under magnetic stirring until precursors are dissolved.
3. The substrate (microscope glass for aspect ratio investigation, carbon fiber for devices), where ZnO SL is previously deposited, is immersed into the solution.
4. The beaker is covered with aluminum foil to prevent evaporation of the solvent (water) that could bring to an alteration of the solution concentration.
5. Growth is carried out at 95 ℃ for 4 hours.
6. The functionalized substrate is removed from the container and washed vigorously with propan-2-ol and bidistilled water.
7. The sample is finally put in oven for exsiccation at 100 ℃ in 210 $mbar$ vacuum for 10 minutes.

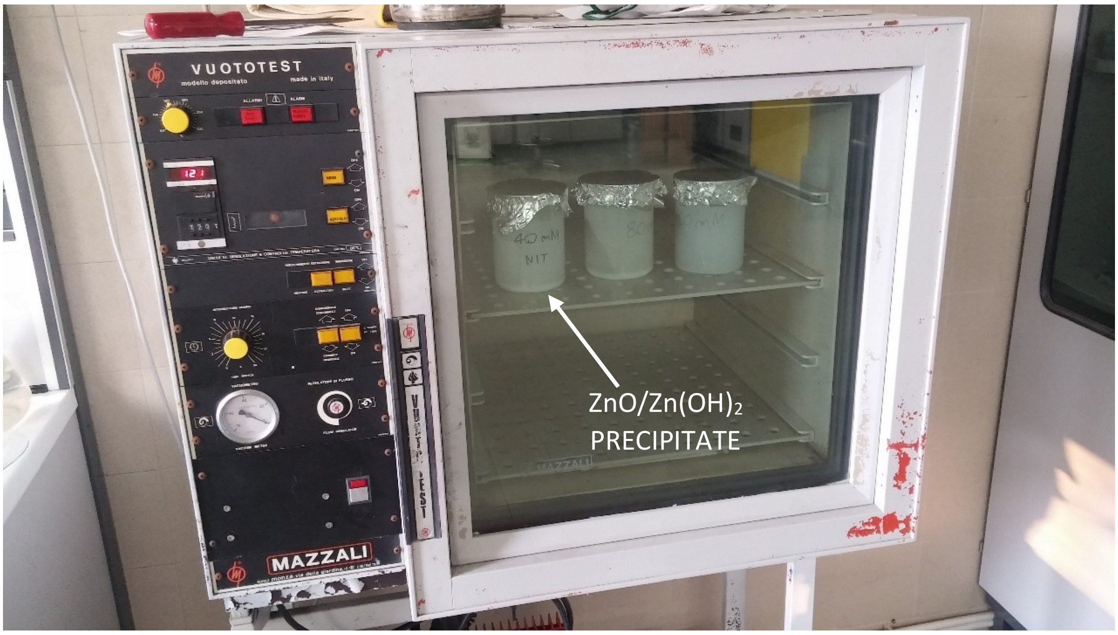

Fig. 42: Growth solutions into the vacuum oven. A white layer is visible at the bottom of the beakers, which is caused by deposition of $Zn(OH)_2$ formed by the alkaline environment originated from HMTA decomposition, and nano/microstructures grown through homogeneous nucleation. These are usually bigger in size with respect to the NRs that grow on the substrate surface, so precipitation occurs despite convective motions. These are, however, responsible for the cloudy appearance of the solution, since smaller nanostructures are transported within the solution.

The investigation about the aspect ratio dependence on precursors concentration is now discussed. The following images show the result of functionalization for progressively higher equimolar concentrations of $Zn(NO_3)_2 \cdot 6H_2O$ and HMTA.

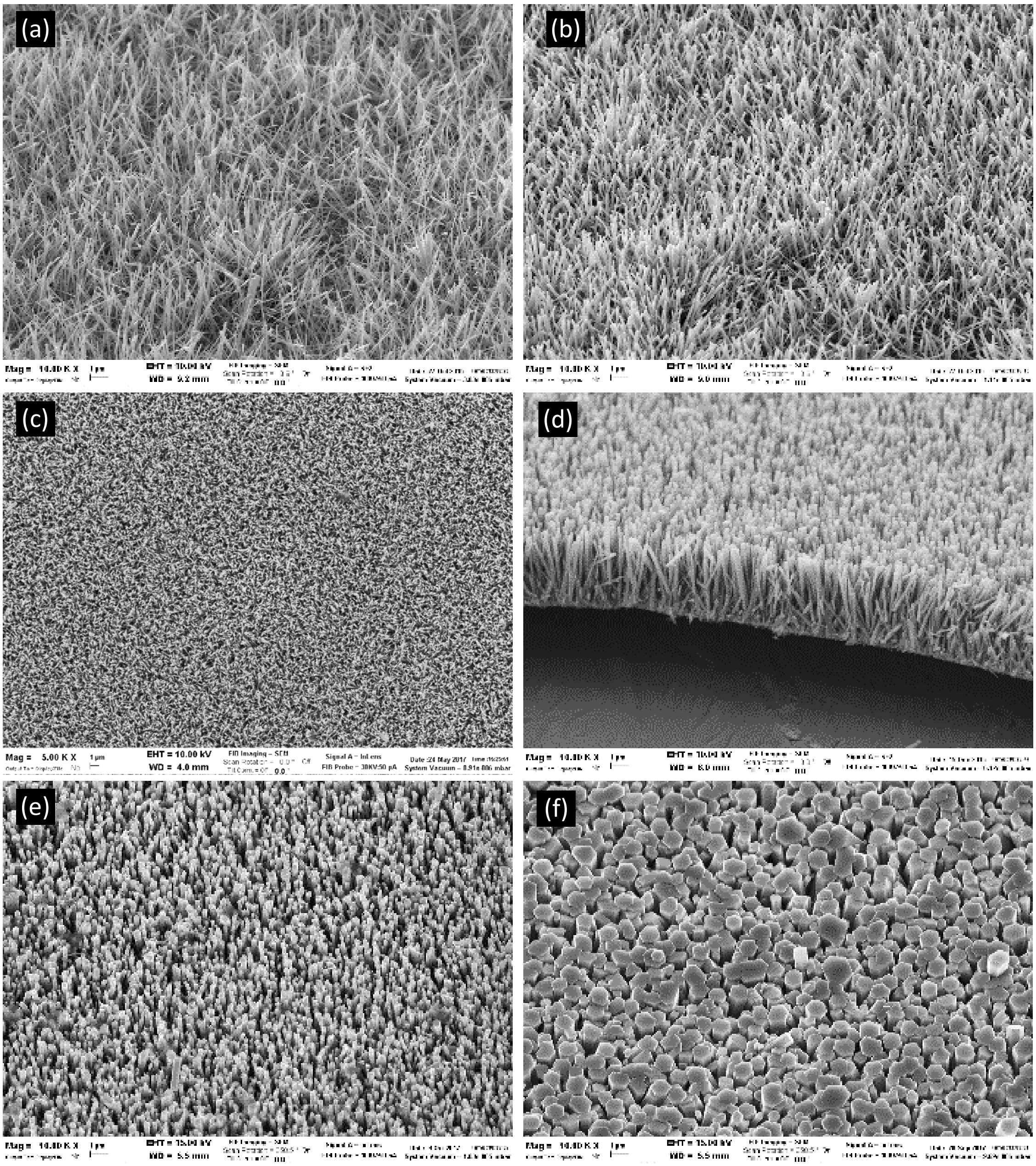

Fig. 43: ZnO NRs functionalization on microscope glasses for equimolar (a) 5:5, (b) 10:10, (c) 20:20, (d) 40:40, (e) 60:60 and (f) 80:80 mM solution of $Zn(NO_3)_2 \cdot 6H_2O$ *and HMTA.*

Results show that the mean diameter of the NRs increases with concentration of precursors, which is consistent with their greater availability for bigger nanostructures. As explained in chapter 3.2, the role of HMTA in the final aspect ratio is to promote axial growth by suppressing lateral one. However, it is evident from the SEM pictures that at higher concentration of both precursors, although equimolar, aspect ratio is more affected by the Zn salt and that HMTA is less incisive.

Analogously to diameter, length as well is influenced by concentration, and this is even more intuitive all the time because, as longitudinal growth is promoted by the presence of HMTA, a higher concentration (or rather, availability) leads to longer NRs.

The density of NRs on the substrate surface is, instead, mainly affected by the initial stages of the growth. The crystalline grains of the SL exhibit random orientation and, for the thermodynamic and kinetic reasons explained in chapter 3, the growth proceeds much faster along the c axis. If the germ grain has the Zn-terminated facet oriented toward the substrate or other directions where space is obstructed, growth runs out. On the contrary, when that favored surface faces free space, the crystal can expand.

As the SL-covered substrate is immersed into the solution, if concentration of precursors is low, nucleation sites that start to appear are spread apart, and even NRs that are not perpendicular to the substrate grow unhindered. The nanostructures result, therefore, unaligned to each other and less dense. Conversely, if precursors concentration is high, the superficial density of nucleation sites raises as well. The nanostructures are now impeded by the neighboring crystals and only the ones perpendicular to the substrate can grow freely. In this case, hence, they appear highly packed and well aligned.

A good alignment is preferable for homogeneity of the piezoelectric signal coming from the crystals, but bending deformation can be limited if the NRs are densely packed. On the other hand low packing (*i.e.* more free space around the NR) exposes the nanostructures to substantial deformation that can lead to damages. A good compromise is the situation exhibited when an equimolar $40:40\ mM$ solution of $Zn(NO_3)_2 \cdot 6H_2O$ and HMTA is used, where NRs are not too thin but they are sufficiently packed.

The role of the two different precursors can be understood by illustrating the result of the functionalization with unbalanced (non-equimolar) concentrations of $Zn(NO_3)_2 \cdot 6H_2O$ and HMTA.

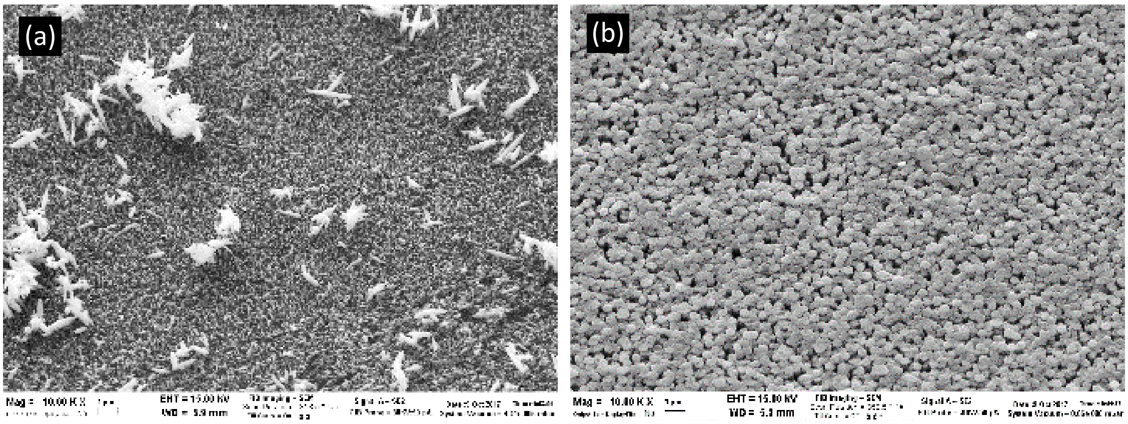

Fig. 44: (a) 10:80 mM solution of $Zn(NO_3)_2 \cdot 6H_2O$ and HMTA, respectively. The sample shows deposition of nano/microstructures grown by homogeneous nucleation and transported onto the surface by convective motions. This exemplifies the situation of an improperly washed sample. (b) Functionalization achieved by an 80:10 mM solution of $Zn(NO_3)_2 \cdot 6H_2O$ and HMTA, respectively.

When a solution of $Zn(NO_3)_2 \cdot 6H_2O$/HMTA with $10:80\ mM$ ratio is prepared, the growth of big ZnO NRs is hindered mainly by two factors: the availability of Zn precursor is low and the lateral growth of the NRs is strongly limited by the high concentration of HMTA. Moreover, pH is relatively high due to the alkaline dissociation of HMTA into NH_3, and this can even bring to a slight crystal corrosion.
In the other case, where the ratio is $80:10\ mM$ for $Zn(NO_3)_2 \cdot 6H_2O$ and HMTA, respectively, HMTA quantity is not enough to impede lateral growth, and the ZnO NRs display greater diameter.
In view of the above considerations, the best compromise is a synthesis with equimolar $40:40\ mM$ solution of $Zn(NO_3)_2 \cdot 6H_2O$ and HMTA. The result is shown in the SEM images below.

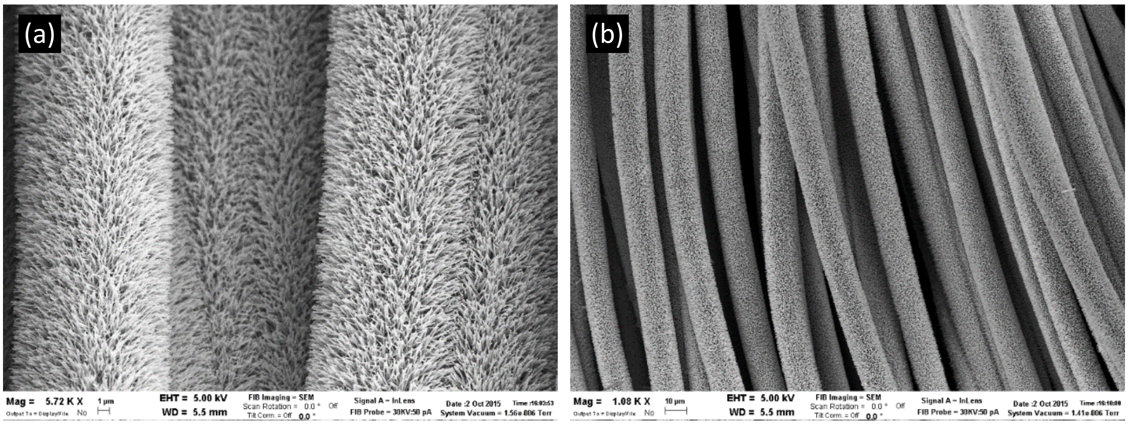

Fig. 45: Complete functionalization of carbon fibers with ZnO NRs by a $40:40\ mM$ *solution of* $Zn(NO_3)_2 \cdot 6H_2O$ *and HMTA for 4 hours at* 95 °C.

It has to be noted that other practical aspects can influence the final geometry of the nanostructures; among these, the most important ones are SL (thickness and density of nanoparticles), the way SL is dried out and substrate position during drying stages and growth.
The hexagonal wurtzite structure of the ZnO NRs is confirmed by XRD analysis.

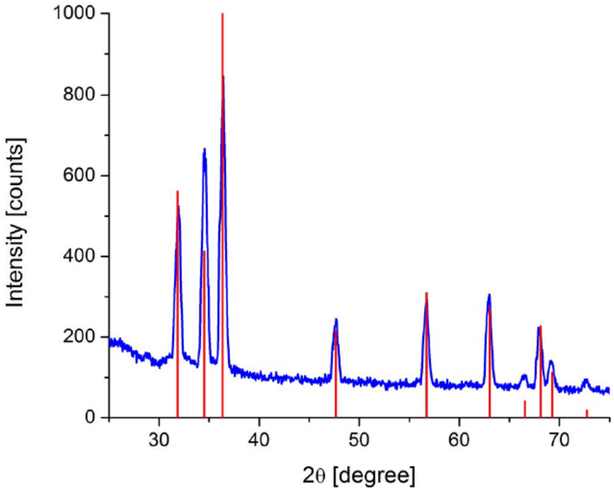

Fig. 46: XRD pattern of the ZnO NRs. All peaks are indexed as hexagonal ZnO ($P6_3mc$ in Hermann-Mauguin notation).

7 Single-fiber device

The first type of device that has been realized is based on single carbon fibers. They are functionalized with *ZnO* NRs by means of the process explained in the previous chapter.
This type of device allows to study the sensing properties of the “first brick” (*i.e.* the single ZfCF) of the target, namely a deformation sensor embedded within CFC.

7.1 Device realization

A whole CFT, containing one thousand carbon fibers, undergoes *ZnO* NRs functionalization. When functionalization is ended and the sample is dried out, single carbon fibers are taken out of the tow by means of tweezers. Carbon fibers and their *ZnO* functionalization layer are fragile, so particular attention is required when ZfCFs are handled with tweezers.
A cross structure is built with two different ZfCFs. They are arranged perpendicularly one on top of the other on a portable substrate. With a view to the embedded device, this structure allows to spatially identify the position the deformation signal is coming from. The lower the crossing area, the higher the spatial resolution, which is ideally ~80 μm^2 in this case owing to the carbon fiber diameter and *ZnO* NRs length. Evidently, such a high sensitivity cannot be reached in a finished composite with the integrated sensor, because stresses in an elastic body result in a deformation gradient, so the spatial resolution depends also on the distance between each sensor, as well as on the mechanical features of the matrix.
Conductive silver paste is deposited on the extremities of both fibers in order to make electrical contacts.

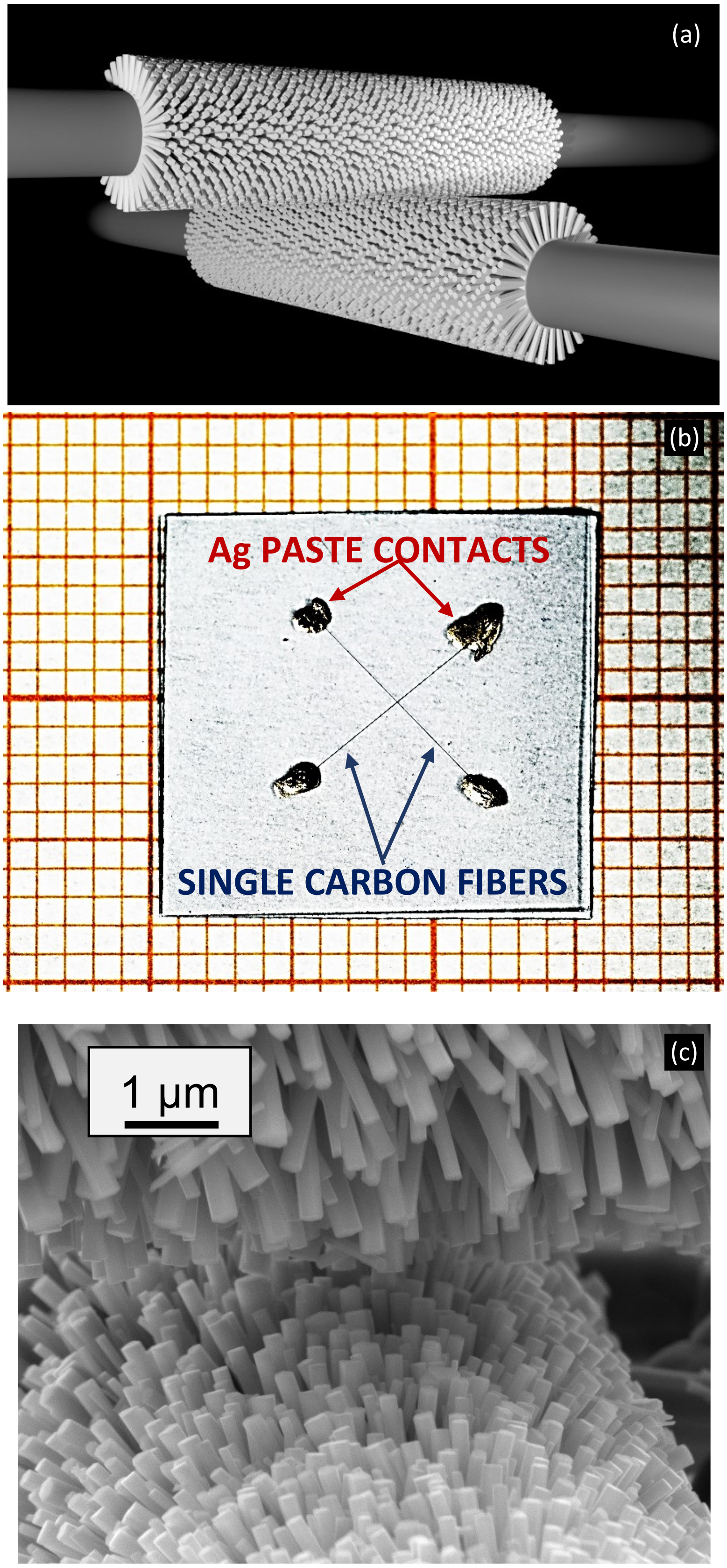

Fig. 47: (a) The wanted structure. (b) The whole single fibers device. (c) SEM image of the crossing point.

7.2 Piezoelectric characterization

The piezoelectric response of the single fiber-based sensor was assessed by means of two complementary techniques:

1) the combination of a DHM and a CM for the direct piezoelectric effect;
2) piezoresponse force microscopy for the inverse piezoelectric effect.

7.2.1 Dynamic hysteresis measurement (DHM) & capacitance measurement (CM)

This piezoelectric characterization consists in a combined two step procedure. The first type of measurement allows to find the electrical frequency at which the material acts as good dielectric, whereas the second one is needed in order to assess the sensing properties.

- **DHM**

The main aim of DHM is to find the impedance behavior of the system as a function of the electrical frequency. Good piezoelectrics (such as PZT) are strong dielectrics; this avoids the interference of free carriers with piezoelectric output, but in materials presenting low-resistivity (*i.e.* high concentration of free charges) this can make piezoelectric measurements particularly difficult.
When a piezoelectric crystal is deformed, displacive charges arise; the free carriers residing within the material feel the electric field generated by the displacive charges and spatially redistribute in order to nullify it and so reducing the energy of the system. This phenomenon is related to the resistive contribution of the material impedance and it can bring to the screening of the piezoelectric charges caused by the free carries.
If the equivalent circuit is considered, to a first approximation the piezoelectric material can be represented by an electric parallel between its internal resistance and capacitance. Impedance is strongly dependent on the frequency of the electrical input; if resistance, capacitance and inductance are in parallel, the inverse of the total impedance Z is the sum of the inverses of the single resistive, capacitive and inductive contributions [211]:

$$\frac{1}{Z}=\frac{1}{Z_R}+\frac{1}{Z_C}+\frac{1}{Z_L}$$

By neglecting inductance, substituting Z_R and Z_C with their explicit form as a function of frequency

$$Z_R = R$$

$$Z_C = \frac{1}{i\omega C}$$

one obtains:

$$\frac{1}{Z} = \frac{1}{R} + i\omega C$$

where i is the imaginary number, R resistance, C capacitance and ω frequency. As shown by the equations, the capacitive impedance is high when frequency is low, so current will preferentially flow through the resistive branch, and vice versa.

Following this considerations, it is possible to emphasize the capacitive behavior of the material, or rather exclude the resistive branch of the equivalent circuit, by changing the input frequency. This is the purpose of DHM in this study.

The wet chemical synthesis does not allow to finely control the concentration of defects. A high concentration of defects causes high concentration of free carriers; the ZnO grown by CBD presents, therefore, low resistivity. The first step, as said, is to find the frequency at which the system acts as good dielectric.

The sample is pre-poled by a semi-periodic triangular pulse (either positive or negative) and then measured through complete triangular pulses (reading pulses) of the same amplitude and frequency. The resulting current is integrated and the obtained charge is plotted as a function of the voltage amplitude.

By fixing carrier wave intensity, modulating wave intensity and sequentially selecting different frequency values, the shape of the polarization-voltage curve is observed, until a linear dependence is obtained.

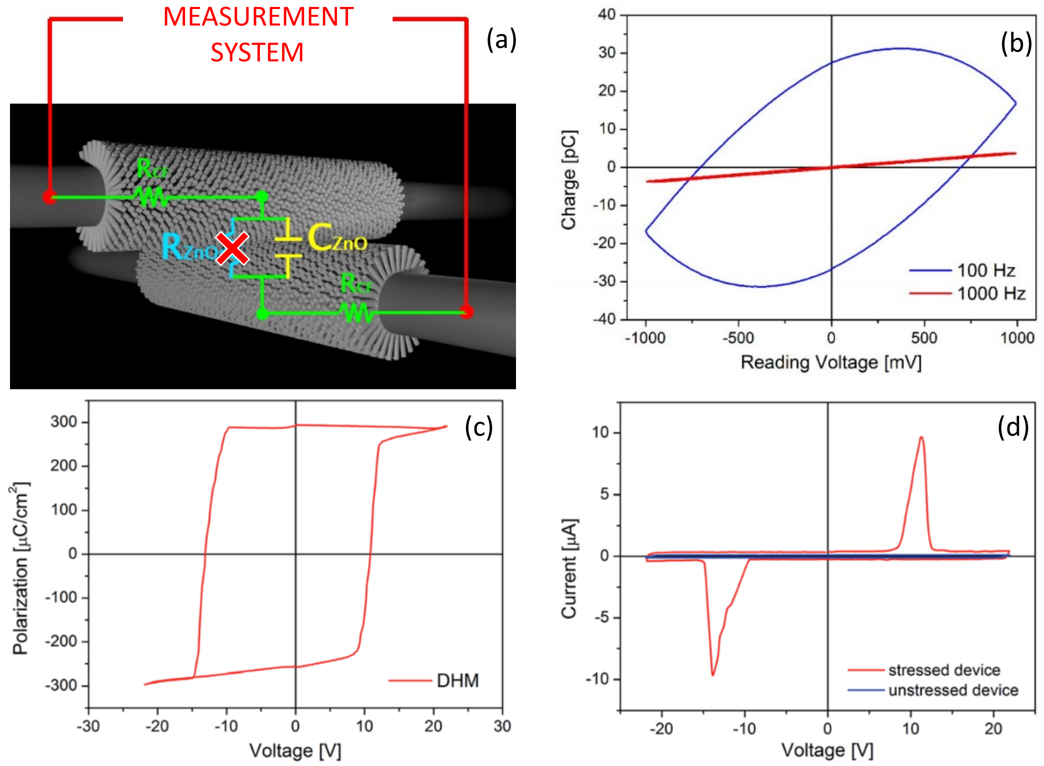

Fig. 48: (a) The role of DHM is to exclude the resistive branch of the equivalent circuit related to the piezoelectric material. (b) The parabolic (blue) and linear (red) polarization/voltage curves corresponding to resistive and capacitive behaviors of the material, respectively, at different frequencies. (c) When the sample is kept under mechanical stress, a typical ferroelectric hysteresis loop is observed. The frequency of electrical input is $900\ Hz$. *(d) Current lobes related to the inversion of the internal electric dipole of ZnO under mechanical stress. It is caused by the application of an electric field that surpasses the ZnO coercive electric field. The current curve is obtained by integrating the ferroelectric loop in (c).*

The frequency of electrical input at which the polarization/voltage curve shows a linear dependence turned out to be $900\ Hz$. The preliminary check is completed: ZnO is now acting as dielectric.

The sample is then kept under mechanical stress by a $50\ g$ load and a $900\ Hz$ electrical input is applied. Under these conditions, a typical ferroelectric hysteresis loop is observed, due to the fact that piezoelectric materials under mechanical stress behave as ferroelectrics. Indeed ferroelectrics can be considered as a particular subset of piezoelectrics presenting non-zero initial polarization. When a piezoelectric material undergoes a mechanical stress, its polarization changes from zero to a certain value, and if this situation is set as initial state, a ferroelectric behavior is observed.

The geometrical quantities are calculated by dividing SEM images of the samples into squares of given side, counting the number of nanostructures inside this square and comparing the number of pixels of the SEM marker with those of the NR characteristic sizes.

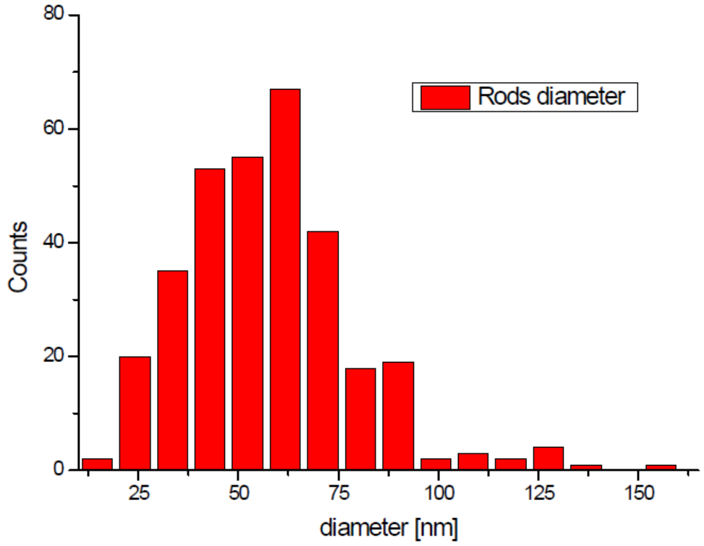

Fig. 49: Diameter distribution of the ZnO NRs.

According to SEM investigation, electric dipoles belonging to the stressed rods are involved within an area

$$A = (35 \pm 7)\ \mu m^2$$

The mean length L and diameter D are about

$$L \approx 2\ \mu m$$

$$D \approx 0.055\ \mu m$$

and a mean ZnO rod surface density σ of

$$\sigma \approx 50\ \mu m^{-2}$$

can be deduced.

Thus, making the approximation that the involved rods equally contribute to the total polarization and considering the saturation polarization

$$P_S \approx (290 \pm 12)\ \frac{\mu C}{cm^2}$$

the net single rod polarization is calculated to be

$$P_{S,NR} \approx (0.12 \pm 0.05)\ \frac{\mu C}{cm^2}$$

Hence, the piezoelectric charge constant d_{33} is derived as the ratio between the saturation charge

$$Q = PA$$

and the external mechanical force, as

$$d_{33} = \frac{Q}{F} = \frac{1.02 \times 10^{-10} C}{0.5\ N} = 20\ \frac{pC}{N}$$

For bulk ZnO, and for an oriented ZnO film, the piezoresponses along the c axis are

$$d_{33}^{ZnO,bulk} \approx 10\ \frac{pC}{N}$$

$$d_{33}^{ZnO,film} \approx 12\ \frac{pC}{N}$$

respectively [212] [213]. The discrepancy of the determined value for d_{33} can be attributed to the approximations of our determination and no speculation on the debated difference of the piezoelectric constants in ZnO bulk and nanostructured samples can be drawn from these data.

- **CM**

At this point the second part of the characterization can be fulfilled: CM is carried out in order to quantitatively assess the sensing properties of the sensor. The capacitance is recorded through small signal capacitance vs. voltage and tangent loss measurements. The applied bias consists in a series of consecutive unipolar excitation pulses, depending on user-defined input parameters (signal amplitude and duration). Such unipolar pulses are DC voltage with a superimposed AC sinewave small signal. The DC bias starts at zero volts, increases up to the desired maximum excitation voltage V_{MAX}, then decreases to $-V_{MAX}$ and is set back to zero. The capacitance and tangent loss measurement are obtained from the AC small signal current by lock-in integration.
The whole sample is encapsulated in ER, in order to create a surrounding that is similar to the real applicative environment of the sensor. Nevertheless, in this case the composite is not manufactured by applying pressure as commonly done in industry; this is to avoid further mechanical stresses on such a delicate structure.
Fig. 3 and 4 report the C vs. V characteristic using an impulsive and a time-invariant excitation, respectively. The unstressed system capacitance collected by applying a staircase voltage with a 900 Hz modulation, results in a mean value of 0.65 pF. Recalling the active element of the proposed device is based on two crossing carbon fibers perpendicular to each other and spaced by a thin layer of dielectric (*i.e.* ZnO NRs layer), the well-known parallel-plate capacitor model no longer fits [214] [215]. According to the calculation proposed by Iossel *et al.* [216] for the aforementioned geometry, the capacitance is defined as:

$$C = \frac{\pi \varepsilon_0 \varepsilon_R l}{(a - b^{(+)} - b^{(-)})}$$

where ε_0 and ε_R are the vacuum and relative dielectric constants and

$$a = ln\left[\frac{1}{r} + \sqrt{1 + \left(\frac{l}{r}\right)^2}\right] + \frac{r}{l} - \sqrt{1 + \left(\frac{r}{l}\right)^2}$$

$$b^{(+)} = \frac{1}{l}\left[2d\, arctan\left(\frac{\sqrt{\frac{l^2}{2} + d^2} + l}{d}\right) + l\, ln\left(\sqrt{\frac{l^2}{2} + d^2} + \frac{l}{2}\right)\right]$$

$$b^{(-)} = \frac{1}{l}\left[2d\, arctan\left(\frac{\sqrt{\frac{l^2}{2}+d^2}-l}{d}\right) - l\, ln\left(\sqrt{\frac{l^2}{2}+d^2}-\frac{l}{2}\right)\right]$$

where l is the wire length, r its radius and d the perpendicular distance between the two wires. The relative dielectric constant of the ZnO NRs has been deduced for $l = 2\,cm$, $d = 4\,\mu m$, $r = 3.5\,\mu m$ and $C = 0.65\,pF$, from which it turns out

$$\varepsilon_R = 7.7$$

in agreement with the value of 7.9 reported for bulk ZnO [217].
By pressing the device with a static $50\,g$ load, the system capacitance increases from 0.65 to $5.30\,pF$ (+715%), indicating the occurrence of an induced polar distortion of the unit cell. Until the weight is retained, the capacitance shows a voltage-invariant behavior and still low $\tan\delta$. Low tangent loss highlights the negligible contribution of the leakage current with respect to the one given by displacive charges, confirming the dielectric origin of the capacitance variation and so the piezoelectric effect.

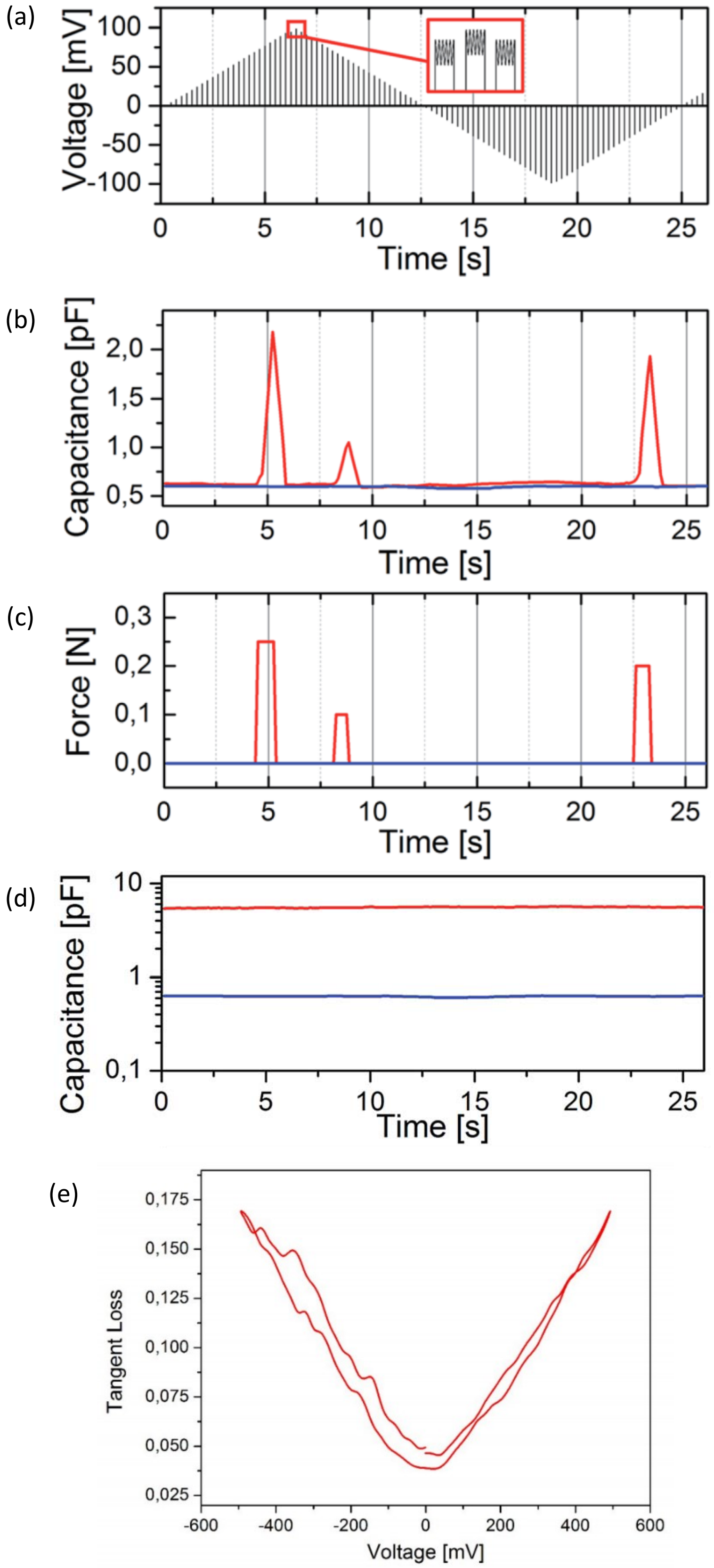

Fig. 50: (a) Input signal during CM. (b) Capacitance peaks corresponding to (c) applied stress. (d) Capacitance increase of $+715\%$ under static load of $50\ g$. The red line corresponds to the stressed sensor, whilst the blue line is the response of the sensor in its unperturbed state. (e) Typical $\tan\delta$ behavior for the studied samples.

As highlighted by fig. 50/b-c, the sensor shows excellent proportionality between applied stress and capacitance response. the capacitance variation takes into account the dielectric permittivity variation because of the structural polarization when the stress is applied; at the same time the narrowing of the gap between carbon fibers cannot be ruled out (*i.e.* the device under test acts as a capacitor and the mechanical stress causes a variation of the plates distance). A correct interpretation of the phenomena must take into account Fig. 48/a: the presence of symmetric polarization lobes states the main contribution to the capacitance variation is due to the dielectric permittivity increase (because of a polar structural transition) rather than a narrowing of the capacitor plates.

7.2.2 Piezoresponse force microscopy

An AFM disc is coated with silver paste, then a ZfCF is half immersed laying horizontally in the conductive paste until this is completely dry. The Pt-coated silicon tip of the PFM is placed on top of a ZnO NR with contact force of $10\ nN$. Then, AC voltage of 0 to $5\ V$ with $17\ kHz$ is applied from a lock-in amplifier to the ZnO NR and the subsequent axial deformation, due to the piezoelectric effect, is measured.
d_{33} of ZnO is calculated as the ratio between the slope of the ZnO PFM curve and the one of the quartz reference. Piezoresponse is a dimensionless quantity since it is related to the value of the reference:

$$d_{11}^{x-quartz} = 2.3\ \frac{pm}{V}$$

For all the measurements, the linear regime is evaluated.

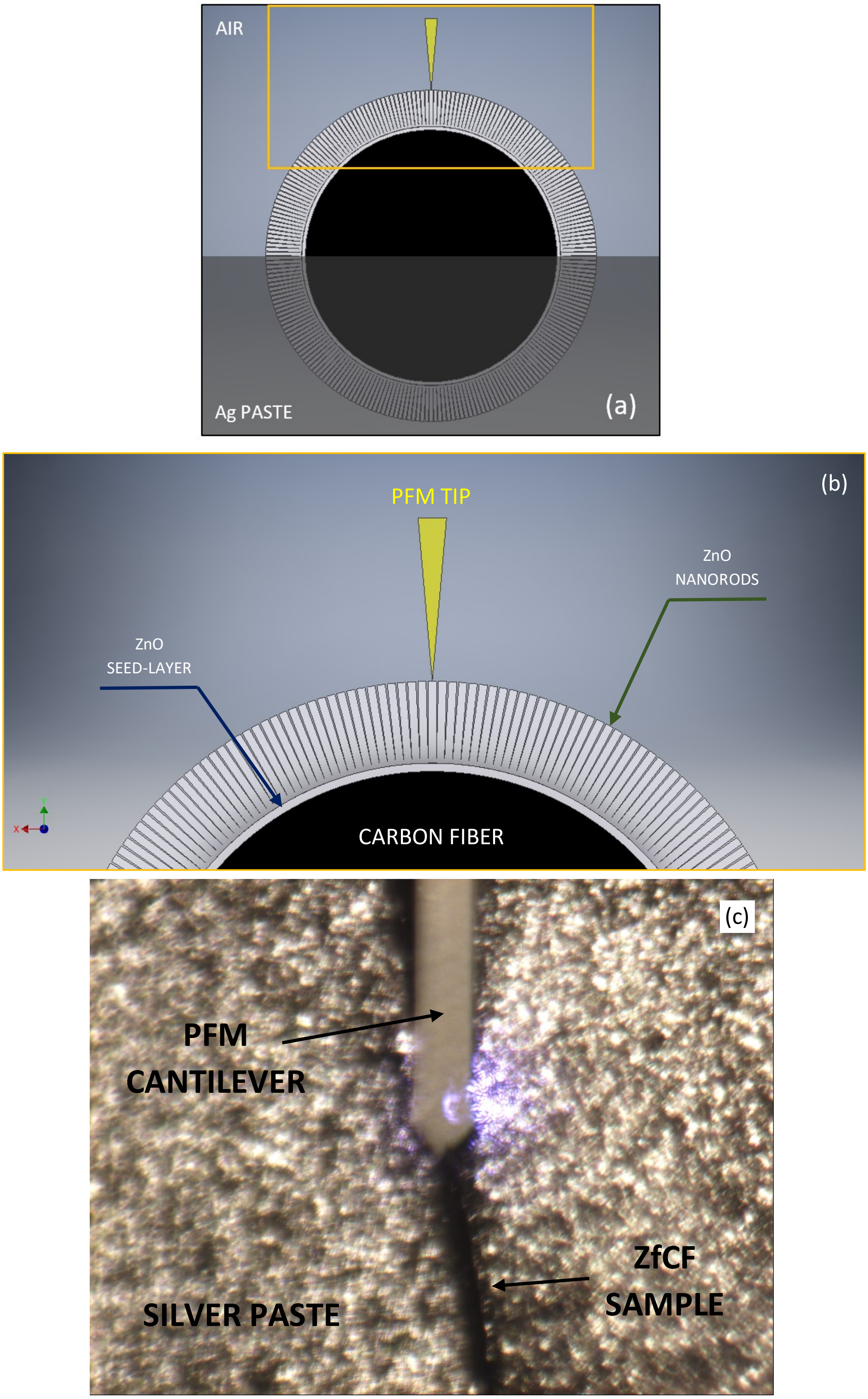

Fig. 51: Cross-section depiction of the ZfCF half-immersed in silver paste for PFM analysis and (b) enlargement of the orange window in (a). PFM tip dimension and SL thickness are exaggerated for figurative purpose. (c) Optical magnification of the ZfCF sample undergoing PFM analysis.

- **ZnO NRs grown by CBD**

The first analyzed sample is a carbon fiber with ZnO NRs grown by the alkaline CBD explained in chapter 3.

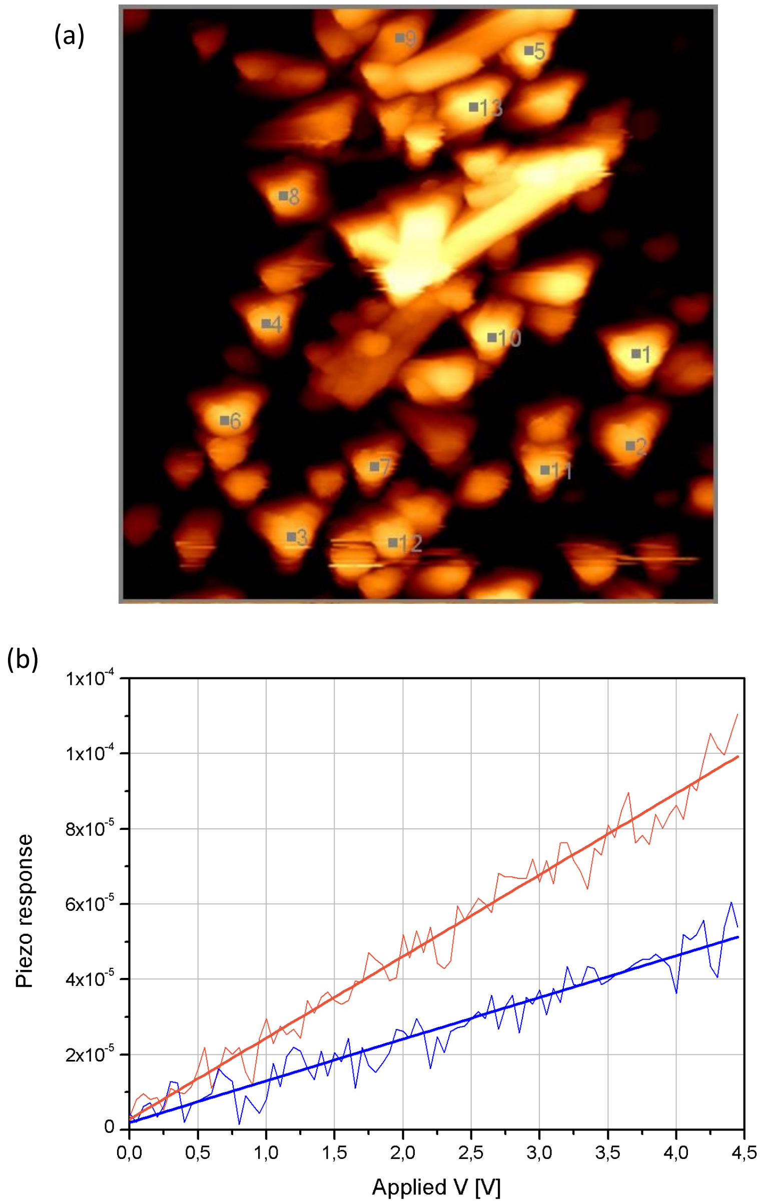

Fig. 52: (a) AFM image of the measured NRs. The image is taken by means of the PFM system itself. (b) Piezoelectric response of ZnO (orange) and reference quartz (blue).

The highest value obtained for the piezoelectric coefficient is

$$d_{33}^{ZnO,CBD} = (4.5 \pm 0.1)\,\frac{pm}{V}$$

which fits with the known range for ZnO samples [218]:

$$0.4\ \frac{pm}{V} < d_{33}^{ZnO} < 26.7\ \frac{pm}{V}$$

It should be noted that the measured value of $d_{33}^{ZnO,CBD}$ could be slightly underestimated due to:

- non-high rigidity of the underlying material (deformation is symmetrical with respect to the center of the nanostructure);
- misalignment between AFM tip and NR axis: under application of voltage, ZnO NR can stretch (or compress) not only along Z direction, but also with XY contribution.

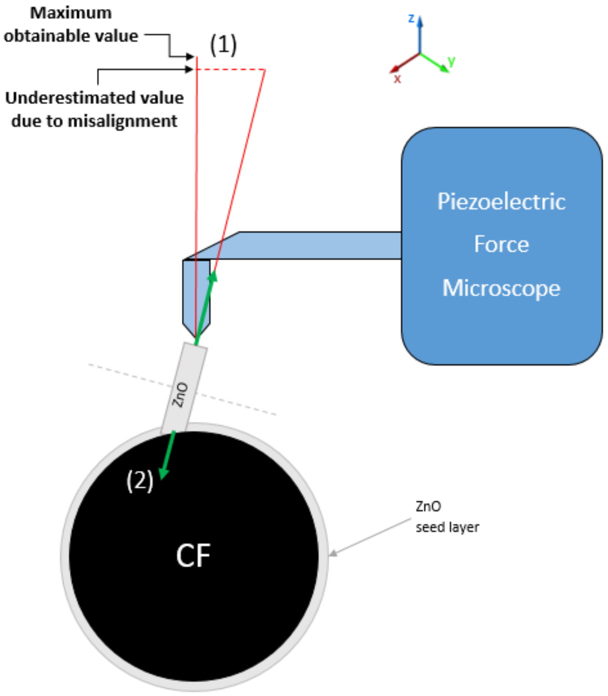

Fig. 53: Possible sources of slight underestimation of the piezoelectric coefficient values measured by PFM technique.

The wide range of d_{33}^{ZnO} values, reported in [218], can be attributed to the different morphologies (nanostructures, bulk, thin film, etc.), but also to the growth methods. These can, in fact, origin different concentrations of defects, or rather, of free charges that screen the piezoelectric effect. The influence of a different concentration of free charges can be observed by comparing samples grown by means of different techniques.

- **ZnO NRs grown by vapor phase technique**

The ZnO NRs grown by vapor phase technique are synthesized at IMEM-CNR by Dr. Davide Calestani [219].

The growth of ZnO NRs was carried out inside a laboratory scale reactor (a tubular furnace), through which it is possible to flow different gases. The used source material is pure metallic Zn powders (5 N purity, $300\,mg$) that are softly etched before use in 1:100 diluted HNO_3 for 1 minute. This etching process is fundamental in order to remove the native oxide and to make possible a maximized and reproducible Zn evaporation from source material.

ZnO seed-film is deposited on glass substrates by means of Pulsed Electron Deposition (PED). Films with thickness in the $100 \div 800\,nm$ range are used. The source and substrate are placed one next to the other, with the substrate in a downstream position, at the center of the furnace. Source material is partially covered, so that generated vapor could exit only through a small window. The growth procedure consisted of three main steps. The process starts by increasing the temperature up to $480\,℃$ in an Ar/O_2 mixture (20:1 mass ratio, $50\,sccm$ total flow). Once the maximum temperature is reached, furnace heating is maintained for 5 min. Then the Ar/O_2 mixture is substituted by a larger Ar flow ($250\,sccm$) and furnace starts cooling down. Finally, the substrate is collected and characterized.

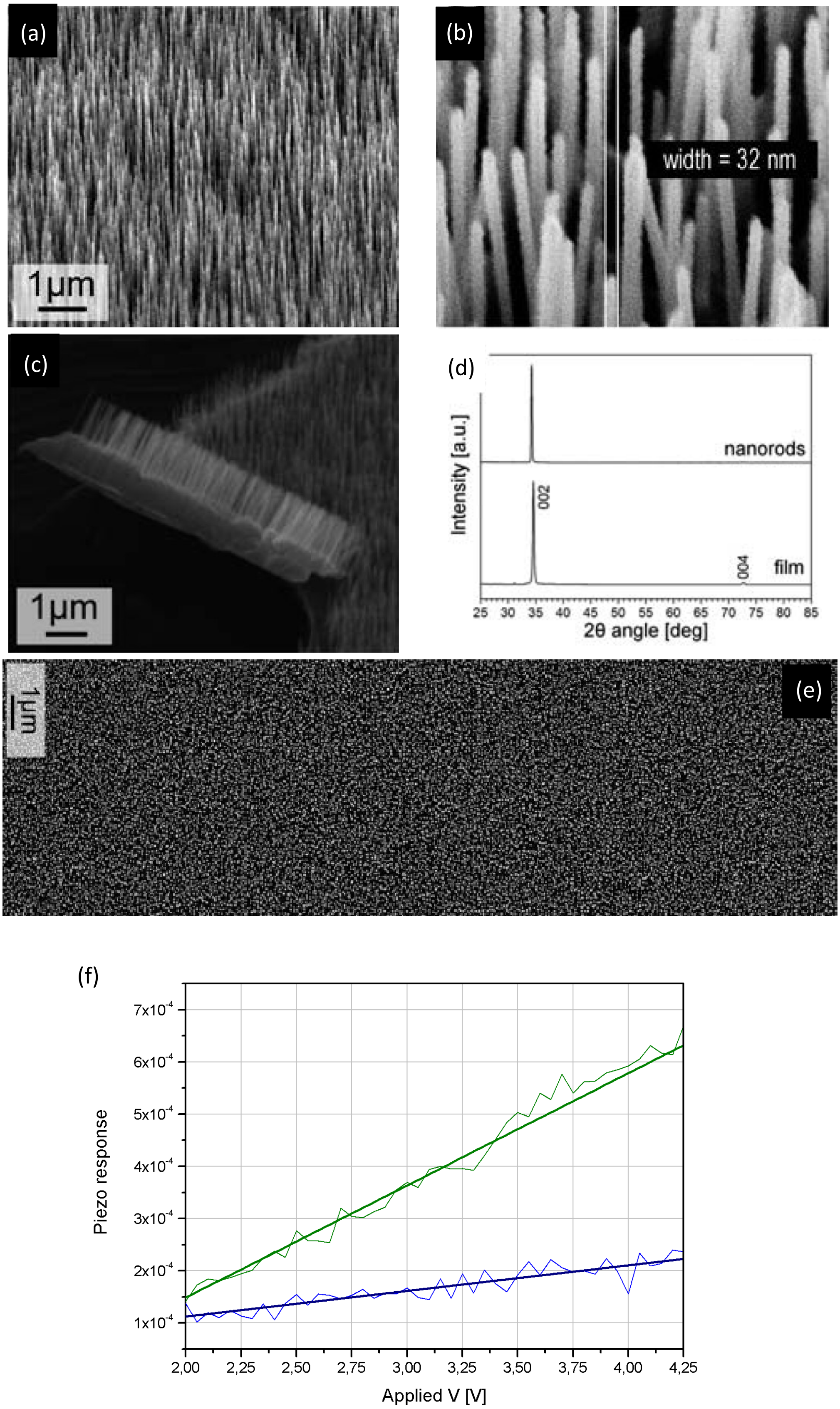

Fig. 54: (a-c, e) ZnO NRs grown by vapor phase at IMEM-CNR. (d) XRD of the same sample. (f) Comparison between piezo response of vapor phase grown ZnO NRs (green) and quartz reference (blue).

For ZnO NRs grown by vapor phase technique the piezoelectric coefficient rises to

$$d_{33}^{ZnO,VP} = (10.1 \pm 0.9)\ \frac{pm}{V}$$

with a ~124% increase with respect to the CBD-grown.
NRs grown by vapor phase exhibit a higher d_{33}. This technique allows indeed to obtain ZnO with lower concentration of defects with respect to CBD. In fact, the purity of the precursors in the latter is limited to the first percent decimal place, whereas those used in vapor phase growth reach the fifth. The bidistilled water used as solvent in CBD presents limited purity as well.
Therefore, the piezoelectric response in the case of vapor phase-grown nanostructures is less screened because of the lower concentration of free charges.

- **Time-dependent PFM during UV irradiation**

The bandgap of ZnO is 3.37 at $25\,℃$, corresponding to approximately $368\,nm$ wavelength. Being ZnO a n-type semiconductor, by exposing it to light with higher energy compared to this value, electrons are promoted to the conduction band and become free carriers. As mentioned in the previous paragraphs, free carriers screen the piezoelectric charges; it is possible, therefore, to analyze the time-dependence of piezoelectric coefficient on the presence of free carriers when their concentration is pushed to raise.
A ZfCF by CBD is prepared for UV exposure and successive PFM analysis. As in the first PFM measurements, an AFM disc is coated with silver paste, then a ZfCF is half immersed laying horizontally in the conductive paste until this is completely dry; this system is then irradiated with UV light for 30 minutes.
The UV source for irradiation of the sample is a Lichtzen INNO CURE 100N with $100\,W$ High Pressure Mercury Short Arc Lamp, emission peak at $365\,nm$, from which light is conducted toward the sample through a flexible liquid light guide [220] [221].

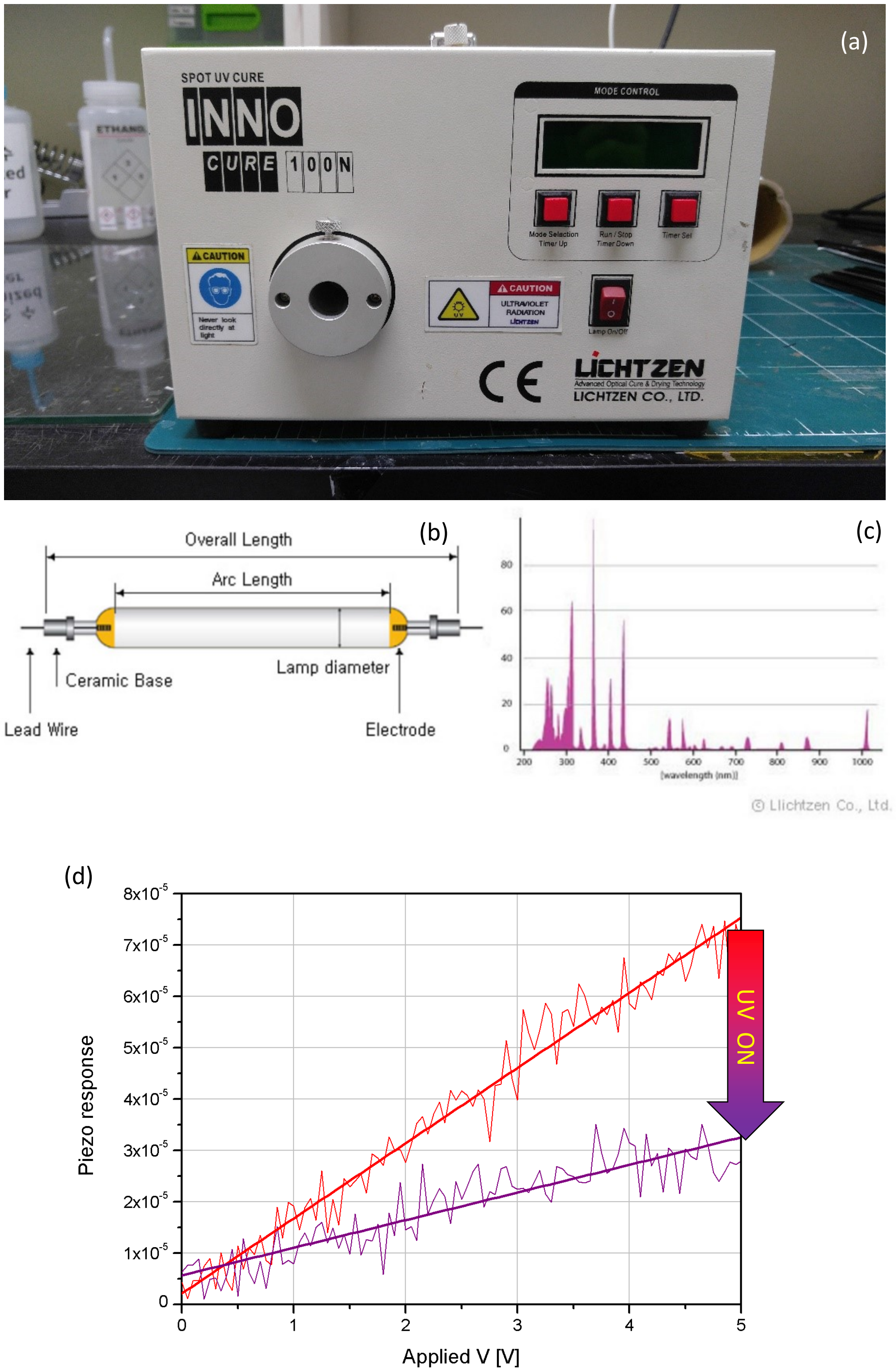

© Llichtzen Co., Ltd.

Fig. 55: (a) The Lichtzen INNO CURE 100N UV source used for sample irradiation at NESEL, South Korea. (b) Structure of a High Pressure Mercury Short Arc Lamp and (c) emission spectrum. (d) Decrease of the piezoelectric coefficient of ZnO NR caused by UV irradiation. The red line corresponds to the sample response before UV exposure, while the purple one arises after 30 minutes irradiation.

After 30 minutes of UV exposure, the piezoelectric coefficient of ZnO NRs decreases by ~63%, revealing its strong dependence on the concentration of free carriers.

8 Tows device

Single carbon fibers are not easy the handle due to fragility and size. It should be remembered that the mechanical features of CFCs derive from the overall arrangement of the single carbon fiber fabrics that constitute the composite itself. For these reasons, in industrial field carbon fibers are handled in the form of fabric; it is essential, therefore, to design a device that is as close as possible to the common raw material, making it more suitable for industrial processes. After the realization of a piezoelectric sensor based on single carbon fibers, it is necessary to step forward toward a CFT-based device.

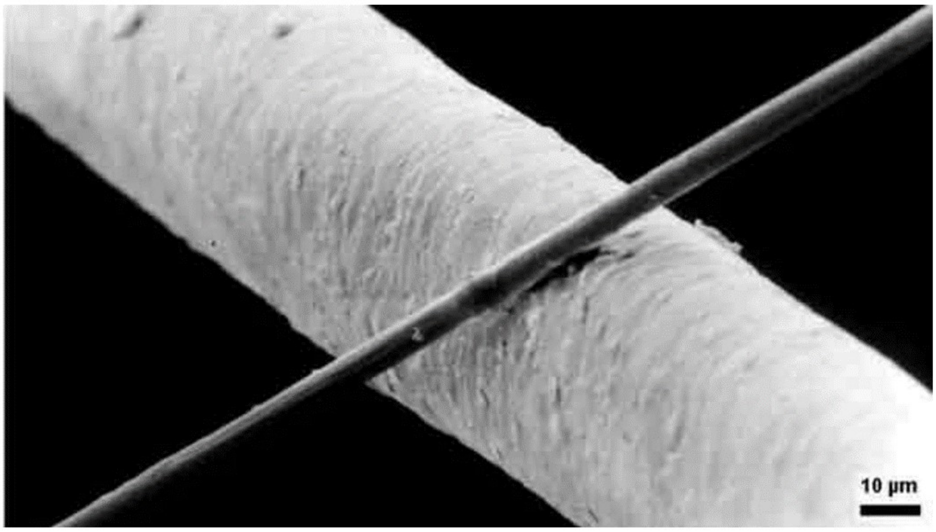

Fig. 56: Comparison between human hair and carbon fiber size [222].

8.1 Device realization

The structure of the piezoelectric sensor based on CFTs is analogous to that based on single fibers. Two CFTs (containing one thousand carbon fibers each) are placed one above the other in perpendicular way, forming a cross. As in the case of the single fibers, spatial resolution depends on the crossing area, which is here augmented to some hundreds of square micrometers; hence, sensitivity is slightly reduced with respect to the previous case, but the mechanical considerations about elasticity explained in chapter 7.1 must be taken into account.

Conductive Ag paste is deposited at the extremes of each tow for the creation of electrical contacts. This way the carbon fibers inside each tow are electrically in parallel to each other.

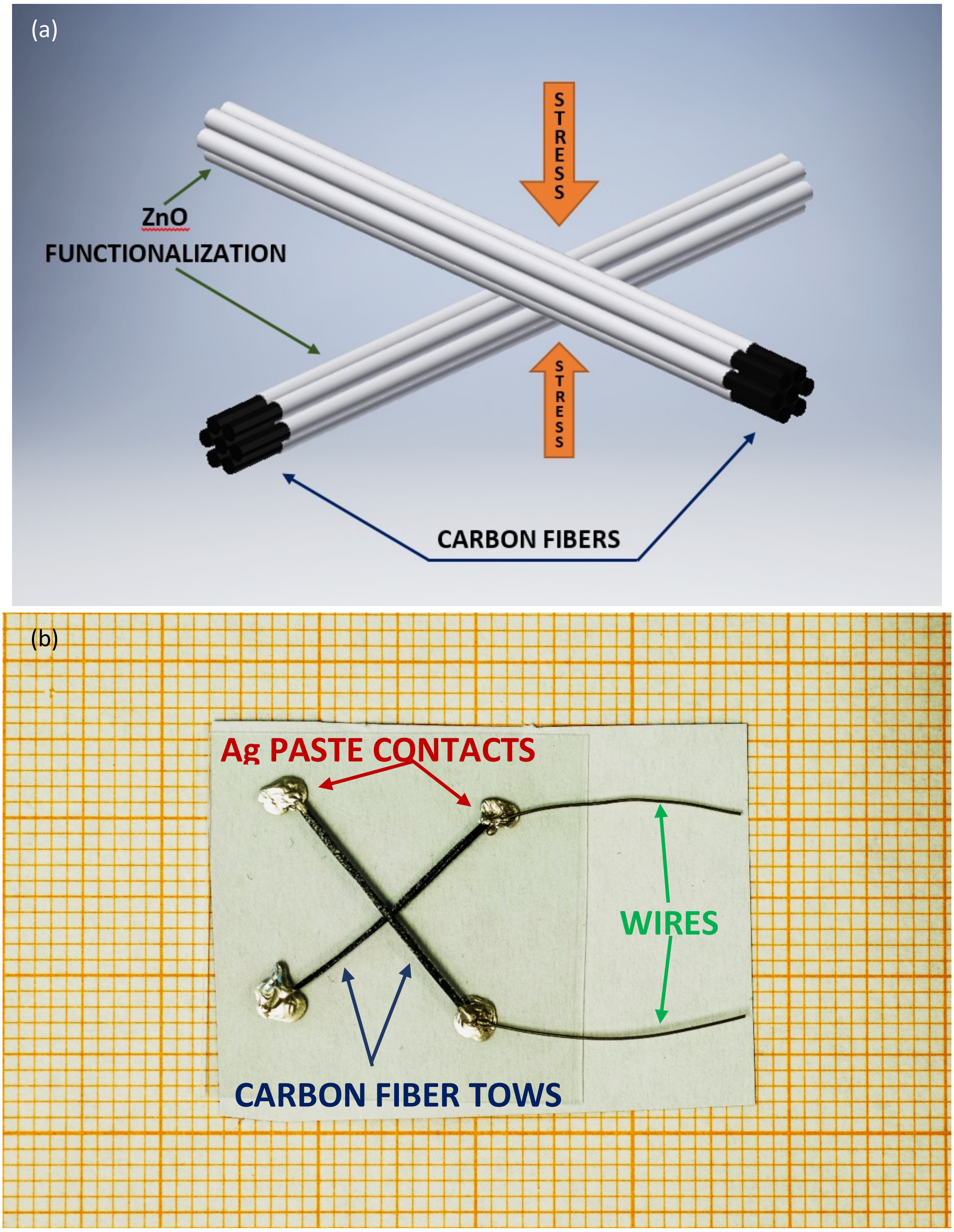

Fig. 57: (a) Crossed arrangement of the piezoelectric sensor based on CFTs. Only seven fibers are represented in each tow for graphic facilitation. (b) Real image of the device.

8.2 Piezoelectric characterization

In this case, the piezoelectric characterization is carried out only by means of the DHM and capacitance analysis. In fact, the sample setup for the PFM investigation displayed in chapter 7 is specifically built for a single functionalized CF.

A pressure is applied perpendicularly to the crossing point. The functionalized CFs composing a single tow stand parallel to each other. Since always the outer [0001] faces of the ZnO NRs are zinc-terminated (positively charged) and the [$000\bar{1}$] faces (the ones toward the CF) are oxygen-terminated (negatively charged) [49] [223] [224] [225], this configuration allows to collect and sum the piezoelectric signal from each wire, which increases the overall output.
Once the correct frequency is found by means of DHM, CM is carried out. By applying pressure pulses, capacitance peaks arise which are proportional to the intensity of the stimulus. With a load of about 30 g, capacitance can rise up to 508% of the value observed in the state of non-stressed device.

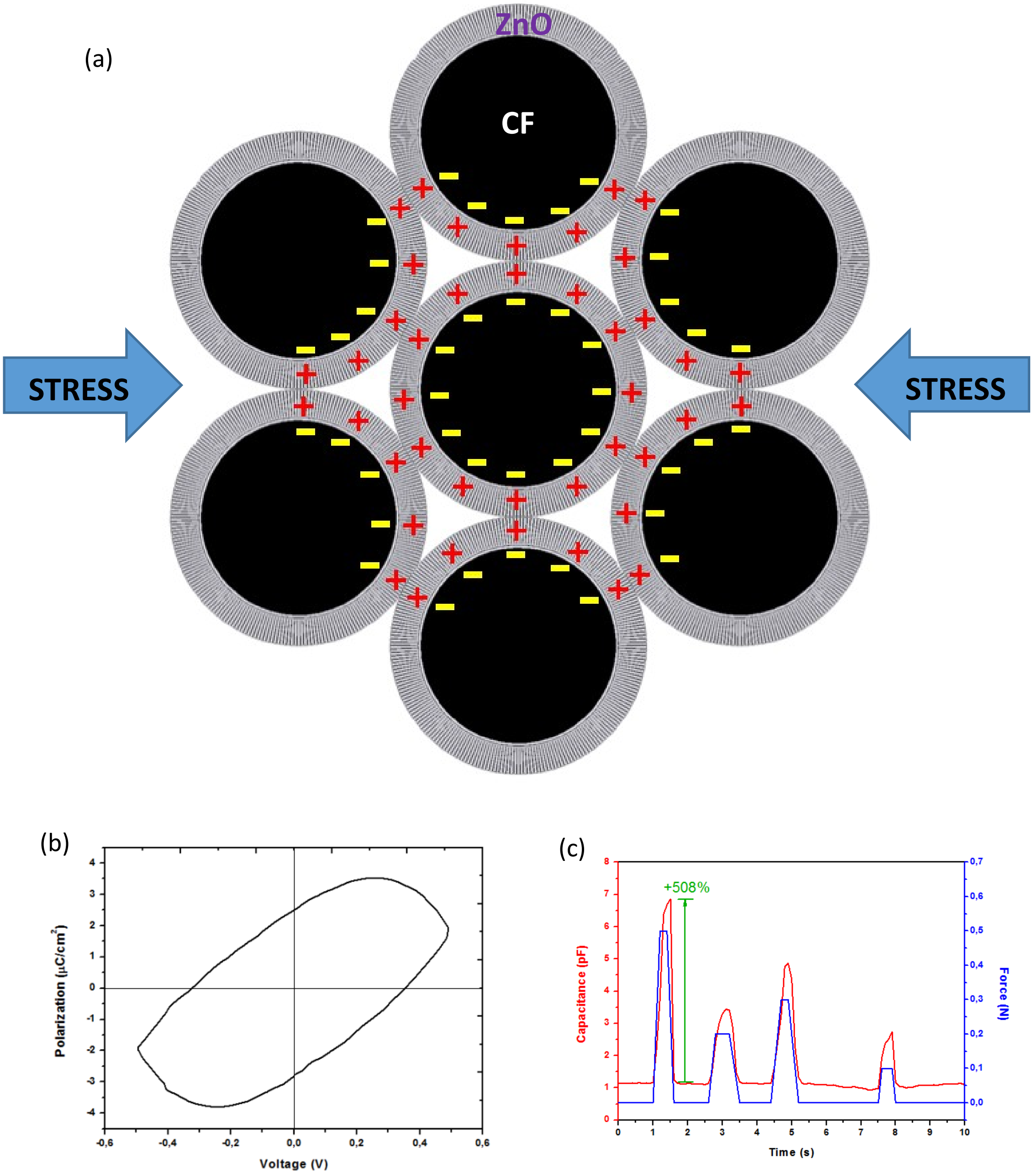

Fig. 58: (a) Sum of same-sign piezoelectric charges due to oriented zinc- and oxygen-terminated faces of ZnO NRs. (b) DHM at $5\ kHz$. (c) Applied force of random intensities (blue line) and resulting capacitance peaks (red line).

9 Embedding the sensor within the carbon fiber composite

The ultimate objective of the work is to embed the ZnO/CF sensor within a CFC, in order to measure in real time deformations the composite is undergoing. Owing to the fact that carbon fibers themselves are functionalized and work as electrodes, the device is completely integrated into the composite structure.

The embedding process is the most delicate step of the creation of a self-sensing CFC. Interactions between resin and device, strains during and after resin exsiccation, interferences between the electrical/mechanical properties of resin, ZnO and carbon fiber, geometrical configurations and aggressive industrial procedures are the most critical issues of this stage.

9.1 Epoxy resins

ER is the most common matrix for CFCs owing to the exceptional mechanical features. The history of this material began in 1909 when the Russian chemist Nikolaus Prileschajew discovered the chemical reaction of an alkene with a peroxy acid to form epoxides, known indeed as Prileschajew reaction [226], whilst its commercial marketing started in 1947.

The prefix “epoxy” refers to a bridge consisting of an oxygen atom bonded to two other atoms already linked in some way, but generally it concerns to the three-membered ring where the atoms to which oxygen is bonded are carbon. The capability of this epoxy group to undergo a large variety of addition and polymerization reactions leads to the class of ERs [227].

ERs are polymeric materials and their name is applied to both the prepolymers and to the cured resins; the former contain reactive epoxy groups, hence their name. In the cured resins, all of the reactive groups may have reacted, so that although they no longer contain epoxy groups the cured resins are still called ERs [228].

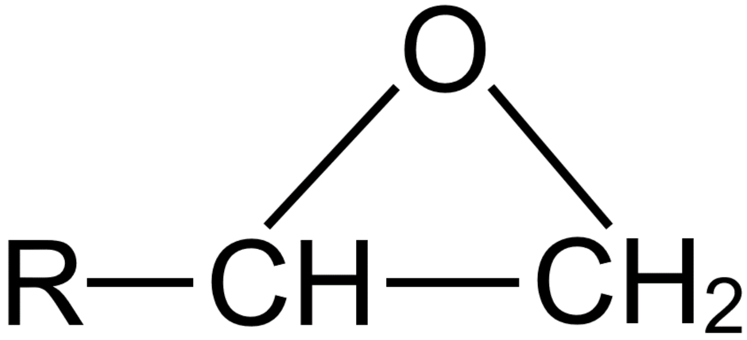

Fig. 59: Terminal epoxy group.

Resins employed in this work are supplied by ELANTAS GmbH - Electrical Insulation branch, Lemignano di Collecchio (Parma).
The reaction between precursor resin and hardener results in the formation of the ER. Different combinations of precursor resin and hardener are used in this work (following ELANTAS specifications and preparation procedures) in order to obtain ERs with appropriate properties. Examples of mechanical and electrical properties are reported in tables 5 and 6.
The two starting components, namely resin and hardener, are homogenized by stirring and mixed together in order to form the epoxy system. Care must be taken to avoid formation of air bubbles during mixing, so as not worsening the mechanical features of the final product.

	Resin	**Hardener**	**Weight ratio**
Epoxy system #1	Elan-tech® EC 251	Elan-tech® W 242 NF	100:40
Epoxy system #2	Elan-tech® EC 152	Elan-tech® W 152 MR (medium reactivity)	100:30

Tab. 4: The two epoxy systems supplied by ELANTAS for this work are Elan-tech® EC251/W242NF and EC152/W152MR.

	Epoxy system #1
Dielectric constant	8÷10
Leakage factor [$\times 10^{-3}$]	300÷400
Volume resistivity [$\times 10^{10}$ Ω·cm]	1.5÷3.5
Dielectric strength [kV/mm]	15÷18

Tab. 5: Electrical properties of the epoxy system obtained by mixing Elan-tech® EC 251 and Elan-tech® W 242 NF.

	Epoxy system #2
Resin viscosity [mPa·s]*	1200÷1800
Hardener viscosity [mPa·s]*	30÷60
Resin density [g/ml]*	1.13÷1.17
Hardener density [g/ml]*	0.94÷0.98
Employment time [min]*	35÷45
Exothermic peak [°C]*	210÷235
Initial viscosity [mPa·s]*	400÷600
Gel time [h]*	5÷7
Mould-release time [h]*	6÷8
Density [g/ml]*	1.08÷1.12
Hardness *	85÷89 Shore D/15
Glass-transition temperature [°C]	85÷90
Water absorption [%]	0.15÷0.25
Maximum working temperature	95 °C
Flexure resistance	120÷130 MN/m^2
Maximum deformation	5÷7%
Deformation at breakage	6÷8%
Flexure elastic modulus	3400÷3800 MN/m^2
Traction resistance	65÷75 MN/m^2
Elongation at breakage	6÷8%
Compression resistance	95÷105 MN/m^2

Tab. 6: Mechanical characteristics of the single components and the epoxy system obtained by mixing Elan-tech® EC 152 and Elan-tech® W 152 MR (value at 25 °C).*

9.2 Composite realization

The final composite is realized by means of a vacuum bag process. Pre-impregnated fabric is employed so as to avoid the step of pouring resin. The so-called "pre-preg" is stored in a refrigerating room to prevent polymerization; moreover, low temperatures maintain the resin extremely viscous, so it is possible to handle it without the inconvenience represented by its stickiness.

Two layers of pre-preg are laid on a flat and clean aluminum surface, previously treated with releasing agent in order to allow detachment of the polymerized composite, and the cross-like sensor is placed. This displays a certain thickness with respect to the surrounding areas, where carbon fibers are absent. It is necessary, therefore, to insert additional layers of pre-preg above those areas because, during vacuum bag process, pressure is applied homogeneously over the whole sample area for composite strengthening; if an extra layer is present at the point where carbon fibers are located, the pressure will focus right there, strongly intensifying the applied stress and possibly leading to damages. Other two layers of pre-preg are added in order to close the sandwich structure, which is eventually put into the vacuum bag as shown in the following illustration.

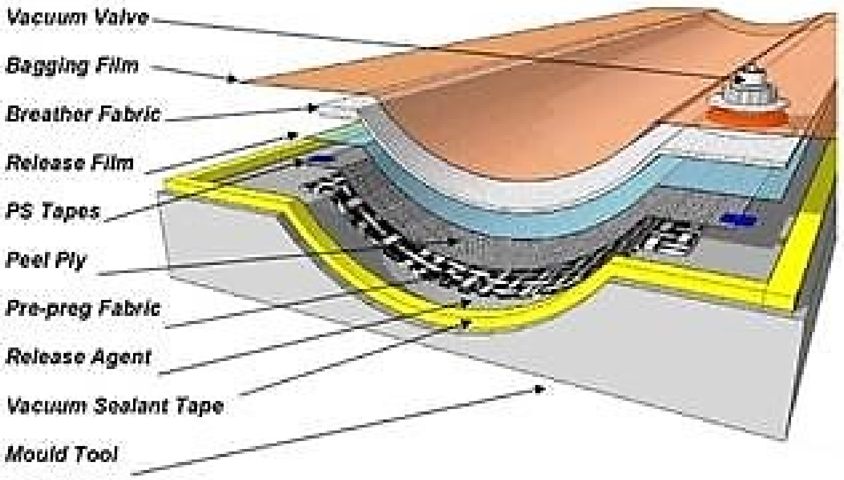

Fig. 60: Layered view of the elements that come into play during vacuum bag process for the realization of a CFC.

The whole system undergoes vacuum process at 130 °C for 120 minutes, with heating-up ramp of 20 minutes and cooling-down ramp of 10 minutes. This allows, other than compacting and reinforcing the composite, to remove air bubbles that could worsen the mechanical features.

9.3 Mechanical characterization

A whole carbon fiber dry patch (200 $^{g}/_{m^2}$ plain weave – PW, measuring $200 \times 200\, mm$) is functionalized with ZnO NRs as described in chapter 3. This patch is used as a standard ply during sample lamination. Two laminates are considered for the characterization: the first laminate consists of 20 plies of carbon fibers (200 $^{g}/_{m^2}$ PW), impregnated with ER; the second laminate consists of 19 plies of CF 200 $^{g}/_{m^2}$ PW, impregnated with ER, plus the ply functionalized with ZnO NRs. The latter is inserted as the central ply. Each laminate is put into a vacuum bag, heated in an autoclave at 130 °C, and pressurized at 6 bar.

InterLaminar Shear Strength (ILSS), is evaluated according to ASTM D2344 industrial standard (short-beam strength of polymer matrix composite materials and their laminates).

Five samples (S1–S5) are obtained from each laminate and tested for ILSS. Among all mechanical properties, shear properties are the most influenced by the presence of an extrinsic material between plies, and such measurements can be considered as the worst-case scenario for the proposed device. ILSS results and force vs. deformation plots are reported.

	S1	S2	S3	S4	S5	Average	σ_{mean}
ILSS CF [MPa]	59.9	61.6	61.0	60.9	60.7	60.8	0.27
ILSS ZfCF [MPa]	59.6	60.8	58.4	54.9	54.9	57.7	1.2

Tab. 7: ILSS analysis for CFC (1st row) and CFC made of ZfCFs (2nd row).

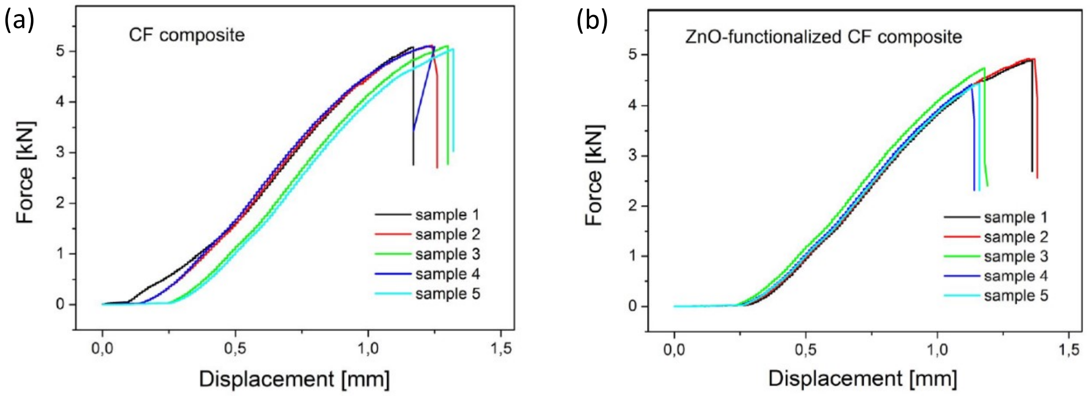

Fig. 61: ILSS measurement performed on pristine CF composite material (a) and ZfCF-based composite material (b).

Significantly, the ILSS average values measured for pristine carbon fiber and functionalized CF differ by a mere 5%. Such a low value points out the excellent integration of ZfCF into the composite laminate. The standard deviation of the mean σ_{mean} calculated for ZfCF is slightly higher than that measured for carbon fibers; this can be tentatively ascribed to either the non-homogeneous distribution of ZnO NRs or the different sizing of ER with respect to carbon fibers and ZfCF. Further studies are required to investigate this aspect.

Above all, the mechanical performance of the composite laminate material is essentially unaffected by the ZnO NRs functionalization and paves the way to the large-scale integration into structural parts of interest.

9.4 Critical aspects

The ZfCF sensors are inserted between the pre-preg layers both with and without ER protection. For the sensing characterization of the ZnO-based devices, in this work glass fiber pre-preg is used rather than carbon fiber, in order to prevent unwanted short circuits.

When the resin protection is absent, ZnO NRs undergo high stresses that can bring to damage them. These are mainly caused by two factors:

- Pressure applied by the vacuum bag system.
- Tensile and compressive forces during polymerization.

None of the unprotected tows embedded within the CFC emerged undamaged, so it was not possible to measure any piezoelectric signal. Almost the totality of sensors showed short circuits between the CFTs. For this reason, a thin epoxy sheath is deposited through diluted ER system #2, which is preferable owing to its mechanical stiffness.

If the normal resin/hardener ratio is employed, the resulting resin exhibits very high viscosity that does not allow to control thickness on the CFTs. In order to reduce viscosity (so the thickness) acetone is used to dilute the resin precursor, which is finally mixed with hardener. The optimized resin/diluent/hardener weight ratio turns out to be 1: 6: 0.3 (the resin/hardener ratio is already fixed by data-sheet specifications and cannot be changed to attain correct polymerization). A higher amount of diluent (acetone) leads to a non-sufficient thickness of ER, while a lower one keeps viscosity high. The functionalized CFTs are dipped into the diluted epoxy mixture and placed on blotting paper, to remove exceeding resin, at room temperature for 24 hours. This process is repeated twice in order to obtain a sufficient resin layer.

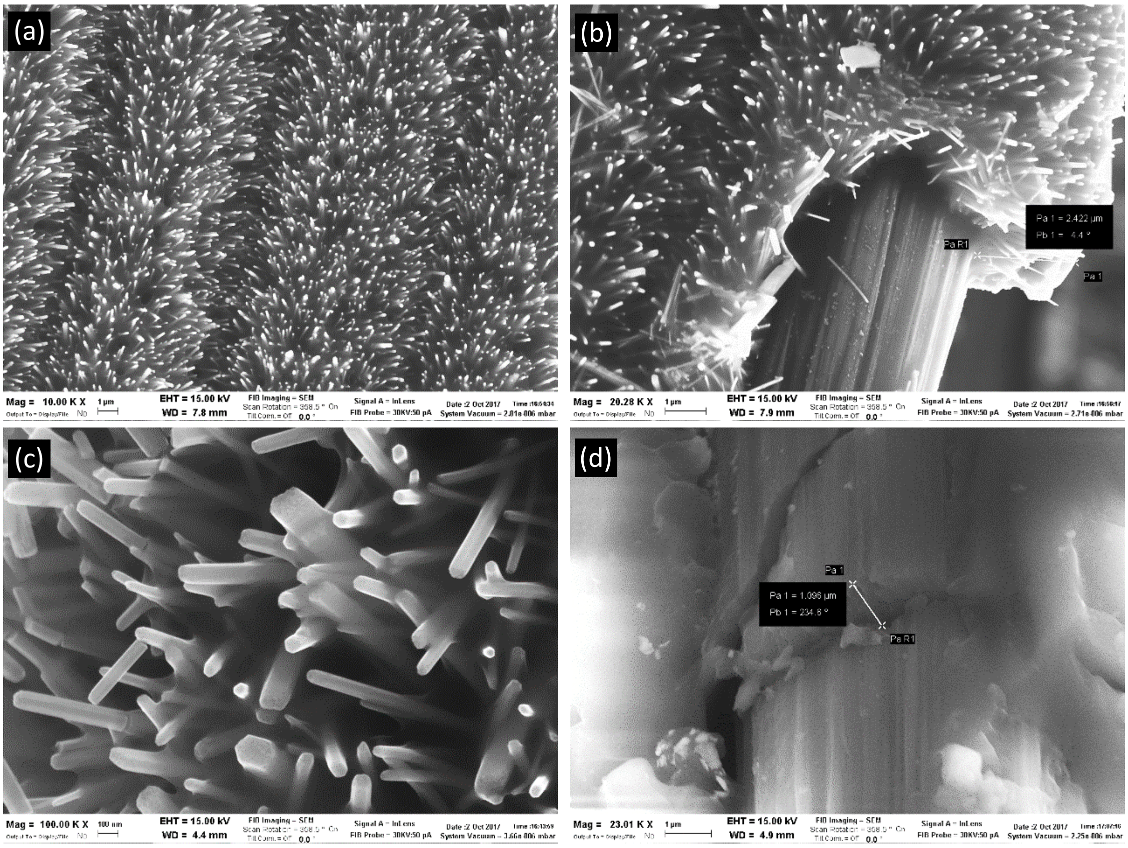

Fig. 62: (a-c) ER deposition obtained by the process explained above. The ZnO NRs are well covered and only their top extremities stick out from the polymer. (d) Two layers of ER obtained by repeating twice the deposition process on bare CF.

Nevertheless, when ER dries out, the tow/resin system becomes rigid and its thickness is much higher with respect to the one of the composite layers. With the view to overcome this problem, it is possible to insert the epoxy-covered tow between the pre-preg layers as soon as resin is deposited, so as to let ER polymerize within the composite and acquire the appropriate thickness and shape. Another issue is represented by the difference between the pre-preg resin and the one that is deposited on the tow: they must be chemically compatible, otherwise consolidation does not occurs, leading to bubbles and delamination. Experiments about electrical resistance of the epoxy systems used in this work, reveal that the volume resistivity shown in table 5 does not present linear behavior when very low thickness is reached. By approaching nanometric thickness, high resistance is not maintained and conductivity hinders the insulating purpose of the ER. Hence, a compromise must be achieved, since thickness has to be kept above the nanometric scale but it cannot exceed the amount that makes it bulky for the embedding process.

For the piezoelectric assessment of the device, mechanical and electrical features of the resin represent a crucial question as well for two main reasons:

- When a stress is applied, if the ER is softer than ZnO NRs, it will absorb mechanical forces and deform elastically, preventing the piezoelectric effect to happen.
- The dielectric constant of the epoxy system could invalidate the piezoelectric measurement. In fact, as multiple layers are present in this sensing structure, the total capacitance arising from capacitances in series is limited by the lower one. If the dielectric constant of the ER is low, its capacitance could be too low as well and impede to evaluate the piezoelectric behavior.

Both these aspects are visible in figure 63.

The latter, in particular, is revealed by adding a strong insulator between the two functionalized tows. Aluminum oxide Al_2O_3 exhibits high dielectric constant:

$$\varepsilon_R^{Al_2O_3} = 19.5$$

This value has been measured by means of the ferroelectric tester described in chapter 5.2, on a Al_2O_3 cylinder with an area of 80 mm^2 and thickness of 2.5 mm. It also exhibits very high rigidity. An Al_2O_3 cement is prepared by mixing Al_2O_3 powder with a specific glue solvent, and one drop of this paste is deposited between two ZfCF tows. The process has to be very fast since the paste dries out very quickly (less than two minutes). The sensor is then placed in oven at 120 ℃ for 2 hours because Al_2O_3 absorbs a big quantity of humidity, which has to be removed.

All of the samples where Al_2O_3 is present, show perfect electrical insulation and capacitance peaks up to ~44.9% of the initial value when stress is applied. The effect of softness is highlighted, instead, when comparing the blank measurements of both ER (figure 63/a) and Al_2O_3 (figure 63/c): in the first case a capacitance increase up to ~28.7% is displayed when pressure is applied, even in the absence of ZnO, while in the second capacitance is unaltered by stress. Figure 63/b is the piezoelectric response of a CFTs sensor immersed in ER (not in CFC). For this sample, capacitance raises by ~53% (*NB* more than half of the signal is caused by resin deformation, by subtracting the resin contribution a ~24.3% variation is obtained). Anyway, Al_2O_3 is very rigid and fragile; several attempts of embedding the ZfCF sensor with alumina within the composite have been realized. Al_2O_3 was deposited both before the embedding process (so it was already completely dry) and in conjunction with it, when alumina was still wet so it could acquire the correct shape and thickness. Despite these precautions, Al_2O_3 is usually subjected to breakage inside the composite. Moreover, its thickness is high in any case (especially due to its high viscosity during deposition process), so the problem of inserting an unwanted thick layer is still present.

Clearly, several attempts of embedding the resin-protected sensor within the CFC were made as well. As in the case of alumina, ER have been employed both in dry and wet form, but piezoelectric measurements displayed either excessively high insulation between the ZfCFs or, again, short circuits.

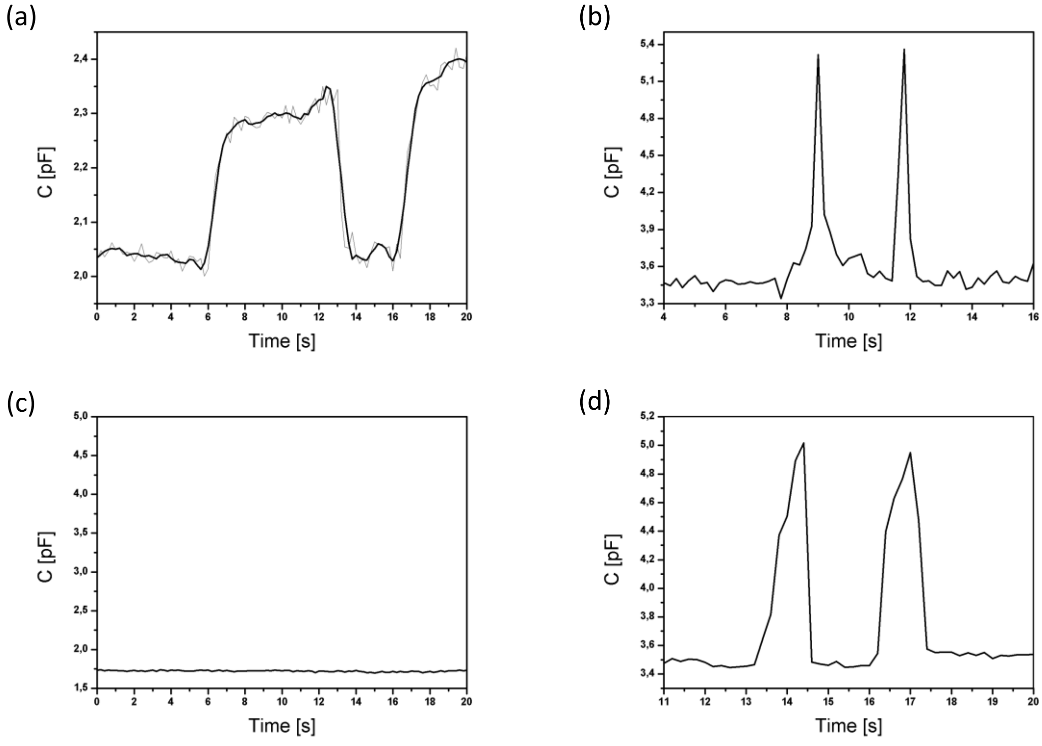

Fig. 63: (a) ER blank signal. (b) Capacitance peaks related to ZfCF tows device (more than half of the signal is caused by resin deformation). (c) Blank of the Al_2O_3 sample. (d) Capacitance peaks of the Al_2O_3 device.

Concerning the piezoelectric measurements, it is crucial to screen electrostatic and other extrinsic signals by covering the sample with aluminum tape (figure 64). The composite piece is fixed to a platform by means of screws, through which the external conductive tape is connected to ground.

Due to the aforementioned properties of the resin and the risk of electrostatic effects, the sensing properties of the device embedded within resin, shown in figure 63/b, has to be confirmed by further studies. However, the result is promising since this functioning device represents the preparatory step to the complete integration.

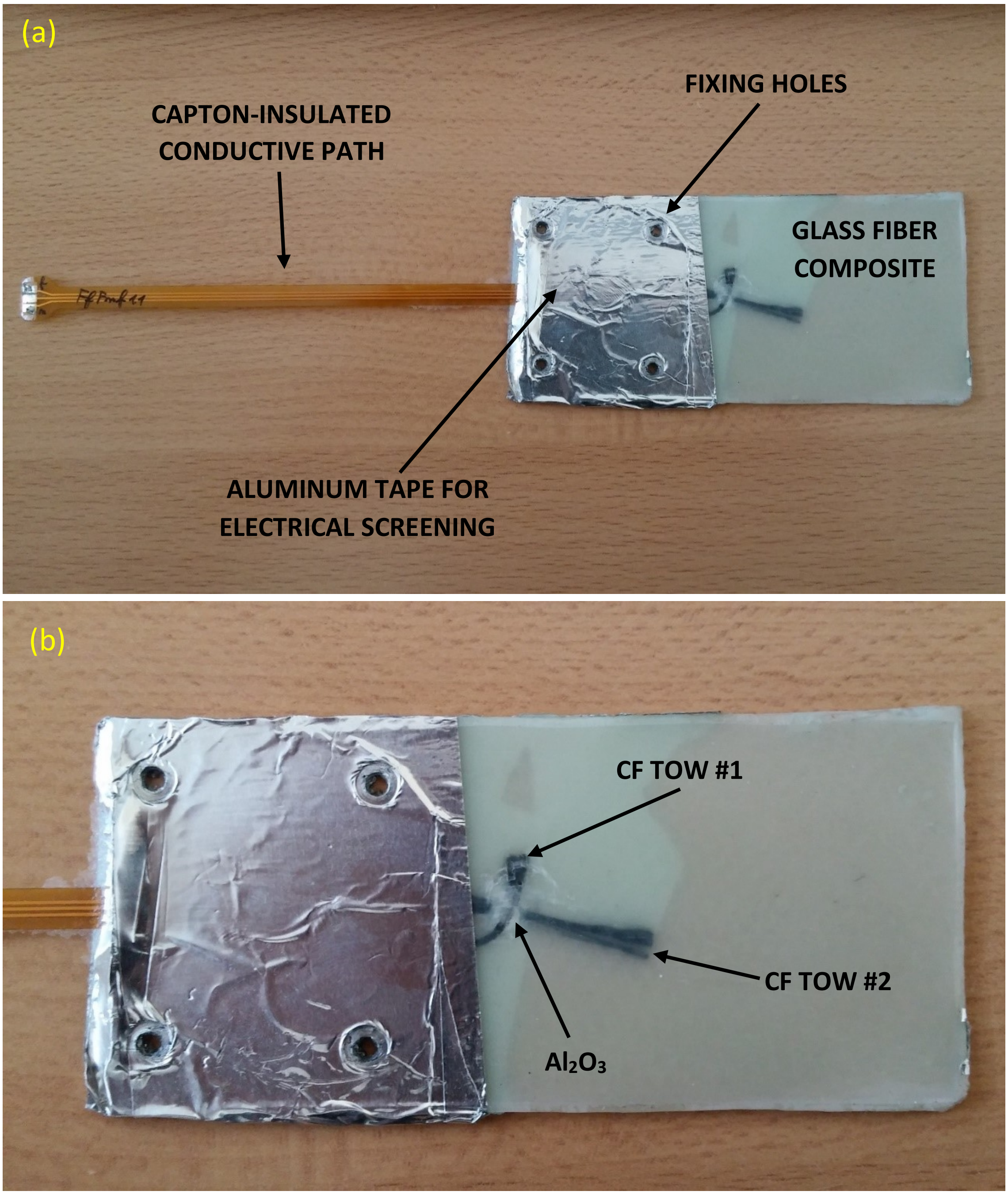

Fig. 64: (a) ZfCF sensor embedded in glass fiber composite. Part of aluminum tape is removed in order to show the underlying area. (b) Magnification of the sample. This, in particular, is one of the samples used for the tests with alumina.

10 Conclusions and perspectives

Carbon fiber composites represent a cornerstone for applications where both light weight and high-level mechanical features are requested. Their cost is still non-competitive with respect to aluminum alloys, but predictions affirm that this issue will be resolved in few decades.

For many applications where carbon fiber composites are present, these materials undergo extreme mechanical stresses; moreover, due to the manufacturing process, strongly dependent on the arrangement of carbon fiber layers in the single final objects, modelling mechanical failures is a complicated challenge. This is the most critical aspect that limits the use of carbon fiber composites, for instance, in the field of aviation. It is necessary, therefore, to analyze deformations in real time.

Deformation sensors that are employed nowadays, display important drawbacks, such as size, obstruction and presence of expensive and/or materials which are extrinsic with respect to the composite.

Owing to the relationship existing between electric signals and mechanical deformations in piezoelectric materials, piezoelectric effect is a suitable phenomenon for this type of sensing. Piezoelectric effect has the unique characteristic to work “in both directions”. Electric signals arise from mechanical deformation, but the opposite phenomenon happens as well: deformation is achieved by applying electric inputs. If a composite material includes a piezoelectric material, this can be forced to deform and the deformation can be transferred to the surrounding matrix, which is actually the entire composite. In the presence of a feedback system connected to the sensing material, it is possible, therefore, to respond to the deformation in order to hinder it simultaneously. In this case, the composite material does not only act as active sensor, but as smart material as well: it autonomously reacts to external solicitations. This is undoubtedly one of the most interesting perspectives of this technology.

ZnO is a low-cost material that is relatively easy to synthesize by means of low temperature techniques. Its anisotropic nanostructures have been intensively studied for exploitation of deformation sensing, energy harvesting and nanogenerators. Thanks to the ease of synthesis of ZnO, it is possible to functionalize carbon fibers with ZnO piezoelectric nanostructures, in order to give carbon fiber composites deformation sensing properties and, therefore, transforming them into self-sensing materials.

The functionalization is fulfilled through a two-step process: ZnO seed layer is deposited on the carbon fibers, then nanorods are grown by alkaline chemical bath deposition mediated by hexamethylenetetramine. This method is low-cost (precursors are cheap), ecologic (water is the solvent) and low-temperature (carbon fibers undergo destructive oxidation at high temperatures). It is, hence, suitable for industrialization.

Excellent control is achieved in functionalization, since it is fulfilled both on single fibers and entire tows. Furthermore, aspect ratio and surface density can be controlled as well.

Once functionalization is achieved, the sensor is built by arranging single carbon fibers or carbon fiber tows in a cross-like structure.

Piezoelectric characterization is carried out by means of ferroelectric analysis (combination of dynamic hysteresis measurement and capacitance measurement, for the direct piezoelectric effect) and piezoresponse force microscopy (for inverse piezoelectric effect). The former, in particular, shows the excellent proportionality between applied stress and piezoelectric output. By means of the latter, the value of the piezoelectric coefficient that arises is $d_{33}^{ZnO,CBD} = (4.5 \pm 0.1)\ \frac{pm}{V}$, in accordance with scientific literature.

The single-fiber sensor displays a capacitance variation of 715% with a load of $50\ g$, while in the case of the tow-based device a capacitance increase of 508% is achieved with a $30\ g$ load.

The final step for the attainment of a sensing carbon fiber composite is to embed the aforementioned sensor within the composite material. This turns out to be the most critical stage, since the manufacturing process results mechanically aggressive for the ZnO nanostructures, and the final piezoelectric assessment is made impossible by either short circuits between carbon fiber tows or excessively high insulation caused by resin.

With this in mind, a more mechanical stable device has been realized by either protecting the sensor with epoxy resin or inserting an alumina paste with high dielectric constant between the functionalized carbon fiber tows. The Al_2O_3 paste prevents short circuits and allows easier reading of the piezoelectric output arising from ZnO. Capacitance peaks up by 44.9% with a $50\ g$ load. Nevertheless, its thickness and fragility do not make it appropriate to solve the question of the presence of extrinsic and thick materials within the composite.

When epoxy resin protection is present, instead, the effect of its thickness is important and can make piezoelectric assessment difficult; indeed, the electrical resistance is dramatically reduced when thickness is low (nm scale) and resin softness becomes significant for high thickness (μm scale). In the former case, insulation between the two carbon fibers is compromised, while in the latter the elastic deformation of resin can conceal the piezoelectric effect. The study recently focused on the optimization of the resin thickness, so that both the electrical and mechanical properties of the epoxy system are balanced and does not contribute adversely.

A 24.3% variation in capacitance was obtained with a load of $50\ g$ for a carbon fiber tows sensor immersed in epoxy resin. This has to be confirmed by further studies, but despite the efforts to achieve complete integration did not produce the pursued results yet, it represents a promising preparatory step toward the complete integration.

Furthermore, with the view of the final sensing composite, it is important to underline that the mechanical features of the composite material are not worsened by the presence of ZnO.

11 Publications and dissemination

11.1 Patent

With this work, an international patent has been registered, whose data are reported in the following table.

TITLE	Zinc oxide-based piezoelectric device
CODE	WO2015145290 (A1)
DATE	Publication October 1st 2015
EXTENSION	Application to EU, USA, Japan.
INVENTORS	Calestani Davide, Coppedè Nicola, Culiolo Maurizio, Delmonte Davide, Villani Marco, Zappettini Andrea, Marchini Laura Bercella Rocco.
APPLICANTS	Bercella s.r.l., C.N.R.

Tab. 8: Data of the international patent registered during this work.

11.2 Scientific papers

- *Turning carbon fiber into a stress-sensitive composite material*, M. Villani, D. Delmonte, M. Culiolo, D. Calestani, N. Coppedè, M. Solzi, L. Marchini, R. Bercella, A. Zappettini, ***Journal of Materials Chemistry A, 2016, 4, 10486-10492***.
- *Smart composites materials: A new idea to add gas-sensing properties to commercial carbon-fibers by functionalization with ZnO nanowires*, D. Calestani, M. Villani, M. Culiolo, D. Delmonte, N. Coppedè, A. Zappettini, ***Sensors & Actuators B: Chemical, 2017, 245, 166-170***.
- *Crystal growth of nanostructured zinc oxide nanorods from the seed layer,* B. Adetoye, M. Culiolo, A. Zappettini, D. Calestani, P. Managutti, N. Coppedè, M. Villani, A. Alabi, T. Akomolafe, ***submitted***.

- *Piezoelectric sensor based on carbon fiber tows functionalized with zinc oxide NRs,* M. Culiolo, D. Delmonte, M. Villani, D. Calestani, A. Zappettini*,* **submitted**.
- *Tailoring the morphology of ZnO nanorods by chemical bath deposition*, M. Villani, M. Culiolo, D. Calestani, A. Zappettini, **submitted**.
- *Pressure sensor obtained by functionalization of commercial foam rubber with PEDOT:PSS,* M. Culiolo, N. Coppedè, A. Zappettini, **in progress**.

11.3 Conferences

- **Poster***: ZnO nanorod-based piezoelectric stress sensor embedded within carbon fiber composite,* 3rd Parma Nano-Day, Parma (Italy), July 12-14th 2017.
- **Oral***: ZnO nanorod-based piezoelectric stress sensor embedded within carbon fiber composite,* NanoMaterials for Energy and Environment (NanoMatEn2017), Paris (France), June 28-30th 2017.
- **Oral***: Carbon fibers functionalized with piezoelectric ZnO nanorods for mechanical stress sensing,* 2nd Parma Nano-Day, Parma (Italy), December 3-4th 2015.
- **Poster***: Growth of ZnO nanorods on carbon fibers for in situ stress measurements,* Fifth European Conference on Crystal Growth (ECCG5), Bologna (Italy), September 9-11th 2015.

11.4 Award

- **BEST POSTER** for *"ZnO nanorod-based piezoelectric stress sensor embedded within carbon fiber composite"* at the Session A "Technologies, Chemistry and Physics" of the 3rd Parma Nano-Day, Parma (Italy), July 12-14th 2017.

12 References

[1] https://www.thoughtco.com/applications-of-carbon-fiber-820384.

[2] http://www.dmfci.unict.it/siracusa/web1/materiale_didattico/c5.pdf.

[3] http://www.dexcraft.com/articles/carbon-fiber-composites/aluminium-vs-carbon-fiber-comparison-of-materials/.

[4] R. Heuss, N. Müller, S. A. Sintern Wv e A. Tschiesner, *Lightweight, heavy impact. McKinsey & Company,* 2012.

[5] U. S. G. A. Office, «Status of FAA's Actions to Oversee the Safety of Composite Airplanes,» 2011.

[6] Y. Zhu, Y. Gui, S. Rong e Z. Hong, «A Review of Optical NDT Technologies,» *Sensors,* vol. 11, p. 7773–7798, 2012.

[7] G. Sala, L. Di Landro, A. Airoldi e P. Bettini, «Tecnologie e materiali aerospaziali,» *Politecnico di Milano, Milano.*

[8] W. K. B. G. R. H. J. W. Wilkie, «Low-Cost Piezocomposite Actuator for Structural Control Applications, SPIE 7th Annual International Symposium on Smart Structures and Materials,» Newport Beach, CA, 2000.

[9] S. S. a. A. Erturk, «Electrohydroelastic Euler–Bernoulli–Morison model for underwater resonant actuation of macro-fiber composite piezoelectric cantilevers,» *Smart Materials and Structures,* vol. 25, p. 105007, 2016.

[10] A. B. F. Felli, «Impiego di sensori in fibra ottica per il monitoraggio di fratture statiche e dinamiche», 2010.

[11] M. Ramakrishnan, G. Rajan, Y. Semenova e G. Farrell, «Overview of fiber optic sensor technologies for strain/temperature sensing applications in composite materials,» *Sensors,* vol. 16, p. 99, 2016.

[12] M. Borotto, E. De Cais, «Progettazione e realizzazione di una struttura dinamometrica in materiale composito basata su sensori a fibra ottica,» 2010.

[13] G. Luyckx, E. Voet, N. Lammens e J. Degrieck, «Strain measurements of composite laminates with embedded fibre Bragg gratings: Criticism and opportunities for research,» *Sensors,* vol. 11, pp. 384-408, 2010.

[14] «Strutture ibride per la meccanica e l'aerospazio». *Composite materials presses.*

[15] C. W. Bunn, «A comparative review of ZnO materials and devices,» in *Proc. Phys. Soc., London*, 1935.

[16] C. A. Mead, «Surface barriers on ZnSe and ZnO,» *Physics Letters,* vol. 18, p. 218, 1965.

[17] T. C. Damen, S. P. S. Porto e B. Tell, «Raman effect in zinc oxide,» *Physical Review,* vol. 142, p. 570, 1966.

[18] E. Mollwo, *Z. angew Phys,* vol. 6, p. 257, 1954.

[19] I. T. Drapak, *Visible luminescence of a ZnO-Cu2O heterojunction,* vol. 2, Amer Inst Physics Circulation Fulfillment Div, 500 Sunnyside Blvd, Woodbury, NY 11797-2999, 1968, p. 513.

[20] J. L. Gomez e O. Tigli, «Zinc oxide nanostructures: from growth to application,» *Journal of Materials Science,* vol. 48, pp. 612-624, 2013.

[21] V. A. L. Roy, A. B. Djurišić, W. K. Chan, J. Gao, H. F. Lui e C. Surya, «Luminescent and structural properties of ZnO nanorods prepared under different conditions,» *Applied physics letters,* vol. 83, pp. 141-143, 2003.

[22] C. Maragliano, S. Lilliu, M. S. Dahlem, M. Chiesa, T. Souier e M. Stefancich, «Quantifying charge carrier concentration in ZnO thin films by Scanning Kelvin Probe Microscopy,» *Scientific reports,* vol. 4, 2014.

[23] D. C. Look, D. C. Reynolds, J. R. Sizelove, R. L. Jones, C. W. Litton, G. Cantwell e W. C. Harsch, «Electrical properties of bulk ZnO,» *Solid state communications,* vol. 105, pp. 399-401, 1998.

[24] A. J. a. C. G. V. d. Walle, «Fundamentals of zinc oxide as a semiconductor,» *Rep. Prog. Phys.,* vol. 72, p. 126501, 2009.

[25] A. H. F. L. H. Z. F. H. a. B. K. M. Detlev M. Hofmann, «Hydrogen: A Relevant Shallow Donor in Zinc Oxide,» *PHYSICAL REVIEW LETTERS,* vol. 88, n. 4, p. 045504, 2002.

[26] C. G. Van de Walle, «Hydrogen as a cause of doping in zinc oxide,» *Physical review letters,* vol. 85, p. 1012, 2000.

[27] A. Janotti e C. G. Van de Walle, «Hydrogen multicentre bonds,» *Nature materials,* vol. 6, p. nmat1795, 2006.

[28] W. Setyawan e S. Curtarolo, «High-throughput electronic band structure calculations: Challenges and tools,» *Computational Materials Science,* vol. 49, pp. 299-312, 2010.

[29] A. B. Djurišić, X. Chen, Y. H. Leung e A. M. C. Ng, «ZnO nanostructures: growth, properties and applications,» *Journal of Materials Chemistry,* vol. 22, pp. 6526-6535, 2012.

[30] A. Janotti e C. G. Van de Walle, «Oxygen vacancies in ZnO,» *Applied Physics Letters,* vol. 87, p. 122102, 2005.

[31] A. Janotti e C. G. Van de Walle, «New insights into the role of native point defects in ZnO,» *Journal of Crystal Growth,* vol. 287, pp. 58-65, 2006.

[32] A. J. a. C. G. V. d. Walle, «Native point defects in ZnO,» *Phys. Rev. B,* vol. 76, p. 165202, 2007.

[33] S. Limpijumnong, S. B. Zhang, S.-H. Wei e C. H. Park, «Doping by large-size-mismatched impurities: the microscopic origin of arsenic-or antimony-doped p-type zinc oxide,» *Physical review letters,* vol. 92, p. 155504, 2004.

[34] C. H. Park, S. B. Zhang e S.-H. Wei, «Origin of p-type doping difficulty in ZnO: The impurity perspective,» *Physical Review B,* vol. 66, p. 073202, 2002.

[35] Y. Q. Fu, J. K. Luo, X. Y. Du, A. J. Flewitt, Y. Li, G. H. Markx, A. J. Walton e W. I. Milne, «Recent developments on ZnO films for acoustic wave based bio-sensing and microfluidic applications: a review,» *Sensors and Actuators B: Chemical,* vol. 143, pp. 606-619, 2010.

[36] http://tcqp.science/18-pages/projects/inactive/26-environmentally-sensitive-equilibrium-morphology-phase-mapping-of-nanoparticles-nanorods,.

[37] M. Hadis e Ö. Ümit, *Zinc Oxide: Fundamentals, Materials and Device Technology,* WILEY-VCH Verlag GmbH & Co. KGaA, Weinheim, 2009.

[38] http://nptel.ac.in/courses/113104005/lecture_pdf/module5.pdf.

[39] Z. L. Wang, «Nanostructures of zinc oxide,» *Materials today,* vol. 7, pp. 26-33, 2004.

[40] T. V. Richter, F. Stelzl, J. Schulz-Gericke, B. Kerscher, U. Würfel, M. Niggemann e S. Ludwigs, «Room temperature vacuum-induced ligand removal and patterning of ZnO nanoparticles: from semiconducting films towards printed electronics,» *Journal of Materials Chemistry,* vol. 20, pp. 874-879, 2010.

[41] X. L. Yuan, B. P. Zhang, J. Niitsuma e T. Sekiguchi, «Cathodoluminescence characterization of ZnO nanotubes grown by MOCVD on sapphire substrate,» *Materials science in semiconductor processing,* vol. 9, pp. 146-150, 2006.

[42] Y. B. G. S. a. D. G. Changhui Ye, «Thickness-Dependent Photocatalytic Performance of ZnO Nanoplatelets,» *J. Phys. Chem. B,* vol. 110 (31), p. 15146–15151, 2006.

[43] X. H. J. D. H. A. P. T. Jinping Liu, *Materials Letters,* vol. 59, pp. 3710-3714, 2005.

[44] Z. D. J. L. L. X. W. Y. Y. Q. Qin Xie, *Solid State Communications,* vol. 136, pp. 304-307, 2005.

[45] Z. R. D. Z. L. W. Zheng Wei Pan, «Nanobelts of Semiconducting Oxides,» *Science,* vol. 291, p. 1947, 2001.

[46] Z. L. Wang, «Zinc oxide nanostructures: growth, properties and applications,» *Journal of Physics: Condensed Matter,* vol. 16, p. R829, 2004.

[47] X. Y. Kong e Z. L. Wang, «Spontaneous polarization-induced nanohelixes, nanosprings, and nanorings of piezoelectric nanobelts,» *Nano Letters,* vol. 3, pp. 1625-1631, 2003.

[48] X. Y. Kong, Y. Ding, R. Yang e Z. L. Wang, «Single-crystal nanorings formed by epitaxial self-coiling of polar nanobelts,» *Science,* vol. 303, pp. 1348-1351, 2004.

[49] Z. L. Wang, X. Y. Kong e J. M. Zuo, «Induced growth of asymmetric nanocantilever arrays on polar surfaces,» *Physical Review Letters,* vol. 91, p. 185502, 2003.

[50] P. Gao e Z. L. Wang, «Self-assembled nanowire- nanoribbon junction arrays of ZnO,» *The journal of physical chemistry B,* vol. 106, pp. 12653-12658, 2002.

[51] R. Helbig, «Über die züchtung von grösseren reinen und dotierten ZnO-kristallen aus der gasphase,» *Journal of Crystal Growth,* vol. 15, pp. 25-31, 1972.

[52] J.-L. Santailler, C. Audoin, G. Chichignoud, R. Obrecht, B. Kaouache, P. Marotel, D. Pelenc, S. Brochen, J. Merlin, I. Bisotto e others, «Chemically assisted vapour transport for bulk ZnO crystal growth,» *Journal of Crystal Growth,* vol. 312, pp. 3417-3424, 2010.

[53] E. Ohshima, H. Ogino, I. Niikura, K. Maeda, M. Sato, M. Ito e T. Fukuda, «Growth of the 2-in-size bulk ZnO single crystals by the hydrothermal method,» *Journal of Crystal Growth,* vol. 260, pp. 166-170, 2004.

[54] J. Nause e B. Nemeth, «Pressurized melt growth of ZnO boules,» *Semiconductor Science and Technology,* vol. 20, p. S45, 2005.

[55] A. O. Dikovska, P. A. Atanasov, C. Vasilev, I. G. Dimitrov e T. R. Stoyanchov, «Thin ZnO films produced by pulsed laser deposition,» *J. Optoelectron. Adv. Mater.,* vol. 7, pp. 1329-1334, 2005.

[56] K. S. T. S. W. Z. a. K. S. Zhuo Chen, «ZnO thin films synthesized by chemical vapor deposition,» in *Applications and Technology Conference (LISAT), 2010 Long Island Systems*, Farmingdale, NY, USA, 2010.

[57] C. Munuera, J. Zuniga-Perez, J. F. Rommeluere, V. Sallet, R. Triboulet, F. Soria, V. Munoz-Sanjose e C. Ocal, «Morphology of ZnO grown by MOCVD on sapphire substrates,» *Journal of crystal growth,* vol. 264, pp. 70-78, 2004.

[58] M. A. L. Johnson, S. Fujita, W. H. Rowland, W. C. Hughes, J. W. Cook e J. F. Schetzina, «MBE growth and properties of ZnO on sapphire and SiC substrates,» *Journal of Electronic Materials,* vol. 25, pp. 855-862, 1996.

[59] R. Ondo-Ndong, G. Ferblantier, M. Al Kalfioui, A. Boyer e A. Foucaran, «Properties of RF magnetron sputtered zinc oxide thin films,» *Journal of Crystal Growth,* vol. 255, pp. 130-135, 2003.

[60] Y. W. Heo, D. P. Norton e S. J. Pearton, «Origin of green luminescence in ZnO thin film grown by molecular-beam epitaxy,» *Journal of Applied Physics,* vol. 98, p. 073502, 2005.

[61] A. K.-R. a. T. Jesionowski, «Zinc Oxide—From Synthesis to Application: A Review,» *Materials,* vol. 7, pp. 2833-2881, 2014.

[62] S. Mahmud, M. Johar Abdullah, G. A. Putrus, J. Chong e A. Karim Mohamad, «Nanostructure of ZnO fabricated via French process and its correlation to electrical properties of semiconducting varistors,» *Synthesis and Reactivity in Inorganic and Metal-Organic and Nano-Metal Chemistry,* vol. 36, pp. 155-159, 2006.

[63] W. Ao, J. Li, H. Yang, X. Zeng e X. Ma, «Mechanochemical synthesis of zinc oxide nanocrystalline,» *Powder Technology,* vol. 168, pp. 148-151, 2006.

[64] A. Kołodziejczak-Radzimska, T. Jesionowski e A. Krysztafkiewicz, «Obtaining zinc oxide from aqueous solutions of KOH and Zn $(CH_3COO)_2$,» *Physicochemical Problems of Mineral Processing,* vol. 44, pp. 93-102, 2010.

[65] R. Hong, T. Pan, J. Qian e H. Li, «Synthesis and surface modification of ZnO nanoparticles,» *Chemical Engineering Journal,* vol. 119, pp. 71-81, 2006.

[66] A. S. Lanje, S. J. Sharma, R. S. Ningthoujam, J.-S. Ahn e R. B. Pode, «Low temperature dielectric studies of zinc oxide (ZnO) nanoparticles prepared by precipitation method,» *Advanced Powder Technology,* vol. 24, pp. 331-335, 2013.

[67] Y. Wang, C. Zhang, S. Bi e G. Luo, «Preparation of ZnO nanoparticles using the direct precipitation method in a membrane dispersion micro-structured reactor,» *Powder Technology,* vol. 202, pp. 130-136, 2010.

[68] W. Jia, S. Dang, H. Liu, Z. Zhang, C. Yu, X. Liu e B. Xu, «Evidence of the formation mechanism of ZnO in aqueous solution,» *Materials Letters,* vol. 82, pp. 99-101, 2012.

[69] C.-l. Ma, X.-d. Sun e others, «Preparation of nanocrystalline metal oxide powders with the surfactant-mediated method,» *Inorganic Chemistry Communications,* vol. 5, pp. 751-755, 2002.

[70] P. Li, Y. Wei, H. Liu e X.-k. Wang, «Growth of well-defined ZnO microparticles with additives from aqueous solution,» *Journal of solid state chemistry,* vol. 178, pp. 855-860, 2005.

[71] L. Znaidi, «Sol--gel-deposited ZnO thin films: A review,» *Materials Science and Engineering: B,* vol. 174, pp. 18-30, 2010.

[72] H. Benhebal, M. Chaib, T. Salmon, J. Geens, A. Leonard, S. D. Lambert, M. Crine e B. Heinrichs, «Photocatalytic degradation of phenol and benzoic acid using zinc oxide powders prepared by the sol--gel process,» *Alexandria Engineering Journal,* vol. 52, pp. 517-523, 2013.

[73] M. Ristić, S. Musić, M. Ivanda e S. Popović, «Sol--gel synthesis and characterization of nanocrystalline ZnO powders,» *Journal of Alloys and Compounds,* vol. 397, pp. L1--L4, 2005.

[74] S. Yue, Z. Yan, Y. Shi e G. Ran, «Synthesis of zinc oxide nanotubes within ultrathin anodic aluminum oxide membrane by sol--gel method,» *Materials Letters,* vol. 98, pp. 246-249, 2013.

[75] D. Chen, X. Jiao e G. Cheng, «Hydrothermal synthesis of zinc oxide powders with different morphologies,» *Solid State Communications,* vol. 113, pp. 363-366, 1999.

[76] A. A. Ismail, A. El-Midany, E. A. Abdel-Aal e H. El-Shall, «Application of statistical design to optimize the preparation of ZnO nanoparticles via hydrothermal technique,» *Materials Letters,* vol. 59, pp. 1924-1928, 2005.

[77] L. N. Demianets, L. E. Li e T. G. Uvarova, «Zinc oxide: hydrothermal growth of nano-and bulk crystals and their luminescent properties,» *Journal of materials science,* vol. 41, pp. 1439-1444, 2006.

[78] X.-L. Hu, Y.-J. Zhu e S.-W. Wang, «Sonochemical and microwave-assisted synthesis of linked single-crystalline ZnO rods,» *Materials Chemistry and physics,* vol. 88, pp. 421-426, 2004.

[79] T. Strachowski, E. Grzanka, B. F. Palosz, A. Presz, L. Ślusarski e W. Łojkowski, «Microwave driven hydrothermal synthesis of zinc oxide nanopowders,» in *Solid State Phenomena*, 2003.

[80] T. Choduba, W. Łojkowski, E. Reszke e T. Strachowski, «Way of Conducting of Synthesis and Chemical Electrode Reactor,» *US3450617 A,* vol. 28, 2009.

[81] J. J. Schneider, R. C. Hoffmann, J. Engstler, A. Klyszcz, E. Erdem, P. Jakes, R.-A. Eichel, L. Pitta-Bauermann e J. Bill, «Synthesis, characterization, defect chemistry, and FET properties of microwave-derived nanoscaled zinc oxide,» *Chemistry of Materials,* vol. 22, pp. 2203-2212, 2010.

[82] J. Zhang, J. Wang, S. Zhou, K. Duan, B. Feng, J. Weng, H. Tang e P. Wu, «Ionic liquid-controlled synthesis of ZnO microspheres,» *Journal of Materials Chemistry,* vol. 20, pp. 9798-9804, 2010.

[83] S.-J. Chen, L.-H. Li, X.-T. Chen, Z. Xue, J.-M. Hong e X.-Z. You, «Preparation and characterization of nanocrystalline zinc oxide by a novel solvothermal oxidation route,» *Journal of Crystal Growth,* vol. 252, pp. 184-189, 2003.

[84] X. Li, G. He, G. Xiao, H. Liu e M. Wang, «Synthesis and morphology control of ZnO nanostructures in microemulsions,» *Journal of Colloid and Interface Science,* vol. 333, pp. 465-473, 2009.

[85] S. A. Vorobyova, A. I. Lesnikovich e V. V. Mushinskii, «Interphase synthesis and characterization of zinc oxide,» *Materials Letters,* vol. 58, pp. 863-866, 2004.

[86] C.-H. Lu e C.-H. Yeh, «Emulsion precipitation of submicron zinc oxide powder,» *Materials Letters,* vol. 33, pp. 129-132, 1997.

[87] A. Kołodziejczak-Radzimska, E. Markiewicz e T. Jesionowski, «Structural characterisation of ZnO particles obtained by the emulsion precipitation method,» *Journal of Nanomaterials,* vol. 2012, p. 15, 2012.

[88] M. Singhai, V. Chhabra, P. Kang e D. O. Shah, «Synthesis of ZnO nanoparticles for varistor application using Zn-substituted aerosol OT microemulsion,» *Materials Research Bulletin,* vol. 32, pp. 239-247, 1997.

[89] A. Yıldırım e C. Durucan, «Synthesis of zinc oxide nanoparticles elaborated by microemulsion method,» *Journal of Alloys and Compounds,* vol. 506, pp. 944-949, 2010.

[90] J. Xu, Q. Pan, Z. Tian e others, «Grain size control and gas sensing properties of ZnO gas sensor,» *Sensors and Actuators B: Chemical,* vol. 66, pp. 277-279, 2000.

[91] K. Okuyama e I. W. Lenggoro, «Preparation of nanoparticles via spray route,» *Chemical engineering science,* vol. 58, pp. 537-547, 2003.

[92] T. Tani, L. Mädler e S. E. Pratsinis, «Homogeneous ZnO nanoparticles by flame spray pyrolysis,» *Journal of Nanoparticle Research,* vol. 4, pp. 337-343, 2002.

[93] X. Zhao, B. Zheng, C. Li e H. Gu, «Acetate-derived ZnO ultrafine particles synthesized by spray pyrolysis,» *Powder Technology,* vol. 100, pp. 20-23, 1998.

[94] E. Kärber, T. Raadik, T. Dedova, J. Krustok, A. Mere, V. Mikli e M. Krunks, «Photoluminescence of spray pyrolysis deposited ZnO nanorods,» *Nanoscale research letters,* vol. 6, p. 359, 2011.

[95] T. Han, A. L. Yarin e D. H. Reneker, «Viscoelastic electrospun jets: Initial stresses and elongational rheometry,» *Polymer,* vol. 49, pp. 1651-1658, 2008.

[96] L. Zanotti, D. Calestani, M. Villani, M. Zha, A. Zappettini e C. Paorici, «Vapour-phase growth, purification and large-area deposition of ZnO tetrapod nanostructures,» *Crystal Research and Technology,* vol. 45, pp. 667-671, 2010.

[97] D. Calestani, M. Zha, R. Mosca, A. Zappettini, M. C. Carotta, V. Di Natale e L. Zanotti, «Growth of ZnO tetrapods for nanostructure-based gas sensors,» *Sensors and Actuators B: Chemical,* vol. 144, pp. 472-478, 2010.

[98] R. S. Wagner e W. C. Ellis, «Vapor-liquid-solid mechanism of single crystal growth,» *Applied Physics Letters,* vol. 4, pp. 89-90, 1964.

[99] M. H. Huang, Y. Wu, H. Feick, N. Tran, E. Weber e P. Yang, «Catalytic growth of zinc oxide nanowires by vapor transport,» *Advanced Materials,* vol. 13, pp. 113-116, 2001.

[100] H. Simon, T. Krekeler, G. Schaan e W. Mader, «Metal-seeded growth mechanism of ZnO nanowires,» *Crystal Growth \& Design,* vol. 13, pp. 572-580, 2013.

[101] P. X. Gao, Y. Ding e Z. L. Wang, «Crystallographic orientation-aligned ZnO nanorods grown by a tin catalyst,» *Nano Letters,* vol. 3, pp. 1315-1320, 2003.

[102] http://www.everzinc.com/zinc-oxide/market-and-applications/.

[103] http://www.lifegreenzo.eu/?page_id=1021&lang=en.

[104] D. C. Reynolds, D. C. Look e B. Jogai, «Optically pumped ultraviolet lasing from ZnO,» *Solid State Communications,* vol. 99, pp. 873-875, 1996.

[105] Y. I. A. C. L. A. T. M. A. R. S. D. V. A. S.-J. C. a. H. M. Ü. Özgür, «A comprehensive review of ZnO materials and devices,» *J. Appl. Phys.,* vol. 98, p. 041301, 2005.

[106] A. Mang, K. Reimann e others, «Band gaps, crystal-field splitting, spin-orbit coupling, and exciton binding energies in ZnO under hydrostatic pressure,» *Solid state communications,* vol. 94, pp. 251-254, 1995.

[107] A. Ohtomo, M. Kawasaki, T. Koida, K. Masubuchi, H. Koinuma, Y. Sakurai, Y. Yoshida, T. Yasuda e Y. Segawa, «Mg x Zn 1- x O as a II--VI widegap semiconductor alloy,» *Applied physics letters,* vol. 72, pp. 2466-2468, 1998.

[108] F. Wang, Z. Ye, D. Ma, L. Zhu e F. Zhuge, «Formation of quasi-aligned ZnCdO nanorods and nanoneedles,» *Journal of crystal growth,* vol. 283, pp. 373-377, 2005.

[109] S. Shionoya, W. M. Yen e H. Yamamoto, Phosphor handbook, CRC press, 2006.

[110] H. Nanto, H. Sokooshi e T. Usuda, «Smell sensor using zinc oxide thin films prepared by magnetron sputtering,» in *Solid-State Sensors and Actuators, 1991. Digest of Technical Papers, TRANSDUCERS'91., 1991 International Conference on*, 1991.

[111] K. Eda, «Zinc oxide varistors,» *IEEE Electrical Insulation Magazine,* vol. 5, pp. 28-30, 1989.

[112] M. C. Larciprete, D. Haertle, A. Belardini, M. Bertolotti, F. Sarto e P. Günter, «Characterization of second and third order optical nonlinearities of ZnO sputtered films,» *Applied Physics B: Lasers and Optics,* vol. 82, pp. 431-437, 2006.

[113] J. Briscoe e S. Dunn, «Piezoelectric nanogenerators--a review of nanostructured piezoelectric energy harvesters,» *Nano Energy,* vol. 14, pp. 15-29, 2015.

[114] Z. L. Wang e J. Song, «Piezoelectric nanogenerators based on zinc oxide nanowire arrays,» *Science,* vol. 312, pp. 242-246, 2006.

[115] M. Alexe, S. Senz, M. A. Schubert, D. Hesse e U. Gösele, «Energy harvesting using nanowires?,» *Advanced Materials,* vol. 20, pp. 4021-4026, 2008.

[116] Z. L. Wang, «Energy Harvesting Using Piezoelectric Nanowires--A Correspondence on "Energy Harvesting Using Nanowires?" by Alexe et al.,» *Advanced Materials,* vol. 21, pp. 1311-1315, 2009.

[117] X. Wang, J. Song, J. Liu e Z. L. Wang, «Direct-current nanogenerator driven by ultrasonic waves,» *Science,* vol. 316, pp. 102-105, 2007.

[118] A. Asthana, H. A. Ardakani, Y. K. Yap e R. S. Yassar, «Real time observation of mechanically triggered piezoelectric current in individual ZnO nanobelts,» *Journal of Materials Chemistry C,* vol. 2, pp. 3995-4004, 2014.

[119] S. M. Hatch, J. Briscoe e S. Dunn, «A Self-Powered ZnO-Nanorod/CuSCN UV Photodetector Exhibiting Rapid Response,» *Advanced Materials,* vol. 25, pp. 867-871, 2013.

[120] J. Briscoe, N. Jalali, P. Woolliams, M. Stewart, P. M. Weaver, M. Cain e S. Dunn, «Measurement techniques for piezoelectric nanogenerators,» *Energy \& Environmental Science,* vol. 6, pp. 3035-3045, 2013.

[121] S. Dunn, «Strain behavior of thin film PbZr 0.3 Ti 0.7 O 3 (30/70) examined through piezoforce microscopy,» *Journal of applied physics,* vol. 94, pp. 5964-5968, 2003.

[122] J. Liu, P. Fei, J. Song, X. Wang, C. Lao, R. Tummala e Z. L. Wang, «Carrier density and Schottky barrier on the performance of DC nanogenerator,» *Nano letters,* vol. 8, pp. 328-332, 2008.

[123] X. W. a. Z. L. W. Chen Xu, «Nanowire Structured Hybrid Cell for Concurrently Scavenging Solar and Mechanical Energies,» *J. AM. CHEM. SOC.,* vol. 131, pp. 5866-5872, 2009.

[124] G. Zhu, A. C. Wang, Y. Liu, Y. Zhou e Z. L. Wang, «Functional electrical stimulation by nanogenerator with 58 V output voltage,» *Nano letters,* vol. 12, pp. 3086-3090, 2012.

[125] B. Saravanakumar, R. Mohan, K. Thiyagarajan e S.-J. Kim, «Fabrication of a ZnO nanogenerator for eco-friendly biomechanical energy harvesting,» *RSC Adv.,* vol. 3, n. 37, pp. 16646-16656, 2013.

[126] M.-Y. Choi, D. Choi, M.-J. Jin, I. Kim, S.-H. Kim, J.-Y. Choi, S. Y. Lee, J. M. Kim e S.-W. Kim, «Mechanically powered transparent flexible charge-generating nanodevices with piezoelectric ZnO nanorods,» *Advanced Materials,* vol. 21, pp. 2185-2189, 2009.

[127] C. Dagdeviren, Z. Li e Z. L. Wang, «Energy harvesting from the animal/human body for self-powered electronics,» *Annual Review of Biomedical Engineering,* vol. 19, 2017.

[128] S. Lee, S.-H. Bae, L. Lin, Y. Yang, C. Park, S.-W. Kim, S. N. Cha, H. Kim, Y. J. Park e Z. L. Wang, «Super-flexible nanogenerator for energy harvesting from gentle wind and as an active deformation sensor,» *Advanced Functional Materials,* vol. 23, pp. 2445-2449, 2013.

[129] B. K. a. S.-W. Kim, «Energy harvesting based on semiconducting piezoelectric ZnO nanostructures,» *Nano Energy,* vol. 1, pp. 342-355, 2012.

[130] L. S. ,. Q. L. ,. S. C. ,. F. W. ,. a. X.-M. T. Wei Zeng, «Fiber-Based Wearable Electronics: A Review of Materials, Fabrication, Devices, and Applications,» *Adv. Mater.,* vol. 26, pp. 5310-5336, 2014.

[131] H. Kim, S. M. Kim, H. Son, H. Kim, B. Park, J. Ku, J. I. Sohn, K. Im, J. E. Jang, J.-J. Park e others, «Enhancement of piezoelectricity via electrostatic effects on a textile platform,» *Energy \& Environmental Science,* vol. 5, pp. 8932-8936, 2012.

[132] Y. Qin, X. Wang e Z. L. Wang, «Microfibre--nanowire hybrid structure for energy scavenging,» *Nature,* vol. 451, pp. 809-813, 2008.

[133] Y. Hu, Y. Zhang, C. Xu, L. Lin, R. L. Snyder e Z. L. Wang, «Self-powered system with wireless data transmission,» *Nano letters,* vol. 11, pp. 2572-2577, 2011.

[134] L. Lin, Y. Hu, C. Xu, Y. Zhang, R. Zhang, X. Wen e Z. L. Wang, «Transparent flexible nanogenerator as self-powered sensor for transportation monitoring,» *Nano Energy,* vol. 2, pp. 75-81, 2013.

[135] J. Song, X. Wang, J. Liu, H. Liu, Y. Li e Z. L. Wang, «Piezoelectric potential output from ZnO nanowire functionalized with p-type oligomer,» *Nano letters,* vol. 8, pp. 203-207, 2008.

[136] J. Briscoe, M. Stewart, M. Vopson, M. Cain, P. M. Weaver e S. Dunn, «Nanostructured p-n Junctions for Kinetic-to-Electrical Energy Conversion,» *Advanced Energy Materials,* vol. 2, pp. 1261-1268, 2012.

[137] G. Zhu, R. Yang, S. Wang e Z. L. Wang, «Flexible high-output nanogenerator based on lateral ZnO nanowire array,» *Nano letters,* vol. 10, pp. 3151-3155, 2010.

[138] S. Xu, Y. Qin, C. Xu, Y. Wei, R. Yang e Z. L. Wang, «Self-powered nanowire devices,» *Nature nanotechnology,* vol. 5, pp. 366-373, 2010.

[139] G. Hodes, Chemical solution deposition of semiconductor films, CRC press, 2002.

[140] J. W. Mullin, Crystallization, Butterworth-Heinemann, 2001.

[141] M. Volmer e A. Weber, «Keimbildung in übersättigten Gebilden,» *Zeitschrift für physikalische Chemie,* vol. 119, pp. 277-301, 1926.

[142] J. Park, J. Joo, S. G. Kwon, Y. Jang e T. Hyeon, «Synthesis of monodisperse spherical nanocrystals,» *Angewandte Chemie International Edition,* vol. 46, pp. 4630-4660, 2007.

[143] D. V. Ragone, «Thermodynamics of Materials, Volume 1,» *Thermodynamics of Materials, Volume 1, by David V. Ragone, pp. 336. ISBN 0-471-30885-4. Wiley-VCH, October 1994.,* p. 336, 1994.

[144] D. A. Porter e K. E. Easterling, *Phase Transformations in Metals and Alloys, 1981 Van Nostrand Reinhold,* UK, 1981.

[145] J. Baumgartner, A. Dey, P. H. H. Bomans, C. Le Coadou, P. Fratzl, N. A. J. M. Sommerdijk e D. Faivre, «Nucleation and growth of magnetite from solution,» *Nature materials,* vol. 12, pp. 310-314, 2013.

[146] A. F. Wallace, L. O. Hedges, A. Fernandez-Martinez, P. Raiteri, J. D. Gale, G. A. Waychunas, S. Whitelam, J. F. Banfield e J. J. De Yoreo, «Microscopic evidence for liquid-liquid separation in supersaturated CaCO3 solutions,» *Science,* vol. 341, pp. 885-889, 2013.

[147] M. H. Nielsen, S. Aloni e J. J. De Yoreo, «In situ TEM imaging of CaCO3 nucleation reveals coexistence of direct and indirect pathways,» *Science,* vol. 345, pp. 1158-1162, 2014.

[148] D. Gebauer, A. Völkel e H. Cölfen, «Stable prenucleation calcium carbonate clusters,» *Science,* vol. 322, pp. 1819-1822, 2008.

[149] A. S. Myerson e B. L. Trout, «Nucleation from solution,» *Science,* vol. 341, pp. 855-856, 2013.

[150] M. Sleutel e A. E. S. Van Driessche, «Role of clusters in nonclassical nucleation and growth of protein crystals,» *Proceedings of the National Academy of Sciences,* vol. 111, pp. E546--E553, 2014.

[151] Y. F. Nicolau, «Solution deposition of thin solid compound films by a successive ionic-layer adsorption and reaction process,» *Applications of Surface Science,* vol. 22, pp. 1061-1074, 1985.

[152] S. Lindroos e M. Leskelä, «Successive ionic layer adsorption and reaction (SILAR) and related sequential solution-phase deposition techniques,» *Solution Processing of Inorganic Materials,* p. 239, 2008.

[153] V. K. LaMer e R. H. Dinegar, «Theory, production and mechanism of formation of monodispersed hydrosols,» *Journal of the American Chemical Society,* vol. 72, pp. 4847-4854, 1950.

[154] M. Villani, *Functionalization of zinc oxide nanostructures,* Università degli Studi di Parma - IMEM-CNR, 2012.

[155] J. H. L. Beal, «Synthesis and Characterisation of Metal Chalcogenide Nanocrystals,» 2009.

[156] C. N. R. Rao, A. Müller e A. K. Cheetham, Nanomaterials chemistry: recent developments and new directions, John Wiley & Sons, 2007.

[157] T. Sugimoto, *Adv. Colloid Interface Sci.,* vol. 28, p. 165, 1987.

[158] I. M. Lifshitz e V. V. Slyozov, «The kinetics of precipitation from supersaturated solid solutions,» *Journal of physics and chemistry of solids,* vol. 19, pp. 35-50, 1961.

[159] C. Wagner, «Theorie der alterung von niederschlägen durch umlösen (Ostwald-reifung),» *Berichte der Bunsengesellschaft für physikalische Chemie,* vol. 65, pp. 581-591, 1961.

[160] R. Nagarajan e T. A. Hatton, Nanoparticles: synthesis, stabilization, passivation, and functionalization, ACS Publications, 2008.

[161] J. T. G. Overbeek, «Colloid stability in aqueous and non-aqueous media. Introductory paper,» *Discussions of the Faraday Society,* vol. 42, pp. 7-13, 1966.

[162] S. Xu e Z. L. Wang, «One-dimensional ZnO nanostructures: solution growth and functional properties,» *Nano Research,* vol. 4, pp. 1013-1098, 2011.

[163] J. Zang, C. M. Li, X. Cui, J. Wang, X. Sun, H. Dong e C. Q. Sun, «Tailoring zinc oxide nanowires for high performance amperometric glucose sensor,» *Electroanalysis,* vol. 19, pp. 1008-1014, 2007.

[164] S. Baruah e J. Dutta, «pH-dependent growth of zinc oxide nanorods,» *Journal of Crystal Growth,* vol. 311, pp. 2549-2554, 2009.

[165] R. A. Laudise e A. A. Ballman, «Hydrothermal synthesis of zinc oxide and zinc sulfide,» *The Journal of Physical Chemistry,* vol. 64, pp. 688-691, 1960.

[166] L. N. Demianets, D. V. Kostomarov, I. P. Kuz'mina e S. V. Pushko, «Mechanism of growth of ZnO single crystals from hydrothermal alkali solutions,» *Crystallography Reports,* vol. 47, pp. S86--S98, 2002.

[167] L. N. Demianets e D. V. Kostomarov, «Mechanism of zinc oxide single crystal growth under hydrothermal conditions,» in *Annales de Chimie Science des Matériaux*, 2001.

[168] L. N. Demianets, D. V. Kostomarov e I. P. Kuz'mina, «Chemistry and kinetics of ZnO growth from alkaline hydrothermal solutions,» *Inorganic Materials,* vol. 38, pp. 124-131, 2002.

[169] A. Kawska, P. Duchstein, O. Hochrein e D. Zahn, «Atomistic mechanisms of ZnO aggregation from ethanolic solution: Ion association, proton transfer, and self-organization,» *Nano letters,* vol. 8, pp. 2336-2340, 2008.

[170] J. Zhang, L. Sun, J. Yin, H. Su, C. Liao e C. Yan, «Control of ZnO morphology via a simple solution route,» *Chemistry of Materials,* vol. 14, pp. 4172-4177, 2002.

[171] B. Cheng e E. T. Samulski, «Hydrothermal synthesis of one-dimensional ZnO nanostructures with different aspect ratios,» *Chemical Communications,* pp. 986-987, 2004.

[172] H. L. Cao, X. F. Qian, Q. Gong, W. M. Du, X. D. Ma e Z. K. Zhu, «Shape-and size-controlled synthesis of nanometre ZnO from a simple solution route at room temperature,» *Nanotechnology,* vol. 17, p. 3632, 2006.

[173] B. Liu e H. C. Zeng, «Hydrothermal synthesis of ZnO nanorods in the diameter regime of 50 nm,» *Journal of the American Chemical Society,* vol. 125, pp. 4430-4431, 2003.

[174] X. Hou, F. Zhou, Y. Sun e W. Liu, «Ultrasound-assisted synthesis of dentritic ZnO nanostructure in ionic liquid,» *Materials Letters,* vol. 61, pp. 1789-1792, 2007.

[175] T. Alammar e A.-V. Mudring, «Facile ultrasound-assisted synthesis of ZnO nanorods in an ionic liquid,» *Materials Letters,* vol. 63, pp. 732-735, 2009.

[176] J. Liu, X. Huang, Y. Li, X. Ji, Z. Li, X. He e F. Sun, «Vertically aligned 1D ZnO nanostructures on bulk alloy substrates: direct solution synthesis, photoluminescence, and field emission,» *The Journal of Physical Chemistry C,* vol. 111, pp. 4990-4997, 2007.

[177] M. Q. Fatmi, T. S. Hofer e B. M. Rode, «The stability of [Zn (NH 3) 4] 2+ in water: a quantum mechanical/molecular mechanical molecular dynamics study,» *Physical Chemistry Chemical Physics,* vol. 12, pp. 9713-9718, 2010.

[178] Q. Tang, W. Zhou, J. Shen, W. Zhang, L. Kong e Y. Qian, «A template-free aqueous route to ZnO nanorod arrays with high optical property,» *Chemical communications,* pp. 712-713, 2004.

[179] D. S. Boyle, K. Govender e P. O'Brien, «Novel low temperature solution deposition of perpendicularly orientated rods of ZnO: substrate effects and evidence of the importance of counter-ions in the control of crystallite growth,» *Chemical Communications,* pp. 80-81, 2002.

[180] L. Vayssieres, «Growth of arrayed nanorods and nanowires of ZnO from aqueous solutions,» *Advanced Materials,* vol. 15, pp. 464-466, 2003.

[181] S. Baruah e J. Dutta, «Hydrothermal growth of ZnO nanostructures,» *Science and Technology of Advanced Materials,* vol. 10, p. 013001, 2009.

[182] K. Govender, D. S. Boyle, P. B. Kenway e P. O'Brien, «Understanding the factors that govern the deposition and morphology of thin films of ZnO from aqueous solution,» *Journal of Materials Chemistry,* vol. 14, pp. 2575-2591, 2004.

[183] I. S. Ahuja, C. L. Yadava e R. Singh, «Structural information on manganese (II), cobalt (II), nickel (II), zinc (II) and cadmium (II) sulphate complexes with hexamethylenetetramine (a potentially tetradentate ligand) from their magnetic moments, electronic and infrared spectra,» *Journal of Molecular Structure,* vol. 81, pp. 229-234, 1982.

[184] F. Solís-Pomar, E. Martínez, M. F. Meléndrez e E. Pérez-Tijerina, «Growth of vertically aligned ZnO nanorods using textured ZnO films,» *Nanoscale research letters,* vol. 6, p. 524, 2011.

[185] S. Xu, N. Adiga, S. Ba, T. Dasgupta, C. F. J. Wu e Z. L. Wang, «Optimizing and improving the growth quality of ZnO nanowire arrays guided by statistical design of experiments,» *ACS nano,* vol. 3, pp. 1803-1812, 2009.

[186] S. Xu, C. Lao, B. Weintraub e Z. L. Wang, «Density-controlled growth of aligned ZnO nanowire arrays by seedless chemical approach on smooth surfaces,» *Journal of Materials Research,* vol. 23, pp. 2072-2077, 2008.

[187] M. N. R. Ashfold, R. P. Doherty, N. G. Ndifor-Angwafor, D. J. Riley e Y. Sun, «The kinetics of the hydrothermal growth of ZnO nanostructures,» *Thin Solid Films,* vol. 515, pp. 8679-8683, 2007.

[188] H. E. Unalan, P. Hiralal, N. Rupesinghe, S. Dalal, W. I. Milne e G. A. J. Amaratunga, «Rapid synthesis of aligned zinc oxide nanowires,» *Nanotechnology,* vol. 19, p. 255608, 2008.

[189] S.-H. Jung, E. Oh, K.-H. Lee, W. Park e S.-H. Jeong, «A sonochemical method for fabricating aligned ZnO nanorods,» *Advanced Materials,* vol. 19, pp. 749-753, 2007.

[190] L. Shi, K. Bao, J. Cao e Y. Qian, «Sunlight-assisted fabrication of a hierarchical ZnO nanorod array structure,» *CrystEngComm,* vol. 11, 2009.

[191] L. E. Greene, M. Law, J. Goldberger, F. Kim, J. C. Johnson, Y. Zhang, R. J. Saykally e P. Yang, «Low-temperature wafer-scale production of ZnO nanowire arrays,» *Angewandte Chemie International Edition,* vol. 42, pp. 3031-3034, 2003.

[192] T.-Y. Liu, H.-C. Liao, C.-C. Lin, S.-H. Hu e S.-Y. Chen, «Biofunctional ZnO nanorod arrays grown on flexible substrates,» *Langmuir,* vol. 22, pp. 5804-5809, 2006.

[193] A. Manekkathodi, M.-Y. Lu, C. W. Wang e L.-J. Chen, «Direct growth of aligned zinc oxide nanorods on paper substrates for low-cost flexible electronics,» *Advanced materials,* vol. 22, pp. 4059-4063, 2010.

[194] C.-S. Hsiao, C.-H. Peng, S.-Y. Chen e S.-C. Liou, «Tunable growth of ZnO nanorods synthesized in aqueous solutions at low temperatures,» *Journal of Vacuum Science \|& Technology B: Microelectronics and Nanometer Structures Processing, Measurement, and Phenomena,* vol. 24, pp. 288-291, 2006.

[195] J. Qiu, X. Li, W. He, S.-J. Park, H.-K. Kim, Y.-H. Hwang, J.-H. Lee e Y.-D. Kim, «The growth mechanism and optical properties of ultralong ZnO nanorod arrays with a high aspect ratio by a preheating hydrothermal method,» *Nanotechnology,* vol. 20, p. 155603, 2009.

[196] http://www.piezo.com/tech4history.html.

[197] http://ruby.chemie.uni-freiburg.de/Vorlesung/fk_chemie_3.html.

[198] G. Bertotti e I. D. Mayergoyz, The science of hysteresis: Hysteresis in materials, vol. 3, Gulf Professional Publishing, 2006.

[199] https://investigacion.us.es/docs/web/files/auriga_brochure.pdf.

[200] D. Delmonte, *Combined magnetic, electric, ferroelectric and magnetoelectric characterization of novel multiferroic perovskites obtained by high pressure/temperature synthesis,* Universita' degli studi di Parma - IMEM-CNR, 2015.

[201] *Manual of TF Analyzer 2000E / Vers. 4.0.M2.*

[202] Griffiths, David J. (2007), Introduction to Electrodynamics, 3rd Edition.

[203] https://www.azonano.com/article.aspx?ArticleID=2682.

[204] https://www.asylumresearch.com/Applications/PFMAppNote/PFMAppNote.shtml.

[205] http://www.csinstruments.eu/piezoresponse-force-microscopy-mode/.

[206] https://www.budgetsensors.com/force-modulation-afm-probe-multi75.

[207] https://www.youtube.com/watch?v=UEIn5XlKGrQ&feature=youtu.be.

[208] B. D. Cullity, «Elements of X-Ray Diffraction 2nd edition. Addision-Wesley Pub. Co,» *Inc., CA, USA,* vol. 197, p. 356, 1978.

[209] V. Ciupină, S. Zamfirescu e G. Prodan, «Evaluation of mean diameter values using Scherrer equation applied to electron diffraction images,» *Nanotechnology--Toxicological Issues and Environmental Safety and Environmental Safety,* pp. 231-237, 2007.

[210] M. Culiolo, *Funzionalizzazione di fibre di carbonio con nanorods di ZnO per applicazioni piezoelettriche,* Università degli Studi di Parma, 2014.

[211] Stephen Herman, Delmar's Standard Textbook of Electricity - Sixth Edition, 2015.

[212] M.-H. Zhao, Z.-L. Wang e S. X. Mao, «Piezoelectric characterization of individual zinc oxide nanobelt probed by piezoresponse force microscope,» *Nano Letters,* vol. 4, pp. 587-590, 2004.

[213] J. A. Christman, H. Maiwa, S.-H. Kim, A. I. Kingon e R. J. Nemanich, «Piezoelectric measurements with atomic force microscopy,» *MRS Online Proceedings Library Archive,* vol. 541, 1998.

[214] X. Wang, «Piezoelectric nanogenerators—Harvesting ambient mechanical energy at the nanometer scale,» *Nano Energy,* vol. 1, pp. 13-24, 2012.

[215] Y. Gao e Z. L. Wang, «Electrostatic potential in a bent piezoelectric nanowire. The fundamental theory of nanogenerator and nanopiezotronics,» *Nano letters,* vol. 7, pp. 2499-2505, 2007.

[216] E. S. K. a. M. G. S. Y. Iossel, «Raschet Elektricheskoy Yemkosti,» *Leningradskoye Otdeleniye "Energiya",* 1969.

[217] T. Hanada, «Basic properties of ZnO, GaN, and related materials,» *Oxide and nitride semiconductors,* pp. 1-19, 2009.

[218] E. Broitman, M. Y. Soomro, J. Lu, M. Willander e L. Hultman, «Nanoscale piezoelectric response of ZnO nanowires measured using a nanoindentation technique,» *Physical Chemistry Chemical Physics,* vol. 15, pp. 11113-11118, 2013.

[219] D. Calestani, M. Z. Zha, L. Zanotti, M. Villani e A. Zappettini, «Low temperature thermal evaporation growth of aligned ZnO nanorods on ZnO film: a growth mechanism promoted by Zn nanoclusters on polar surfaces,» *CrystEngComm,* vol. 13, pp. 1707-1712, 2011.

[220] http://lichtzen.com/english/product_06_01.html.

[221] http://lichtzen.com/english/product_01_01.html.

[222] http://www.carbonfiberdesigns.com/carbon-fiber-facts.html.

[223] W.-J. Li, E.-W. Shi, W.-Z. Zhong e Z.-W. Yin, «Growth mechanism and growth habit of oxide crystals,» *Journal of crystal growth,* vol. 203, pp. 186-196, 1999.

[224] P. X. Gao e Z. L. Wang, «Substrate atomic-termination-induced anisotropic growth of ZnO nanowires/nanorods by the VLS process,» *The Journal of Physical Chemistry B,* vol. 108, pp. 7534-7537, 2004.

[225] A. Klein, «Polare Eigenschaften von Zinkoxid-Kristallen,» *Zeitschrift für Physik A Hadrons and Nuclei,* vol. 188, pp. 352-360, 1965.

[226] N. Prileschajew, «Oxydation ungesättigter Verbindungen mittels organischer Superoxyde,» *European Journal of Inorganic Chemistry,* vol. 42, pp. 4811-4815, 1909.

[227] «Clayton May, Epoxy Resins: Chemistry and Technology, Second Edition, 1985».

[228] B. Ellis e others, Chemistry and technology of epoxy resins, Springer, 1993.

Acknowledgments / Ringraziamenti

Il ringraziamento più grande va ad Angela, che mi è sempre stata vicino, sia nei momenti belli che in quelli brutti, e mi ha spronato quando sono stato incerto. Lo ammetto, in questo sono stato fortunato.
Un grandissimo ringraziamento va ai miei genitori, Elena, i miei nonni (soprattutto TU, che il mio dottorato hai potuto solo vederlo iniziare, ma sei sempre con me e dentro di me), i miei zii… insomma, alla mia famiglia! Così come alla mia famiglia "adottiva" allargata, composta dalla famiglia di Angela (Natina e Antonio, i fratelli, i nonni, le migliaia di zii, cugini e partner), Rosaria, Mauro e Francesco. Un grazie particolare ad Antonio "u patata" che mi ha spinto ad entrare nel mondo stimolante della scuola pubblica.
I want to thank my tutor, Prof. Andrea Zappettini, for all the energy, frankness, teaching and the opportunities he gave me during my PhD.
A huge thanksgiving goes to Prof. Sang-Woo Kim and Prof. Massimo Solzi for giving me the possibility to live the fantastic working and personal experience in South Korea. All the students and researchers at NESEL have been extremely welcoming and accommodating. Over there I send my thanks especially to Usman, Tae-Ho and Tae-Yun.
Non posso certo privare di un grande ringraziamento lo stranissimo e sempre presente Pietro, Giulio (Giulio chi? Ah, il Mistra!), Simone (Simone chi? Ah, il Ghine!), Roberta, le ragazze di Borgo Regale (compresa Lucia) e tutte le persone che in qualche modo hanno reso più bella, simpatica, divertente, stuzzicante, strana ed interessante la mia permanenza in questa città.
Un ringraziamento particolare va anche al mio coinquilino Nicola (Nicola chi? Ah, il Casta!), l'unico con cui non sia mai stato necessario litigare.
Voglio mandare un ringraziamento speciale anche a due persone che hanno condiviso tanto tempo con me, all'IMEM e fuori dall'IMEM, che rappresentano più che semplici colleghi: Filippo e Matteo (Matteo chi? Ah, il Bronz!).
Sempre nell'ambiente dell'IMEM e dell'università ringrazio per la compagnia e per l'aiuto i miei colleghi, in particolare Davide (Davide chi? Ah, il lombre! Cioè, Dedè! Cioè, quel pazzo che gira cantando ed imprecando per l'istituto!), Marco (Marco chi? Ah, il Villo!) che oggi mi ha causato un enorme trauma tagliandosi la storica cresta, Davide (ancora Davide? Ma chi? Ah, il Calle!), Zamb, Ben, il mio efficientissimo e disponibilissimo compagno di ufficio Manuele, Greta, Paola, Marco, Martina, Silvio e Sara. A proposito… non lavorate troppo eh!
Ringrazio inoltre i ragazzi di ESN e quella simpatica combriccola che sono I Pigiamas.
Infine potrebbe sembrare immodesto, ma penso che non sia sbagliato ringraziare anche me stesso, perché la vita è un cecchino che tira continuamente dei colpi "mica da ridere", come si dice da queste parti, e se si arriva al traguardo, in un modo o nell'altro, non è esagerato sentire il bisogno di ringraziarsi.
Sono stato studente per 23 anni. Questo passaggio sancisce la fine del mio percorso da studente nel senso stretto del termine, ma nella vita lo sarò per sempre. E' un

momento che è stato tanto sognato, ma adesso, che all'orizzonte compaiono i 30 anni, forse un giretto nel passato lo farei volentieri nonostante libri, appunti, dispense ed esami.
If I forgot to thank someone I hope you would understand, I am about to submit the notorious PhD thesis…
Se ho dimenticato di ringraziare qualcuno spero capiate, sto per consegnare la famigerata tesi di dottorato…